NUCLEAR ENGINEERING

MASSACHUSETTS INSTITUTE
OF TECHNOLOGY

Experimental Investigation of the Thermal-Hydraulics of Gas Jet Expansion In a Two-Dimensional Liquid Pool

by

R. A. Rothrock and M. S. Kazimi

MITNE-223

Department of Nuclear Engineering
Massachusetts Institute of Technology

October 1978

Experimental Investigation of the Thermal-Hydraulics of Gas Jet Expansion In a Two-Dimensional Liquid Pool

by

R. A. Rothrock and M. S. Kazimi

Report Issues Under Contract NRC-04-77-126
U.S. Nuclear Regulatory Commission

EXPERIMENTAL INVESTIGATION OF THE THERMAL-HYDRAULICS OF GAS JET EXPANSION IN A TWO-DIMENSIONAL LIQUID POOL

ABSTRACT

Gas jet blowdown in a two-dimensional liquid pool has been experimentally investigated. Two sets of experiments were performed: a set of hydrodynamic experiments, where a noncondensible gas is injected into a subcooled liquid pool; and a set of thermal-hydraulic experiments, where a noncondensible heated gas is injected into a near saturated liquid pool. Liquid entrainment by the gas, bubble growth characteristics, and the potential for vaporization, were investigated for a variety of experimental pressures (3 to 10 bars) and two liquid types (water and R-113). Liquid entrainment increased with increasing pressure. The fraction of the jet volume which is liquid is relatively the same for all pressures and decreases with time of expansion. A Taylor instability mechanism for entrainment is found to underpredict the entrained volume. In the initial stages of the expansion, higher entrainment is experienced for more dense fluids. For the same fluid, the entrainment rate was slightly higher for the heated experiments compared to the unheated experiments. Both lateral and vertical growth rates increased with pressure. Vaporization may have occurred for the 4 bar initial pressure, 12 °C superheat condition in freon R-113.

ACKNOWLEDGEMENTS

This report is based on a thesis submitted by the first author to M.I.T. in fulfillment of the requirements for the degree of Master of Science in Nuclear Engineering.

The authors would like to thank Professor Warren Rohsenow whose help was valuable, Mr. Mike Corradini and Mr. Joseph Caloggero whose advice during design, construction, and operation of this experiment expedited this project as well as provided the author with the necessary foresight to execute a successful experiment.

The first author would also like to extend special acknowledgement to his parents for their support during an entire lifetime.

TABLE OF CONTENTS

Page

Chapter I. Introduction

Chapter II. Review of Previous Work

Chapter III. Experimental Apparatus

Chapter IV. Experimental Procedure and Uncertainties

Table of Contents (Continued)

Table of Contents (Continued)

LIST OF FIGURES

List of Figures (Continued)

List of Figures (Continued)

LIST OF TABLES

I. INTRODUCTION

1.1 Motivation for the Study

A substantial effort is presently underway in the United States to investigate the consequences of a hypothetical core disruptive accident (HCDA) in the liquid metal fast breeder reactor (LMFBR). Although the HCDA is a very low probability event, its potential consequences to the public and the environment must be considered in both designing and licensing of the LMFBR nuclear power plant. This comprehensive consideration is required to insure public safety and environmental quality.

Much of the effort in the study of HCDAs is involved with the initiating events, the path on which the accident proceeds, and the termination of the accident. However, a number of phenomena involved in the analysis require a better understanding. These phenomena include fuel self-mixing, as was shown by SIMMER-I (an LMFBR disrupted core analysis code [1]), fluid-structure drag and hydrodynamic effects of the upper core internals, and the role of sodium entrainment in the expansion of the fuel vapor in the above core region.

1.2 Background

In the LMFBR, two basic initiating events which lead to a HCDA have been the focus of the safety analysis [2]. These are the transient overpower (TOP) accident with mild reactivity insertion rates and the loss of flow (LOF) accident with flow decay corresponding to pump coastdown. Both of these events are assumed to occur with failure of the reactor protection system. Figure 1.1 is a schematic of the major components of an LMFBR, namely the Clinch River Breeder Reactor (CRBR).

In either event, fuel and clad melting is expected to occur with a power pulse resulting from sudden reactivity insertions caused by fuel compaction or large thermal reactions caused by fuel coolant interactions (FCI). The TOP accident in small and intermediate size LMFBR is expected to cause partial core meltdown while the LOF accident is expected to result in as much as 80% of the core melting. This could eventually result in fuel vaporization creating high pressures in excess of 50 bars (50 atmospheres) [2]. In both accidents, relief for the work caused by this energy release must be provided either by internal mechanical and/or thermal interactions or venting of the disrupted region, thus providing pathways for radioactivity releases.

For the TOP initiated accident, the relocation of the melted core material may be relatively slow and towards the upper axial core boundaries where nonmelting conditions exist. Some radial movement may occur by hydraulic pressure of the pump head. Thus, freezing of the molten core material would result possibly giving rise to a plugged core condition creating a multiphase pool of core material. It is currently predicted, however, that only a small part of the fuel inventory will undergo melting before neutronic shutdown.

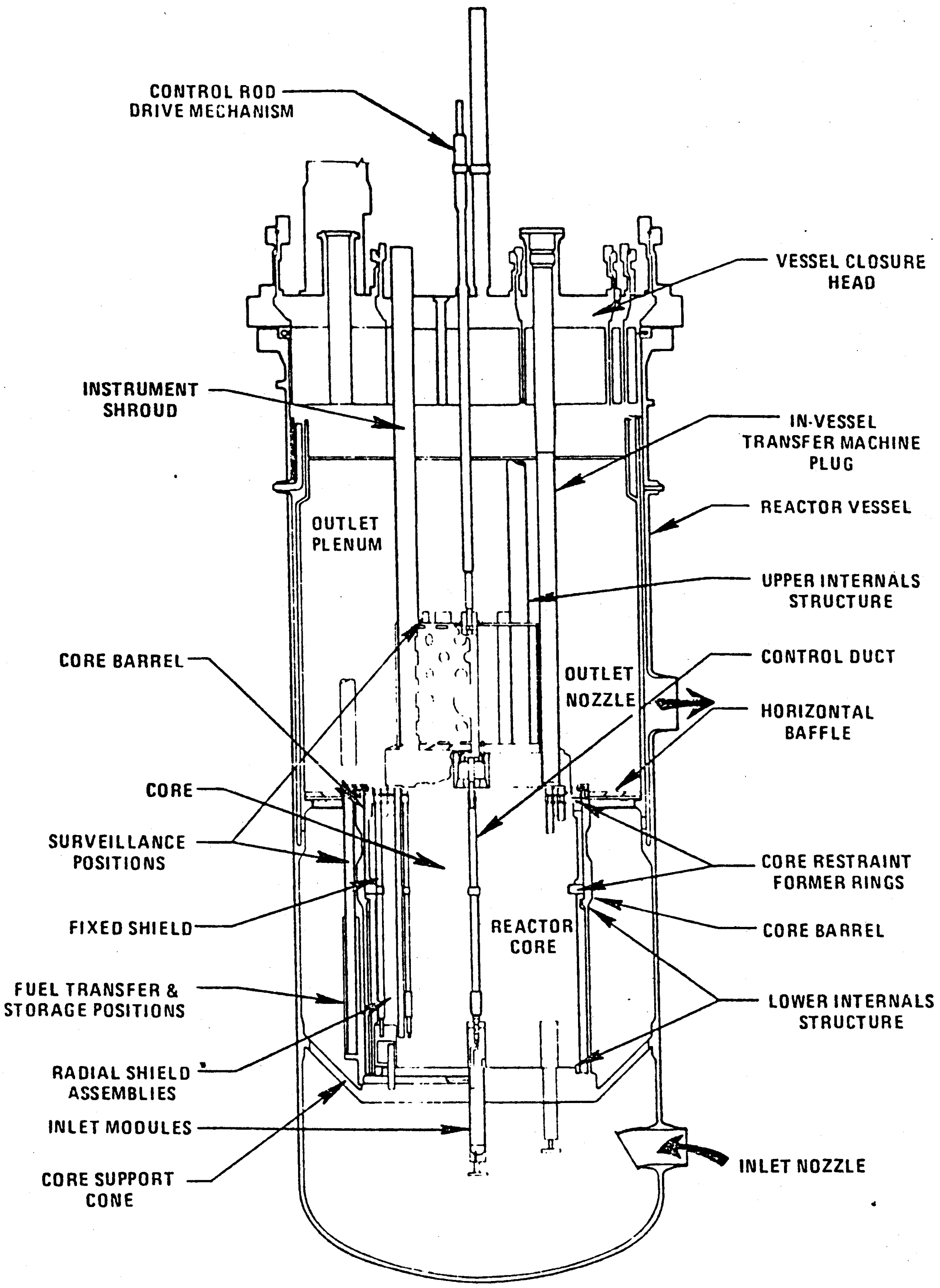

Figure 1.1: View of an LMFBR (CRBR) reactor vessel showing major components

For the LOF initiated accident, loss of flow in a core channel with failure to scram would lead to sodium voiding in the channel resulting in overheating and sudden fuel and clad melting. This condition could propagate quickly from fuel pin to fuel pin thus causing a substantial portion of the active core region to be relocated and/or compacted. This could then cause a prompt supercritical condition which would result in a large power pulse. Because of the massiveness and structure of the surrounding core blanket region and structure, the molten and/or vaporized core would most likely be directed upward through the upper core internal structure discharging into the above core region of subcooled sodium. Figure 1.2 illustrates the main components of concern during an HCDA and the probable path of the core material. This dispersion of fuel would greatly reduce the change of nuclear recriticality and provide a mechanism for distributing the heat by condensation and/or freezing of the core material. With injection of the molten/vaporized core material into the upper sodium region, termination of the accident would probably occur.

There are many different pathways the HCDA can pursue once initiated. Figure 1.3 is a diagram showing a comprehensive approach to LOF initiated HCDA [3]. The present work is a separate effects study of the fuel vapor (gas) injection into the subcooled sodium (liquid) of the above core region.

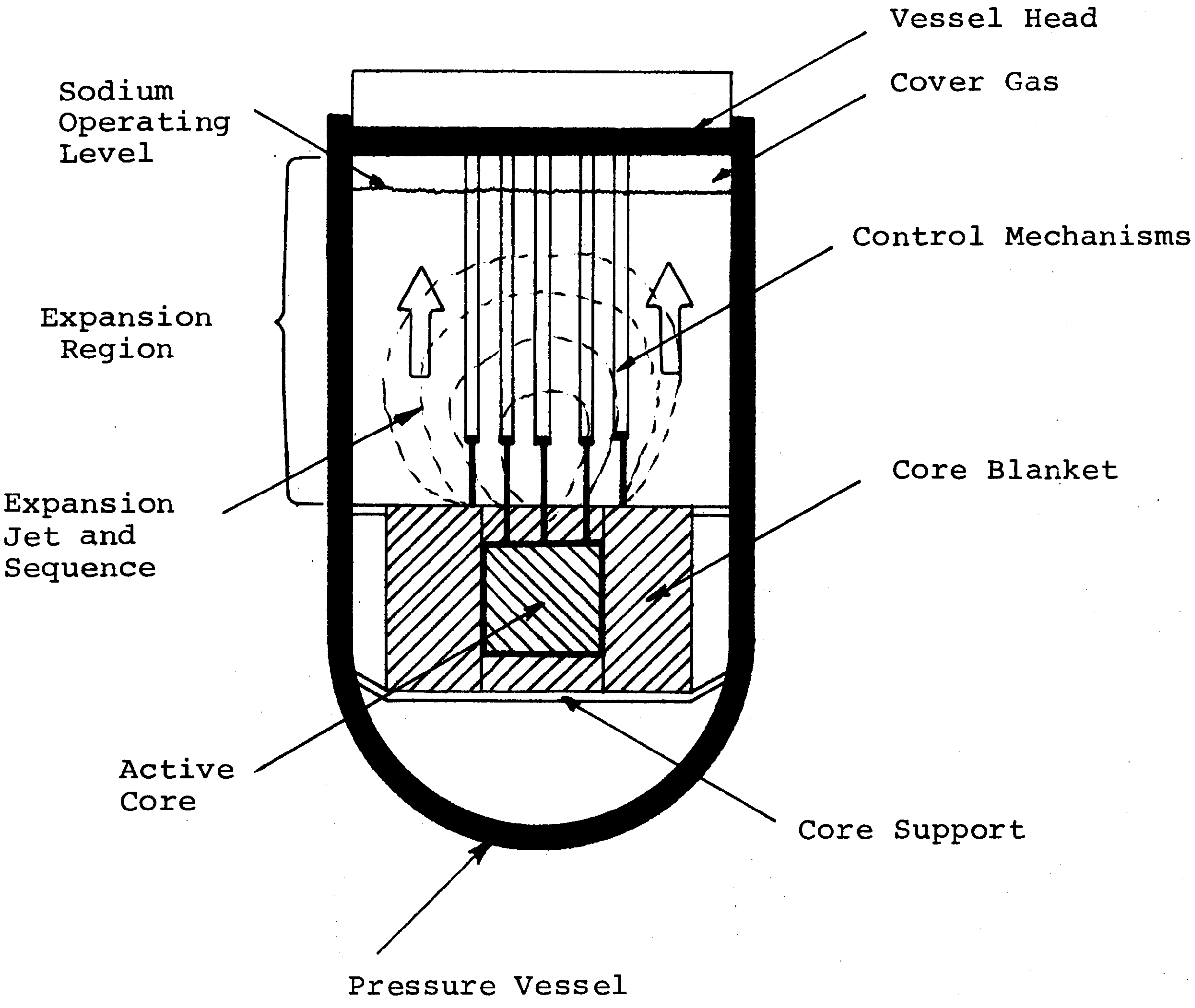

Figure 1.2: LMFBR vessel sectional view illustrating expansion region and expansion jet sequence during a HCDA initiated by LOF.

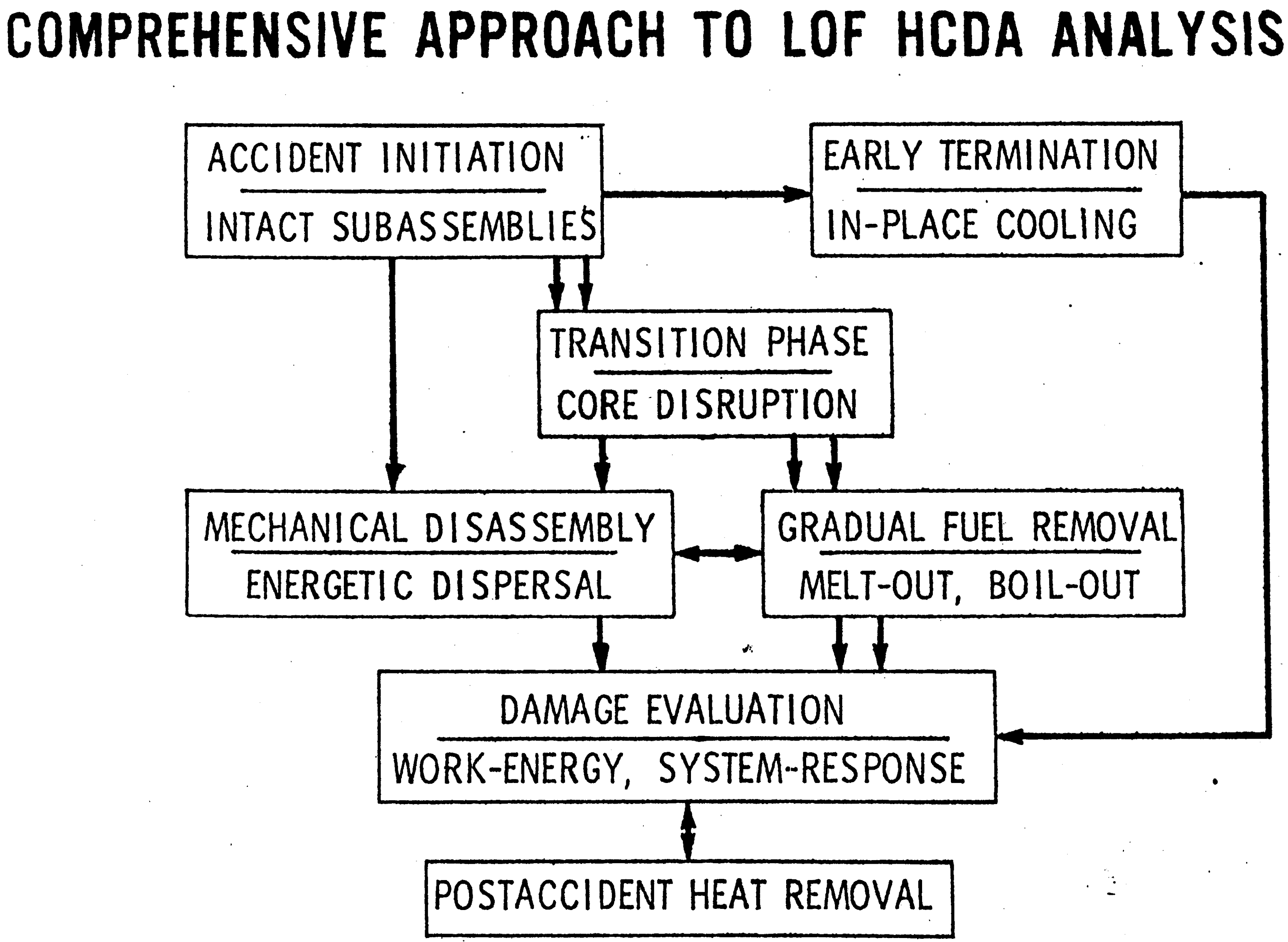

Figure 1.3: Possible sequence of events of a HCDA initiated by LOF

1.3 Purpose and Specific Objectives

The purpose of this work is to experimentally observe the transient development of a two-phase jet expansion as a pressuized gas is injected into a liquid pool. This is called a blowdown. Specifically, this study will observe the liquid entrainment rates in the jet by the injected gas. It is not the intent of this work to model either geometrically or with simulant fluid the actual HCDA. The intent of this work is to study "separate effects" in this blowdown condition that can contribute to development of a comprehensive model for fuel vapor behavior as it penetrates the upper sodium plenum following a hypothetical core meltdown accident.

The present experiments are of the hydrodynamic and thermal-hydraulic type. The hydrodynamic experiments consist of injecting a noncondensible gas into a subcooled liquid. The thermal-hydraulic experiments consist of injecting a heated noncondensible gas into a near saturated liquid.

1.4 Thesis Organization

A brief review of previous work on transient two-phase jets is presented in Chapter 2. Chapter 3 is a description of the experimental set up and apparatus. The experiments undertaken and the general procedure are discussed in Chapter 4. The hydrodynamic results are discussed in Chapter 5. The thermal-hydraulic results are discussed in Chapter 6. A summary of the major conclusions and recommendations for future work are presented in Chapter 7.

II. REVIEW OF PREVIOUS WORK

2.1 Two-Phase Jets in General

The area of two-phase transient jets development and the phenomena associated with these jets such as liquid entrainment is not well understood. Recently, the effort to understand such phenomena has increased since the penetration of the fuel vapor into the subcooled sodium plenum following a hypothetical accident in the LMFBR is of this nature.

To date, most of the work in two-phase jets has been steady state analysis. Schlichting [4] gives an excellent review of the basic models to describe the induced mass flow across flow boundaries (entrainment) by steady state jets discharging into a large reservoir. Schlichting considers both circular and two-dimensional jets. That work principally shows how entrainment increases as the distance from the nozzle increases. This is true in both turbulent and laminar jets. It should be noted that all jets become turbulent a small distance from the nozzle, except when the exit velocity of the fluid is small.

Several experiments have been performed with steady state jets. Ricou and Spalding [5] performed experiments which concentrated on describing the mass flow rate across a jet boundary. The jet and reservoir, in which the jet was injected, were gases of various densities and molecular weights. The main result of that work was a relationship between the entrained mass, the mass flow rate of the jet, the length of the jet, the nozzle diameter, and the density ratio of the entraining and entrained fluids.

An experiment by Kerney, Faeth, and Olson [6] studied the turbulent cavity formed by a steam jet discharging into a subcooled liquid water pool under steady state conditions. Relationships were developed for the jet cavity length as a function of nozzle diameter, exit mass velocity, and a driving potential for condensation. The correlations derived were capable of predicting the jet cavity length over a large range of experimental variables. The principal correlation relates cavity length, condensation driving potential, and mass velocity of the jet.

Tsai and Kazimi [7] have made calculations with regard to hot vapor jet penetration in subcooled liquids. In that work they identified the physical parameters that establish whether jet-like penetration or bubble-like expansion occurs. It was found that penetration depth decreased with increasing condensation heat flux and/or decreasing vapor mass velocity and the heat of vaporization. These results were in good agreement with Kerney's [6] et al. experimental results.

In an attempt to study the initial transient behavior of submerged jets, Abramovich and Solan [8] conducted experiments of both steady state and transient laminar jets. The results of these experiments were correlated with a liquid-drop model [8], which balanced fluid momentum and drag forces on a ball in front of a developing jet nozzle. These experiments also lead to correlations on the penetration rate for several fluid combinations.

A model is presented by Chawla [9] describing the phenomenon of liquid entrainment resulting from the presence of Kelvin-Helmholtz [10] instabilities at the gas/liquid interface of a sonic gas jet submerged in a liquid. Kelvin-Helmholtz instabilities are caused by relative motion of the fluids parallel to the gas/liquid interface. Chawla's model satisfactorily correlated previous experimental results of Bell, Boyce and Collier [11].

In accordance with many works, the ratio of the density of the injecting fluid to the density of the fluid in which the discharge takes place is a major physical parameter which governs the type of growth experienced by the penetration (jet or bubble). This relationship appears in Ricou et al. [5] work in the entrainment relation developed for jet flow with gases. Theofanous, Grolmes, Lambert, and Epstein [12] performed an analytical analysis similar to Abramovich and Solon's [8] to investigate the relationship of fluid densities on penetration development. Based on momentum changes of the entering jet into an assumed vortex ball (the jet is considered to penetrate the vortex ball contributing to its linear momentum and volume), and the volume change in the ball, a set of equations relating motion and displacement were found. When these equations were solved, by changing the density ratio the analytical model yielded results which were in agreement with the experiment.

As the density ratio of the injected fluid to the medium of the discharged decreased (i.e. air injected into water), spherical or bubble-like growth occurred rapidly since relatively little momentum is imparted to the sphere. For the opposite adjustment of the density ratio (i.e., water injected in air), the water is expected to penetrate in a jet-like manner since a relatively large momentum is imparted to the sphere (vortex ball) at the discharge point. Figure 2.1 illustrates these results. Both of these effects were verified with experiments by Theofanous et al. [12]. These experiments will be discussed later.

2.2 Two-Phase Transient Jet Experiment

Several experiments have been performed with transient two-phase jets specially directed at the understanding of blowdown phenomenon.

The experiments to date can be classified according to the fluids used and initial experimental conditions. Figure 2.2 is a chart indicating what types of experiments have been performed and its relation to the others. The experiments to be discussed henceforth are classified into three main groups.

The three main groups are one-dimensional (1-D), two-dimensional (2-D), and three-dimensional (3-D). Each group is divided into two classes, each containing three subclasses. The classes are high pressure (10-100 bars) and low pressure (1-10 bars). The three subclasses are hydraulic, thermal-hydraulic, and flashing experiments. For the hydraulic test, a noncondensible gas is discharged into a subcooled liquid. For the thermal-hydraulic test, a heated noncondensible gas is discharged into a saturated liquid or a subcooled liquid.

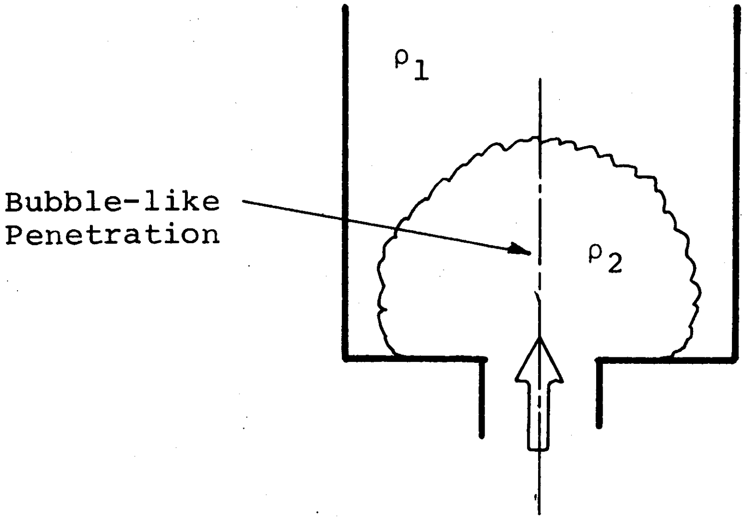

$\frac{\rho_2}{\rho_1} < 1$ Air into Water

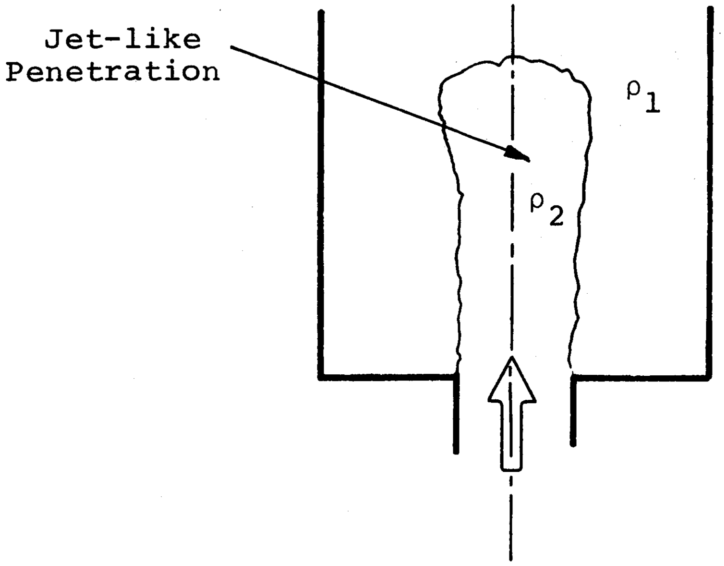

$\frac{\rho_2}{\rho_1} > 1$ Water into Air

Figure 2.1: Illustration of relative shapes of the penetrations for two fluids of different densities

		GROUP		
		1 Dimensional	2 Dimensional	3 Dimensional
LOW PRESSURE 1 - 10 bars	H	MITC [13]	MITR	PUC [14] ANLT [12]
	TH		MITR	
	F			PUC [14] ANLT [12]
HIGH PRESSURE 10 - 100 bars	H			SRI [15]
	TH	SRI [17]		SRI [18]
	F		SRI [16]	SRI [15]

KEY

H - Hydrodynamic
TH - Thermal-hydraulic
F - Flashing
MITC - MIT by Corradini [13]
MITR - MIT by Rothrock [Present work]
PUC - Purdue University by Christopher [14]
ANLT - Argonne National Laboratory by Theofanous [12]
SRI - Stanford Research Institute [15,16,17,18]

Figure 2.2: Summary of experimental work on two-phase jet transients

The flashing tests are those experiments with condensing gases and subcooled or saturated liquids.

Referring to Figure 2.2, the MITC [13] (Massachusetts Institute of Technology by Corradini) experiments were 1D hydraulic low pressure tests primarily performed to study the Taylor instability mechanism of liquid entrainment by a gas. Taylor instabilities on a liquid/gas interface are caused by the acceleration of the liquid perpendicular to the interface [10]. Taylor instabilities were observed during these experiments and an entrainment model based on this phenomenon in 1D has been developed. The application of this treatment to the present experiments will be discussed in Chapter 5.

The MITR (Massachusetts Institute of Technology by Rothrock) experiments are the present work and will be discussed in Chapters 5 and 6.

The PUC (Purdue University by Christopher) [14] experiments were hydraulic and flashing tests at low pressures in 3D. The liquid entrainment rate, hydrodynamic mechanism of the discharges, and analytical modeling of the discharge to approximate convective heat transfer coefficients during the discharge were the primary objectives of that work. Christopher observed entrainment for the condensible gas experiments and no entrainment for the noncondensible gas experiments. Jet/bubble growth was seen to be dependent on the static and dynamic bubble pressures acting in the presence of the liquid pool constraints.

The ANLT (Argonne National Laboratory by Theofanous et al.) [12] experiments were essentially the same as Christopher's experiments. This work verified the modified Abramovich analysis, which indicated growth characteristics of the penetration were dependent on the density of the two fluids. Negligible entrainment of the fluid was found for a high liquid to gas density ratio during spherical or bubble growth.

The SRI (Stanford Research Institute) [15,16,17,18] experiments were widely varied but all high pressure. Some of the tests performed specifically designed to model a HCDA in the Fast Flux Test Facility [18]. The results of these works are quite varied and too lengthy to present in this work.

III. EXPERIMENTAL APPARATUS

3.1 General Description

The experimental apparatus consists of mainly five sections: 1) the gas storage tank or core, 2) the rupture disk flanges, 3) the blowdown chute, 4) liquid pool, and 5) gas plenum. A sectional view showing these five regions of the apparatus is illustrated in Figure 3.1. The region of concern for jet development in the experiment is the region above the blowdown chute. It is designed to reflect the characteristics of a thin section of the sodium upper plenum on the centerline of the CRBR design. The width dimension of the viewing region and the blowdown chute, 30.5 cm and 7.62 cm (12 inches and 3 inches), respectively, is 1/20 scale of the CRBR. The width and height of the blowdown chute are not exactly scaled to the CRBR although it is similar to the fission gas plenum and upper blanket region of the reactor vessel. The height of the viewing region, 50.8 cm (20 inches) is expanded so that the gas plenum is scaled larger than the CRBR to allow for variability in the liquid pool-height. The thickness of these sections is 1.27 cm (1/2 inch). This dimension was chosen to facilitate observation of the blowdown. Simulation of core internals is not included. Below the blowdown chute is an unscaled cylindrical volume which contains the rupture disk assembly flanges and gas storage vessel or core. The rupture disk assembly is used to initiate the

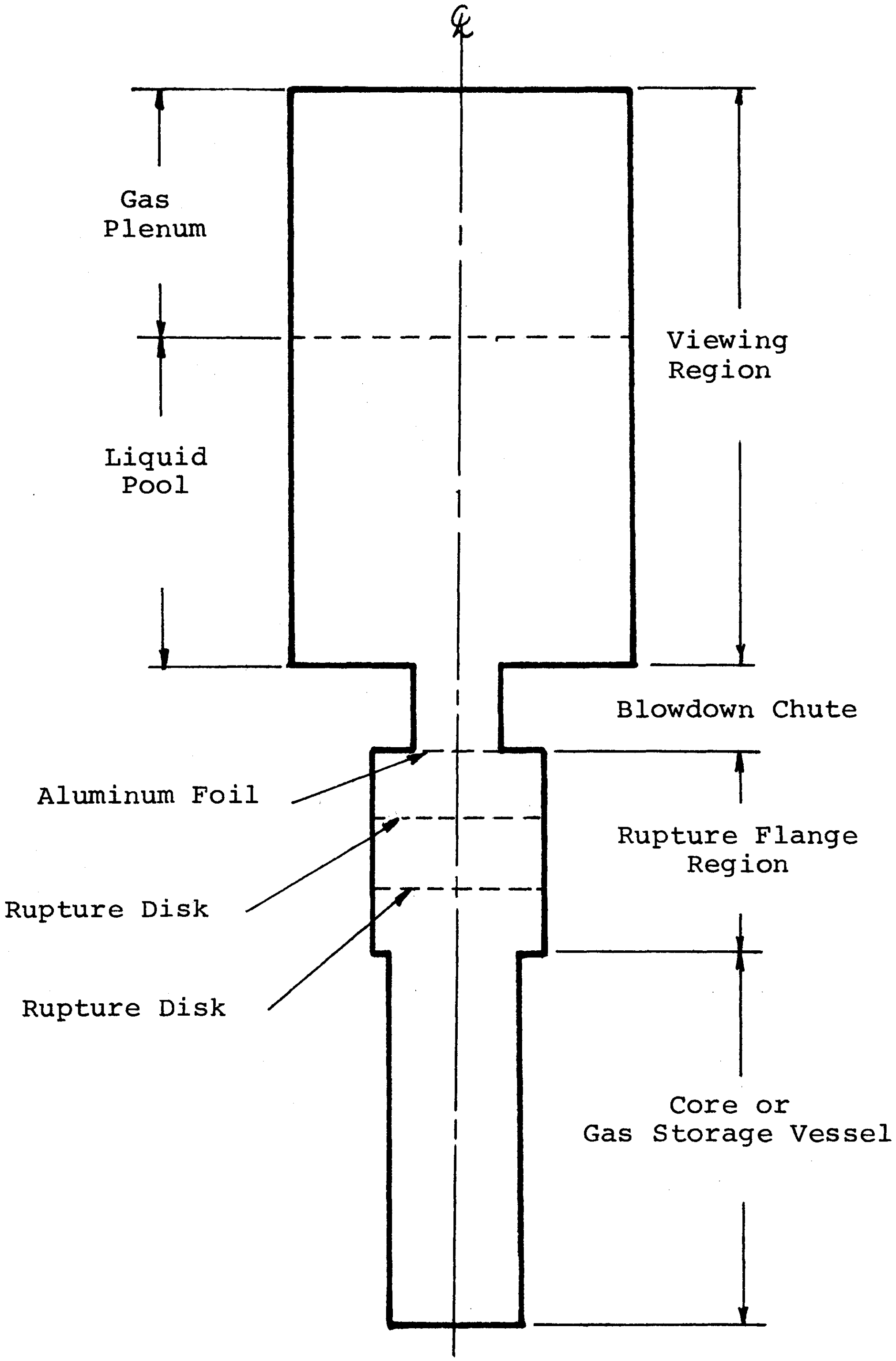

Figure 3.1: Schematic of experimental apparatus

experiment. The core is used for initial gas storage prior to blowdown. The liquid pool was contained above the rupture disk region by a thin (0.3 mm) aluminum foil. This allowed the disks to break properly and allowed an accurate measurement of the liquid volume prior to blowdown to be made.

A pictorial scaled drawing of the apparatus is shown in Figure 3.2. A diagram of the outer perimeter of the working volume is illustrated in Figure 3.3. This figure gives a better view of the experimental volume and thus allows a better understanding of the actual experimental regions and their relation to each other.

3.2 Viewing Region and Blowdown Chute

The viewing region and blowdown chute, Figure 3.4, are the "two-dimensional" parts of the apparatus. The blowdown chute, 7.62 cm x 7.30 cm x 1.27 cm (3 inches x 2-7/8 inches x 1/2 inch) is constructed of 1.27 cm (1/2 inch) plate steel. It is affixed to the underside of the viewing region baseplate, 43 cm x 17.8 cm x 0.64 cm (17 inches x 7 inches x 1/4 inch) plate steel, with a continuous weld providing an air tight seal. The bottom of the chute is continuously welded to the blowdown chute flange, 12.7 cm x 7.62 cm x 0.64 cm (5 inches x 3 inches x 1/4 inch) plate steel which is bolted to the upper flange, 27.9 cm diameter x 2.54 cm thick (11 inch diameter x 1 in thick), of the rupture disk region. The blowdown chute slot 7.62 cm x 1.27 cm (3 inch x 1/2 inch) is through all the preceeding components. On one of the long sides (7.67 cm) of the chute is a threaded hole 0.9525 cm in diameter for the pressure transducer.

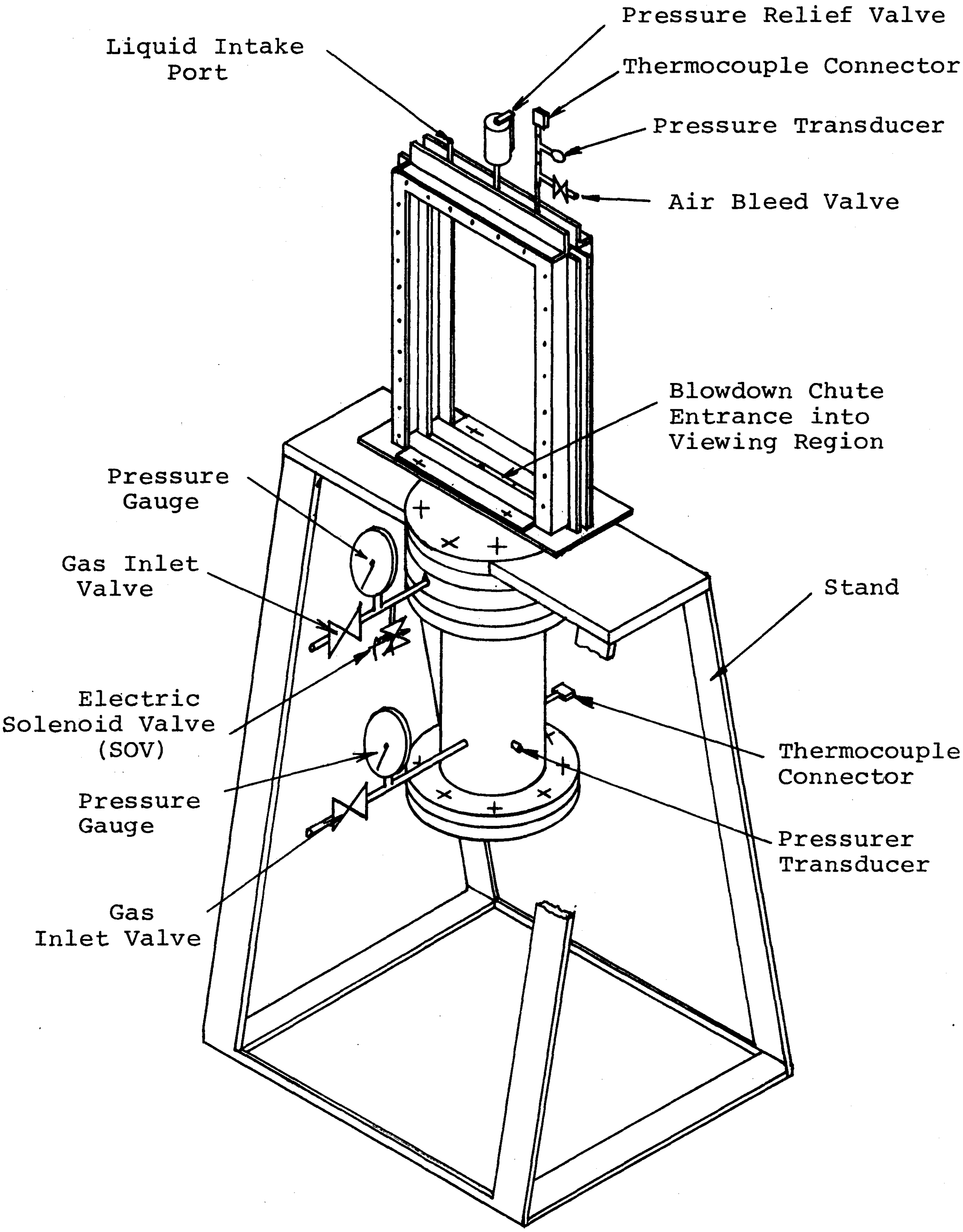

Figure 3.2: Pictorial View of Experimental Apparatus

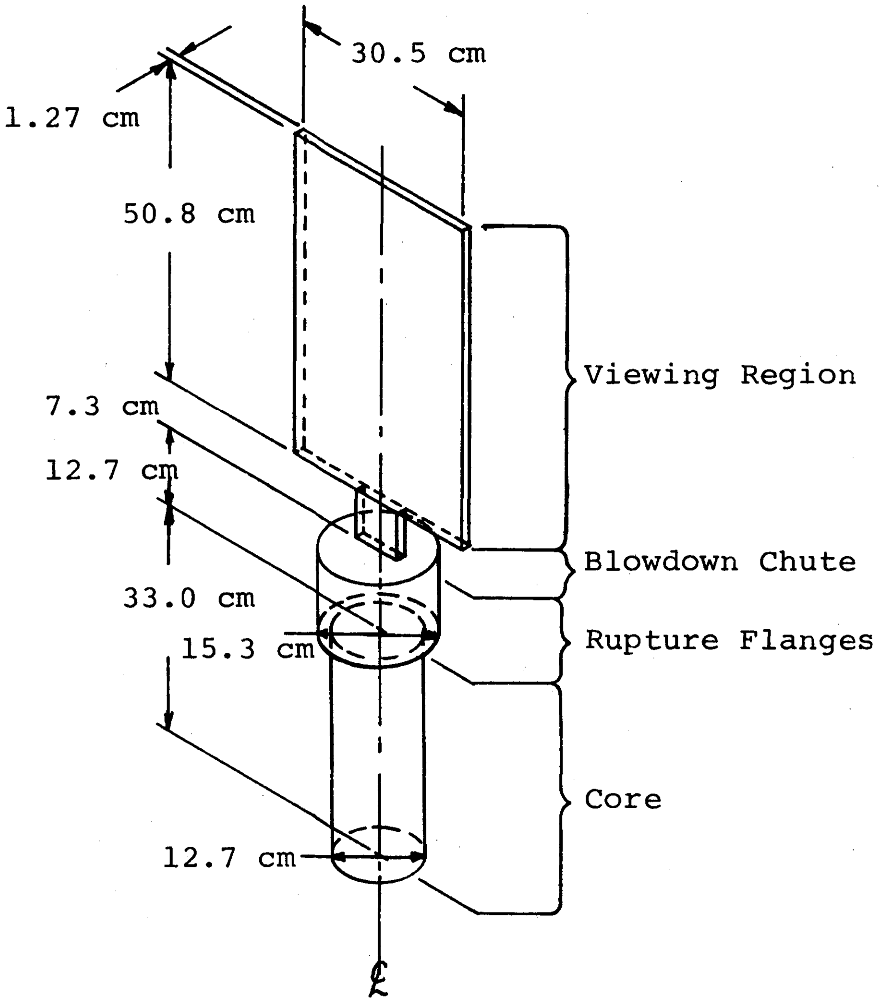

Figure 3.3: Control volume of the experimental apparatus

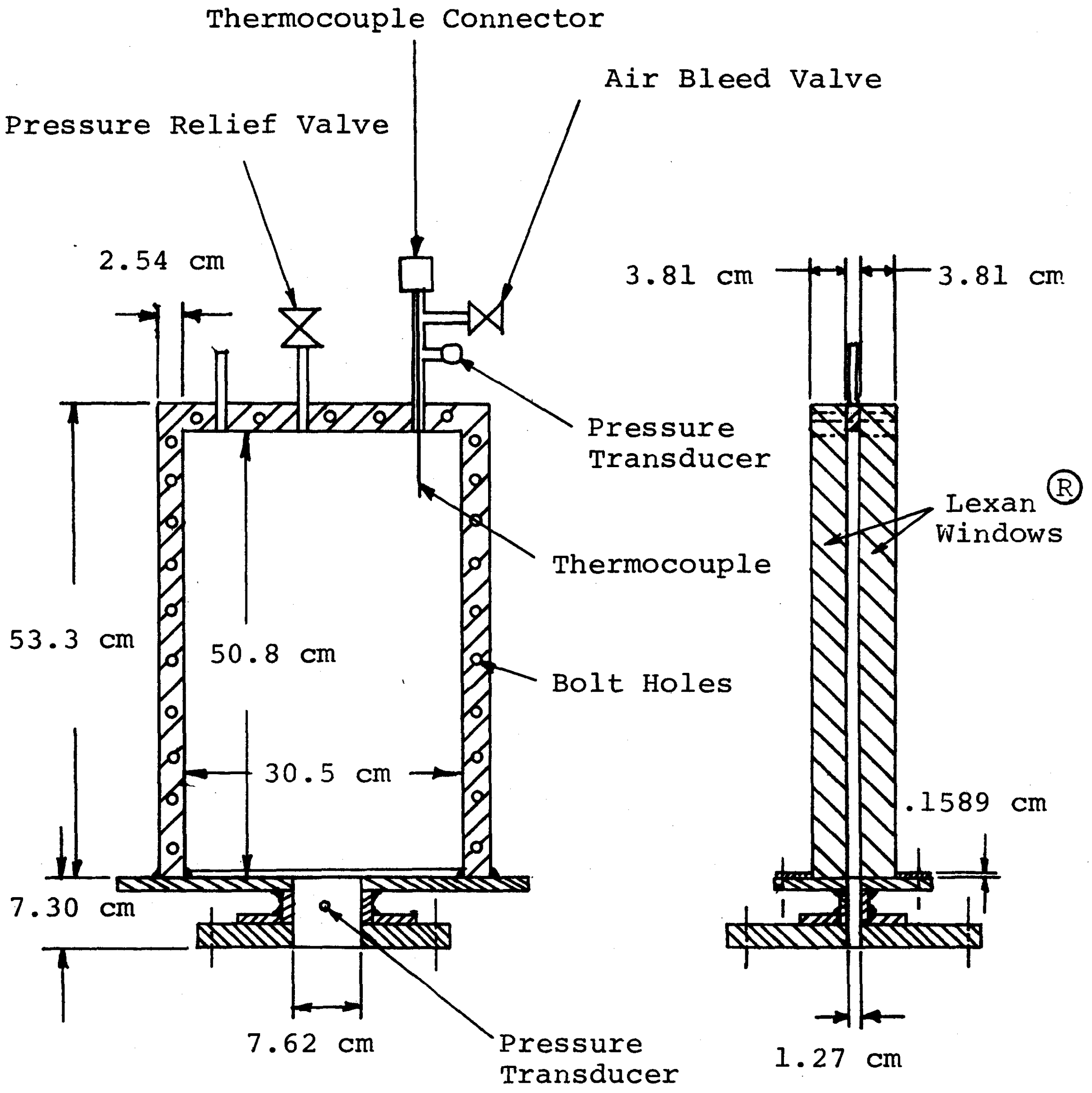

Figure 3.4: Sectional view of viewing of region and blowdown chute

The viewing region is a "sandwich" type design. A 1.27 cm x 2.54 cm (1/2 inch x 1 inch) steel bar (1.27 cm being the depth) is welded to the top of the baseplate such that it is aligned and centered with the blowdown chute slot in the baseplate. The inside dimension of the frame formed by this bar is 30.5 cm x 50.8 cm (12 inch x 20 inch). Three threaded 0.635 cm diameter holes are provided on the top edge of the frame for a fluid intake port, a 13.8 bar (200 psi) safety pressure relief valve, and an instrumentation port. Lexan® glass 53.3 cm x 35.6 x 3.81 cm provides the two windows which are placed flush to the frame and baseplate on either side of the frame. Lexan® glass is a specially heat resistant, high strength type of plexiglass. It was chosen because of its good structural characteristics. It has a modulus of elasticity of 2.3×10^4 bar (3.4×10^5 psi), yield stress of about 790 bar (11,000 psi), and maximum heat resistance of 121 °C (250 °F). An external frame of 3.81 cm x 3.81 cm x 0.635 cm (1-1/2 inch x 1 1/2 inch x 1/4 inch) angle iron is placed around the top and sides of the glass windows. Twenty-five 12.7 cm x 0.9525 cm diameter (5 inch x 3/8 inch diameter) bolts are applied with approximate equal spacing through the angle iron frames, glass, and internal frame to apply pressure for the seal. The glass is restrained on the baseplate by a 0.159 cm (1/16 inch) steel plate bolted with four 2.54 cm x 0.9525 cm (1 inch x 3/8 inch) bolts to the baseplate. These plates prevent outward motion or bulging at the bottom of the glass during pressurization. A seal of General Electric RTV Silicone

Rubber Sealant is applied between the internal frame and baseplate where the glass and steel are in contact. Also, between the glass and baseplate, a 0.0794 cm (1/32 inch) rubber gasket is inserted to insure adequate pressure is developed to hold the silicone rubber in place. Under pressure, the silicone sealant provides adequate shear strength for sealing. The viewing region is designed for approximately a 10.3 bar (150 psi) maximum pressure with a safety factor of 3 (450 psi ultimate).

The fluid intake port is a 12.7 cm x 0.635 cm (5 inch x 1/2 inch) pipe which is closed with a 0.635 cm diameter plug during an experiment. The plenum instrumentation, composed of a pressure transducer, thermocouple, and air bleed valve, is located on the end of a 12.7 cm x 0.635 cm (5 inch x 1/4 inch) pipe connecting it to the plenum. The pressure transducer is at a right angle connected with a 0.635 cm x 0.9525 cm (1/4 inch x 3/8 inch) tee. The air bleed valve is connected at a right angle to the pipe connected by a 0.635 cm x 0.635 cm (1/4 inch x 1/4 inch) tee. The thermocouple is located at the end of the two tee's extending approximately 7.6 cm into the gas plenum.

3.3 Rupture Disk Region

The rupture disk method of initiating the transient experiment provides a near instantaneous removal of the barrier between the gas and the liquid. Appendix A contains a brief analysis of the breaking phenomenon and time required for breaking. This technique requires the use of calibrated rupture disk and a precise initial static pressure measurement.

The rupture flange assembly, shown in Figure 3.5 as a sectional view, is a standard double disk rupture flange assembly for prebulged disk. The disk assembly consists of three 27.9 cm (11 inch) outside diameter 15.2 cm (6 inch) inside diameter flanges made by Fike Metal Products Corp. A 1.27 cm (1/2 inch) hole is provided in the middle flange for pressurization and instrumentation. The assembly is located between the upper flange (below the blowdown chute flange) and top core flange which are matching 27.9 cm (11 inch) diameter x 2.54 cm (1 inch) thick flanges. The upper flange is slotted to match the blowdown chute. These five flanges in total are secured together with eight 20 cm (8 inch) x 1.91 cm (3/4 inch) diameter bolts which also support the core. The aluminum prebulged rupture disk are also purchased from Fike Metal Products Corp.

Any given experiment required two disks. Each disk's rupture pressure was calculated from experimental initial conditions. The disks are factory calibrated. The disks were placed in the rupture flanges and the flanges bolted together securely. The center volume between the rupture and the core volume were pressurized such that neither disk rupture pressure was exceeded. The volume between the top disk and the aluminum foil was at atmospheric pressure. The pressures were adjusted so that when the center volume was depressurized by venting to the atmosphere, the rated rupture pressure of the lower disk was exceeded by at least 5%, thus initiating the transient. A shock wave breaks

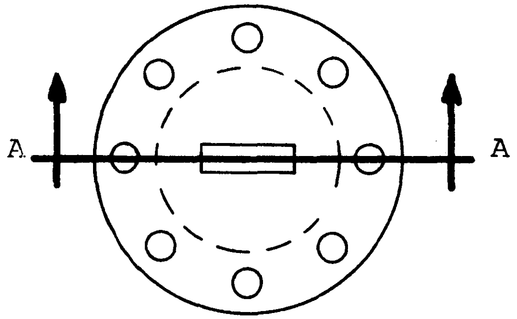

Top View of Rupture Flanges
(Simplified)

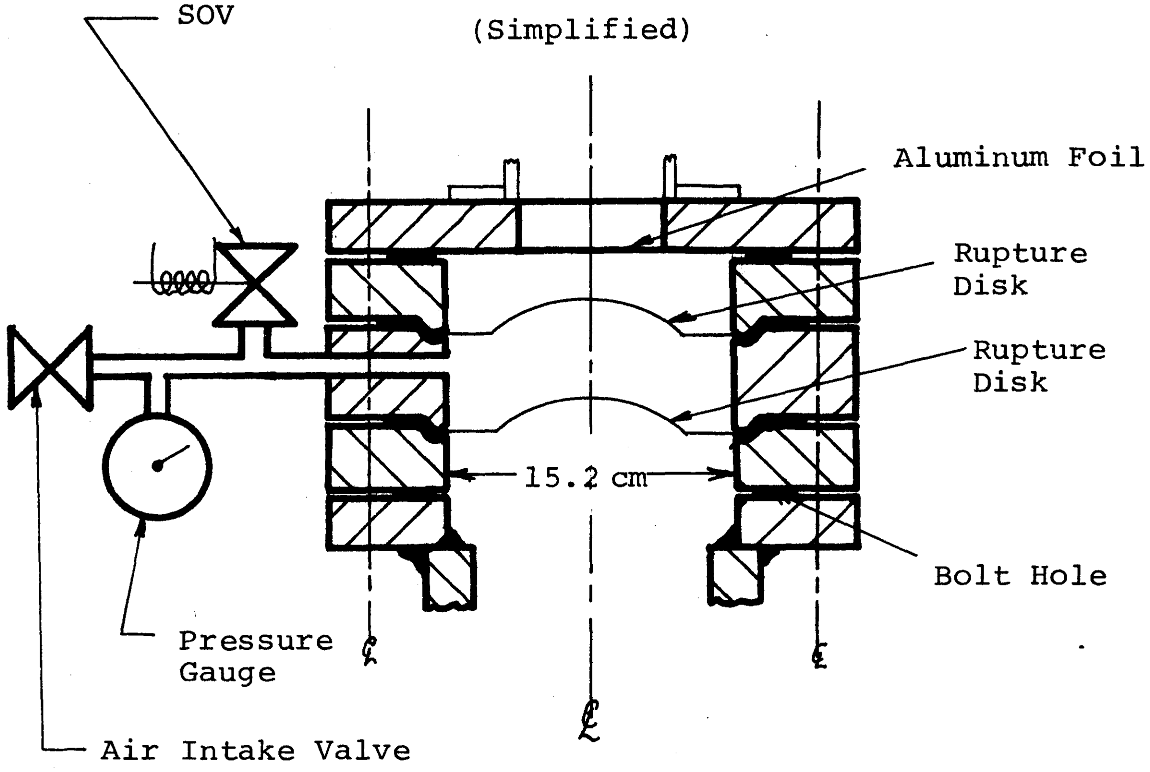

Section A-A View of Rupture Disk Flanges

Figure 3.5: Sectional view of rupture disk flange region

the top rupture disk and aluminum foil allowing the gas to expand into the viewing region. The breaking of these three barriers was instantaneous on the time scale of the experiment. Also, because the core volume becomes the volume of the core plus the volume of the rupture disk region, an initial pressure lower than the pre-blowdown should be measured. Isentropically and ideally, the pressure in the new core volume should be approximately 73% of the pre-blowdown pressure of the core.

3.4 Core Region

The core, shown in Figure 3.6 is a cylindrical vessel where the gas is kept so that initial experiment conditions can be obtained prior to initiation of the experiment. The pipe is a nominally 15.2 cm (6 inch) XX heavy steel pipe 30.5 cm (12 inches) long. The inside diameter is 12.7 cm (5 inches). The lower end is closed with a 27.9 cm (11 inches) outside diameter x 2.54 cm (1 inch) thick plate bolted with eight 7.62 cm (3 inch) x 1.91 cm (3/4 inch) diameter bolts to a 27.9 cm (11 inches) diameter x 12.7 cm (5 inches) inside diameter flange. This flange is continuously welded to the pipe. A 1.27 cm (1/2 inch) diameter hole is provided in the bottom plate for draining. Holes are provided in the pipe vessel for pressurization and instrumentation. The instrumentation consists of two thermocouples, a pressure transducer, and a static pressure gauge. The top end of the vessel is continuously welded to the top core flange previously described. To replace the rupture disk,

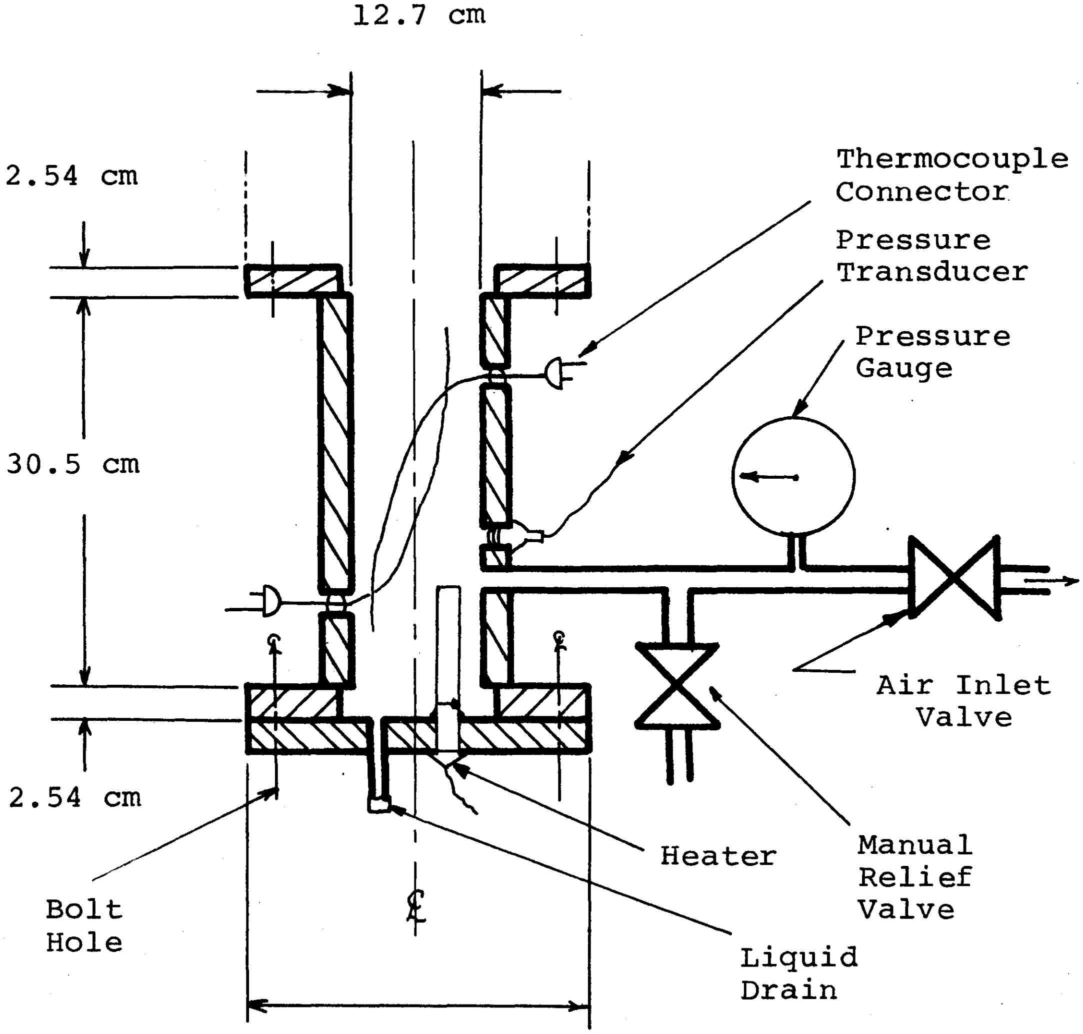

Figure 3.6: Sectional View of Core Region

the core vessel is lowered with a hydraulic jack, otherwise it is held in place by the bolts used on the rupture assembly flanges. A Hotwatt IS756 500 watt heater is inserted in the bottom flange to heat the gas of the core.

3.5 Instrumentation and Measurement

Pressure during the blowdown transient was measured with three PCB Piezotronics Model 102A12, low impedance, quartz pressure transducers. These transducers are capable of measuring rapid changes in pressure with a rise time on the order of one microsecond. One transducer located at the plenum instrumentation port measures the gas pressure as the liquid level rises compressing the cover gas volume. The transducer located 3.8 cm below the bottom of the viewing region on the blowdown chute centerline in the blowdown chute measured chute pressure. This is located as close to the discharge volume as is physically possible. The core pressure transducer is located approximately 10 cm from the bottom of the core tank. It measures the depressurization of the core. These transducers were powered by three PCB Piezotronics Model 482A Power Supply/Amplifiers.

Initial core and rupture flange center volume pressure measurements were made with two Helicoid® bourdon pressure gauges. One is located on the pipeline to the center volume between the center volume and the solenoid valve. The other is located on the inlet gas pipeline to the core volume. These pressure gauges allow proper setting of the pressure, both to prevent premature breaking of the rupture disks and to insure breakage upon depressurization of the center volume in the rupture assembly. The static pressures were recorded by hand.

The output from the power supply/amplifier of the transducers was processed by an impedance matching circuit [19] shown in Figure 3.7. This circuit has a gain of unity. The output of this circuit was fed to a Honeywell Model 906C Visicorder Oscillograph. The Visicorder records the signal from all three pressure transducers in three separate channels on rapid access type recording paper which gives a permanent record of the pressure history during the transient. The paper recording speed was set at 127 cm per second (50 inches per second or 20 milliseconds per running inch). A 1000 Hz square wave signal was supplied in the fourth channel of the Visicorder as a reference timing signal on the recording paper. The 1000 Hz signal was supplied by a Tektronix Type 585 Oscilloscope.

Initial pre-blowdown temperatures were measured with Omega Model ICSS-316G-12 iron-constantan thermocouples. The plenum thermocouple is located approximately 7.6 cm below the top of the plenum and measures temperature of the cover gas. The other two thermocouples are located in the core about 3 cm below the top and 3 cm above the bottom of the core. This allowed accurate temperature measurements of the gas before blowdown. Because of the expansion of the gas volume prior to the actual discharge, a correction in this measurement was required. Isentropically and ideally, the actual temperature should be approximately 91% of the initial temperature. The temperature was not measured during the transient since the thermocouples

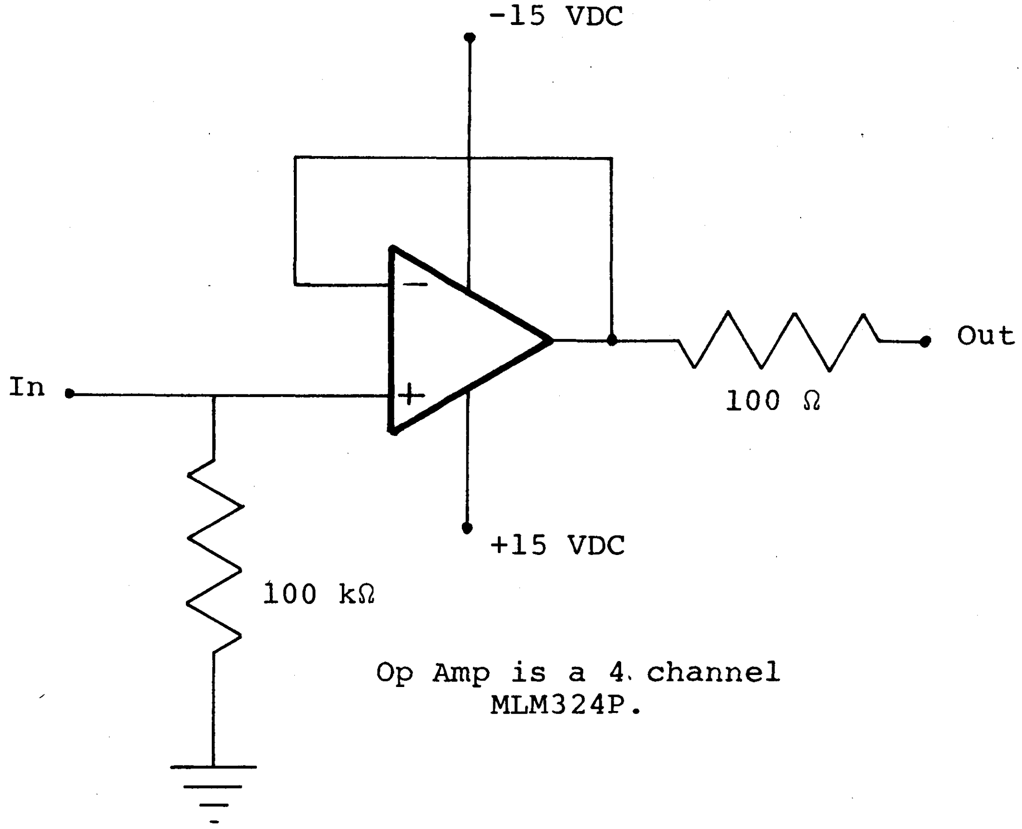

Op Amp is a 4 channel
MLM324P.

Figure 3.7: Impedance Matching Circuit

This circuit is independent for each of the four channels into the visicorder.

have a relatively long time constant (10 seconds). The output of the thermocouples is connected to an Omega Model MCJ Cold Junction Compensator. The output of the cold junction compensator is connected to a Hewlett Packard Vacuum Tube Volt Meter Model 412A. The voltage was read directly from the VTVM meter and recorded by hand.

To observe the gas discharge in the viewing region, high speed photography was employed. The camera was a Hycam High Speed 16 mm movie Camera Model K20S4E-115 which used Kodak 4-X Reversal Film 7277 in 100 foot rolls. The camera speed was set at 5000 frames per second. A Millimite TLG-4 pulse generator supplied the internal timing pulse of 1 pulse per millisecond on the film.

The viewing region was illuminated from the rear with six 600 Watt lights. The lights were (4) Colotran Mini-Pro 100-091 and (2) Smith-Victor Corp. Model 700. No frontal lighting was used. Camera f-stop settings were made with a Honeywell Pentax Hycam 1°/21° Lightmeter.

The volume measurements were made using a 1 cm grid affixed to the rear of the back window in the viewing region. The transient volumes were measured by hand from the photography.

Sychronization between the recording instruments and the blowdown was accomplished by one common source. The Hycam camera has an external trigger circuit which automatically closes an internal switch at a predetermined place on the film. This circuit provides a 110 VAC output. An external lamp (20 Watt) in the view of the camera during the blowdown gives an

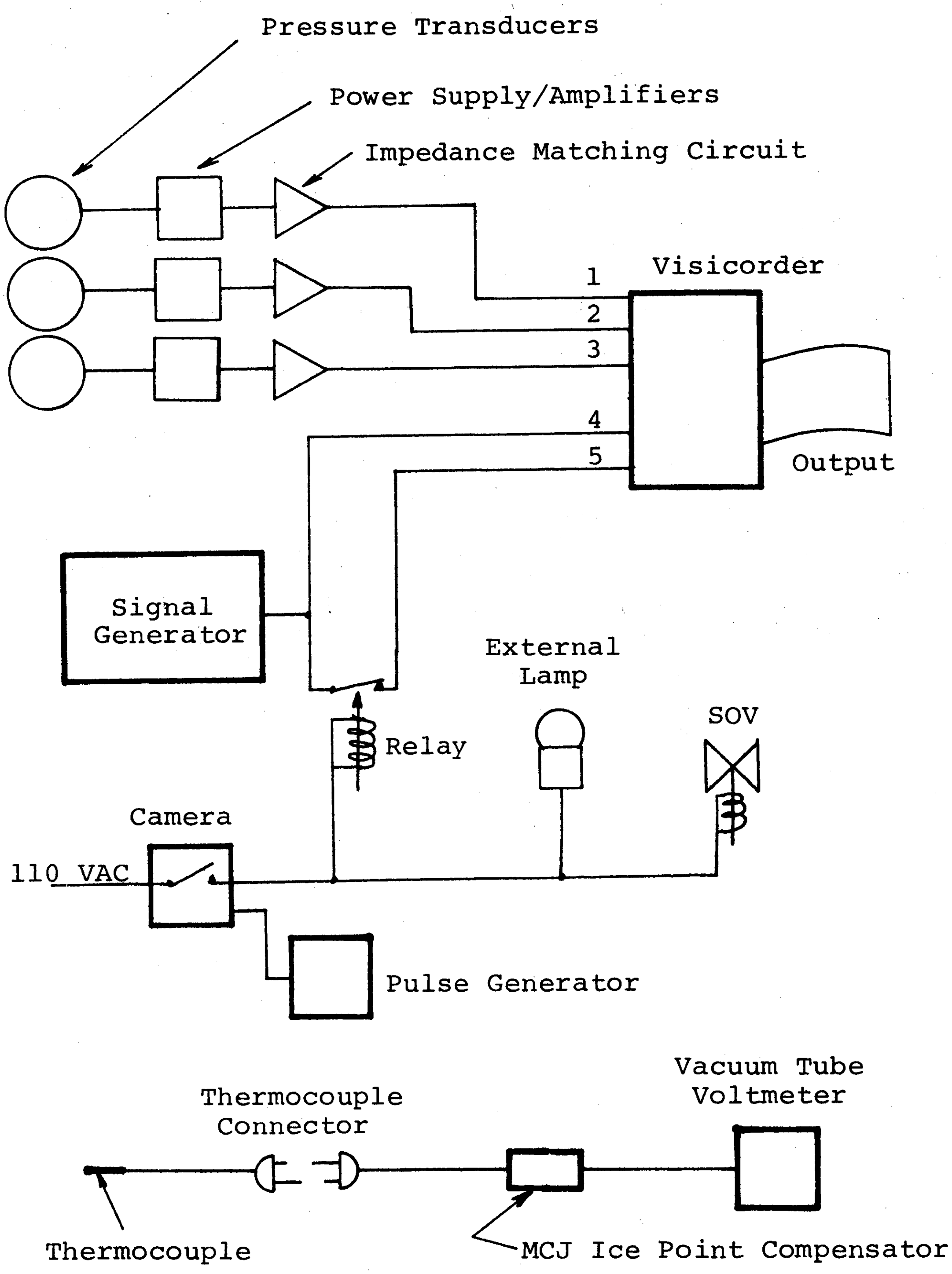

Figure 3.8: Instrumentation hookup and layout

indication on film of the initiation point. The 1000 Hz signal to the Visicorder channel five was placed in series with 110 VAC normally closed relay. When the camera internal switch closed, the relay opened and the signal was discontinued on the Visicorder output. The internal switch also provided power to the electric solenoid valve which initiated the blowdown by venting the slightly pressurized center volume of the rupture assembly to the atmosphere. The Visicorder does not have a remote starting circuit so it was started by hand, as was the camera motor also. These two devices were started as near simultaneously as possible by the operator of the experiment.

IV. EXPERIMENTAL PROCEDURE AND UNCERTAINTIES

4.1 General Experimental Procedure

The experimental procedure is relatively simple and easily reproducable for various experiments. The eletronic equipment was allowed to warm up for at least one hour prior to initiation of any set of experiments. The liquid, in the case of water, was also allowed to come to thermal equilibrium with the laboratory environment before inserting into the viewing region. With the rupture disks in place, the rupture assembly securely bolted together, and the high speed movie camera loaded and set, the pressure in the center volume and lower tank was brought to the desired level by means of a high pressure gas bottle. Temperature measurements of the air above the liquid and gas (heated and unheated) in the lower tank were then made and recorded.

With the initial experimental conditions met, the backlighting was switched on. The camera and Visicorder were then simultaneously switched on. The camera automatically initiates the experiment as was described in Section 3.5. A complete procedure for setup and operation is given in Appendix B.

4.2 Instrument Calibration

The initial temperatures of the experimental conditions were measured with conventional iron-constantan thermocouples. These thermocouples were calibrated with a boiling bath and an ice bath. From known atmospheric pressure conditions, the boiling point and freezing points of the water baths were found.

Manufacturers data specifies a 0.75% error in the reading. Assuming a linear temperature versus millivolt output relationship, (also manufacturer specifications over the present temperature range) a conversion factor was calculated (Reading mV x 17.37 = °C). Over a one hour period, no significant drift in these measurements was observed.

The bourdon type Helicoid® static pressure gauges used to measure initial experimental pressures were calibrated with a dead weight Ashcroft Gauge Tester Type 1300 Serial Number 16697. The gauges, after adjustment, indicated the correct pressure over the full 200 psi range to within 1/2 psi.

The quartz piezoelectric pressure transducers were factory calibrated by PCB Piezotronics. These calibrations were assumed correct since no apparatus was easily accessible for calibration. All calibrated voltage readings were linear with pressure to within 1% over the full range of pressures.

The vacuum tube voltmeter was gauged against other voltage measurement devices. (Recent Model Hewlett Packard Digital Voltmeter) No significant deviation from the proper reading was seen and no significant drift over one hour was noted.

The Visicorder required installation of "scaling" resistors to adjust the deflection of the oscillograph to the proper input voltage. After the proper resistors were installed (resistance values were calculated according to the instruction manual), a deflection calibration was made to check linearity and response of the Visicorder. These were steady state measurements of known input voltages. The calibrated deflections were used for transient measurements. The Visicorder specifications call for a maximum overshoot of 7% for a full scale deflection

All of the calibration data and results are given in Appendix C.

4.3 Experiments Undertaken

All experiments undertaken in the present work used identical geometries but different initial pressure and temperature conditions. The liquid pool height was set at approximately 30.5 cm (12 inches) for each run. The upper gas plenum was always at atmospheric temperature and pressure. The gas volume above the liquid in the viewing region available for discharge was the same for each run.

The hydrodynamic experiments consisted of injecting a noncondensible gas (air) into a subcooled liquid (water) at ambient temperatures but elevated pressures. The initial core pressures were set approximately at 3, 4, 6, 8, and 10 bar. Table 4.1 is a list of the successful experiments undertaken. Substantial difficulty in the 3 bar runs was experienced. The low pressure did not always completely remove the thin foil barrier between the gas and liquid, thus leaving some blockage of the blowdown chute (typically 50%). Higher pressures always removed the foil barrier.

In order to observe the effects of the blowdown chute on the entrainment rate, separate experiments with the aluminum foil barrier at the top of the blowdown chute were also made. Table 4.1 includes these experiments and initial conditions.

TABLE 4.1

Successful Experiments and Relevant Experimental Conditions

Run Number	Type	Initial Core Pressure (Bars)	Initial Core Bulk Temp (°C)	Head of Liquid (cm)
9	H-3	3.03	23	31.8
10	H-3	3.03	25	32.0
11	H-4	3.98	28	31.0
12	H-4	3.93	28	31.5
13	H-4	3.93	28	31.5
14	H-6	5.86	30	31.5
15	H-6	5.86	29	31.0
17	H-8	7.93	31	31.5
21	H-8	7.94	29	29.5
24	H-10	9.65	37	30.5
25s	H-4	3.93	33	33.5
(25s Chute Effects Test)				
26	H-10	10.7	30	30.2
27s	H-8	8.60	36	27.5
(27s Chute Effects Test)				
1	TH/SC-4	3.93	30	30.8
2	TH/SC-4	3.86	31	31.0
3	TH/SC-6	6.00	31	31.4
4	TH/SC-6	6.07	30	32.0
6	TH/SH-4	3.86	52	32.3
7	TH/SH-4	3.93	55	31.5
8	TH/SH-6	6.07	61	31.3

Table 4.1 (continued)

Common Initial Conditions

Water Temperature	25±1 °C (average)
Freon Temperature	25±1 °C (average)
Plenum Gas Temperature (Air)	27±2 °C (average)
Plenum Gas Temperature (Freon)	27±1 °C (average)

Type Key

H-X H = Hydrodynamic
X = Pressure (bars)

TH/SC or SH-X TH = Thermal-Hydraulic (air into freon R-113)
SC = subcooled gas temperature
SH = superheated gas temperatures
X = Pressure (bars)

The thermal-hydraulic experiments consisted of injecting a noncondensible gas (air) at a temperature greater than that of the liquid (freon R-113) saturation temperature at elevated pressures. Both subcooled temperatures and superheated temperatures were used at 4 and 6 bar pressures. Table 4.1 also includes the list of successful thermal-hydraulic experiments. No major difficulties were encountered during the course of these experiments.

4.4 Experimental Failure Rate Analysis

In an attempt to assess the expendable materials (film, rupture disk) required for the experiments, a fault tree analysis of the failure possibilities was performed on the apparatus, recording instruments, and associated electronics. The analysis considered all possible modes of failure that would prevent the data from being recorded once the switch on the camera is turned on. The average failure rate was calculated to be 61%. The fault tree and failure probabilities are given in Appendix D. The failing of the rupture disk (specified by Fike Metal Products [20]) was found to be the prominent mode of failure. Other modes of failure, mechanical, electrical, or human, were dominated by human error in set-up or improper connections, even though a check list was used. Failure data was collected from the various manufacturers and the Reactor Safety Study [21].

4.5 Data Reduction Procedure and Data Uncertainties

Liquid entrainment measurements were made visually from the high speed movie film. From this film, the total pool (liquid and gas) volume and gas expansion (gas and entrained liquid volume) volume, as they vary with time, can be found. From the known initial liquid volume, the amount of liquid entrained can be calculated by subtracting the gas expansion volume from the change in the total pool volume. Figure 4.1 illustrates these two volumes. The total pool volume is known nearly exactly throughout the duration of the experiment until acceleration of the pool surface becomes negative at which time instabilities develop on the surface which destroy the boundary between the gas and liquid obscuring the measurement. This typically occurs just before the maximum expansion of the jet. The expansion volume error is relatively small also. However, the difference in the pool volume and the expansion volume is small and the error is therefore a significant portion (typically 20%) of the measured value. Also from the film, the penetration height (L) and typical penetration width (D) can be measured. Figure 4.1 also illustrates the dimensions of the gas penetration.

The pressure transducers measure pressure relative to the initial pressure prior to the transient. The actual pressure histories had relatively large fluctuations superimposed on the trace because of shock waves that developed when the diaphrams broke. The traces were smoothed and normalized by

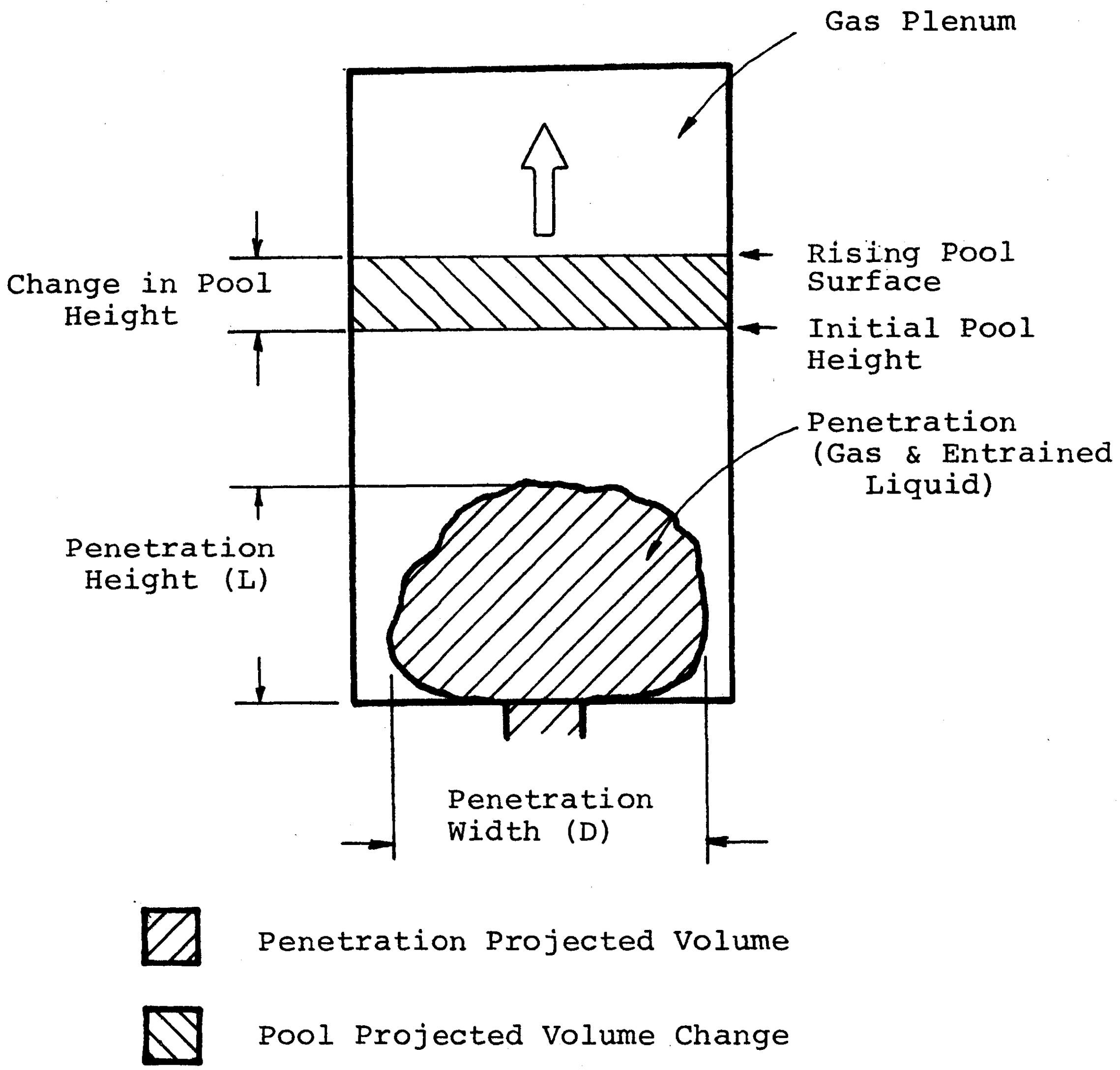

Figure 4.1: Definitions of penetration volume, the change in pool volume, and dimensions of penetration by gas.

accounting for changes in the volume of the gas at initial conditions prior to and after the rupture disks broke.

Uncertainties in the pressure measurement results are primarily from error in reading the pressure histories recorded by the Visicorder. Also, the pressure transducers measure only the local pressure and not the bulk pressure of the volume concerned. There is also a time delay in measurement because of the time required for a pressure wave to reach the transducer from its initiation point. The shock wave traverse time in the blowdown vessel is approximately 1.2 msec. In the gas plenum, the pressure wave traverse time is less than 1 msec. Thus, some time delay in the pressure measurement will result from these effects. This time delay plus the uncertainty in knowing the exact synchronization point in time between the film and pressure histories, yield timing uncertainties in all measurements on the order of ± 1/2 to 1 msec.

V. HYDRODYNAMIC EXPERIMENTAL RESULTS

5.1 Introduction

The experimental results are discussed in six basic sections: 1) a qualitative discussion of the blowdown, 2) a quantitative presentation of typical pressure histories, 3) a quantitative presentation of the entrainment measurements including error estimates, 4) the effects of the blowdown chute on the blowdown characteristics (i.e. entrainment), 5) growth characteristics of the bubble in the viewing region, and 6) a discussion of the significance of the results relative to models for assessment of the mechanical work potential following a hypothetical accidental disassembly of a fast reactor core. The experiments undertaken in the present work and the initial conditions are listed in Table 4.1. A sample of the pressure traces are shown in Appendix E.

5.2 Qualitative Description of the Hydraulic Blowdown

It is useful to consider the qualitative aspects of the results before the quantitative results are discussed. Not only is some interesting information obtained, but this also allows introduction of some terms and concepts which will be used in subsequent analysis. It should be stated that the "average" experiment exhibited the characteristics to be described in this section. There were some variations not discussed with regard to the development of the discharge. There were runs in which portions of the rupture diaphrams were seen being injected into the viewing region late in the transient. Other experiments did not produce a symmetric development of the initial jet as it penetrated the liquid pool. There were never any grossly atypical developments in any experiment.

In general, the higher pressure experiments, 6, 8 and 10 bars, leaked slightly after several runs. The leaks were detected in the photography in most cases and generally occurred 20 to 30 milliseconds after the liquid slug impact on the underside of the top of the viewing region. Retrieved liquid volumes were checked to measure the losses. The subjective judgement of the operator was used to determine if a leak was too large. Runs with large leaks were discarded as this could contribute significant momentum losses.

In all experiments, prior to blowdown a meniscus was formed by the water between the Lexan® windows. Initiation of the experiment was detected when the meniscus disappeared (a slight rise in pool level). The meniscus then would bulge up as the volume of the pool rose yielding a very distinctive line. The pool level then rose some finite amount before the jet came into view. The pool, except in the 10 bar runs, remained level as it rose. In the 10 bar runs there was a slight bulge at the center with respect to the pool surface near the sides. Also, at higher pressures, the pool surface seemed to move down before moving up.

As the jet entered the viewing region, it had already developed a rough leading edge and seldom entered as a rigid block or slug shape. Two nodes, symmetric with respect to the centerline, formed and moved laterally and vertically. The time before the bubble entered the viewing region decreased with increasing pressures. Also, in this initial development period, the jet was black, thus indicating a large quantity of water droplets had been entrained in the chute by the gas. Once the bubble was approximately two or three times wider than its height, the jet began to clear (became less black) near the sides of the chute in the nodes. However, the leading edge was still quite black and rough. The side edges, as now the bubble is somewhat rectangular in shape, were black and more smooth than the leading edge.

When the bubble occupied approximately 75% of the pool cross section, lateral expansion slowed down. The cleavage of the two nodes began to disappear leaving a nearly flat leading surface. The leading surface then bulged in the center as the bubble became more spherical in shape. The center part of the leading edge was being pushed by a second internal jet. The leading edge was now undergoing an upward acceleration and consequently an increase in velocity. In the lower pressure runs, the band of blackness at the edge of the bubble was not as wide as the band of blackness at the leading surface for higher pressure runs. Also, the leading edge was more smooth for low pressure runs. This blackness and roughness on the leading surface could be attributed to development of Taylor instabilities at the gas/liquid interface.

With the bubble becoming spherical the central portion of the bubble became moderately clear. The flow from the internal jet could be distinguished quite well. On the sides of the chute, a darker internal laminar stream or jet was seen entering the expanding volume. The darker stream was attributed to water being removed from the walls of the chute. Although more pronounced in the high pressure runs, this was seen in all runs. This internal stream continued upward to the leading edge becoming turbulent in appearance and contributing to the momentum of the expansion upward.

When the pool level rises, the gas in upper gas plenum of the viewing region is compressed. As the pool level approached the upper boundary, the surface became less and less distinctive in its image. Instabilities were seen forming on the surface during this portion of the blowdown. The instabilities appeared sooner for higher pressures. Also, at high pressures, water was seen splashing upward from the surface at regular time intervals. This was caused by the pressure wave traversing the pool and hitting the interface. Eventually, the pool surface could not be determined accurately. For the higher pressures, the unagitated liquid beneath the surface was seen to impact the upper viewing region boundary just before the bubble became disrupted. The pool surface did not quite reach the upper boundary for low pressures.

When the edge of the expanding volume stopped lateral expansion, the discharge took on a one-dimensional movement upward maintaining its spherical shape on the leading surface. At higher pressures the leading edge curvature was less. As the expansion reached its maximum volume, the perimeter of the bubble became quite smooth eliminating the band of blackness. The bubble now occupying 75% of the pool volume for high pressures (50% for low pressure) collapsed in on itself. The collapse began near the centerline as a jet moving downward creating two large nodes in the upper part of bubble. At this point the entire gas-liquid system loses all symmetry and becomes a "mush" of bubbles.

It should be noted that internal swirling was seen for low pressure runs during the first 30% of the expansion time. High pressures did not produce this effect as much as the low pressures. The internal jet emanating from the chute appeared to contribute to the internal swirling since the darker streams were seen to deflect laterally at the leading edge. In the initial development stages, the expansion moved laterally by a "rolling" of the top edge onto the viewing region bottom like a tread. This motion caused some swirling and was seen as the central portion of the sphere cleared. As the expansion reached its maximum lateral movement, this tread effect reduced greatly as did the swirling also.

The central portion of the bubble was never completely clear during the course of any run. The visual density of the bubble was increasingly darker near the edge and the edges of the chute.

Figures 5.1a to 5.1f are photographs taken from run 11 (4 bars) for several time steps. Figure 5.2a to 5.2f are photographs taken from run 17 (8 bars) for several time steps. For nearly equal time steps, note the more rapid lateral growth in run #17. Note the spherical shape development and its curvature at the end of the transient between the two runs. The internal jet from the chute can also be seen quite clearly in these photographs.

5.3 Typical Pressure Histories

Pressure histories of all runs were similar in shape for high and low pressures for each respective transducer.

The plenum pressure, shown in Figure 5.3 normalized against the initial core pressure, increased rapidly after approximately 10 milliseconds. Typically, the pool surface did not rise significantly until 5 milliseconds into the blowdown. At which time, depending on the initial core pressure, the plenum pressure increased slightly. Since the jet development was well underway 5 milliseconds into the blowdown, the pool surface was undergoing an upward acceleration and increasing velocity. Over the time scale of the experiment, this compression can be assumed to be adiabatic and isentropic. The plenum pressure should rise as the volume decreases according to the thermodynamic relation for isentropic compression,

$$pV^{\gamma} = \text{constant} \quad (\gamma = 1.4 \text{ for air}).$$

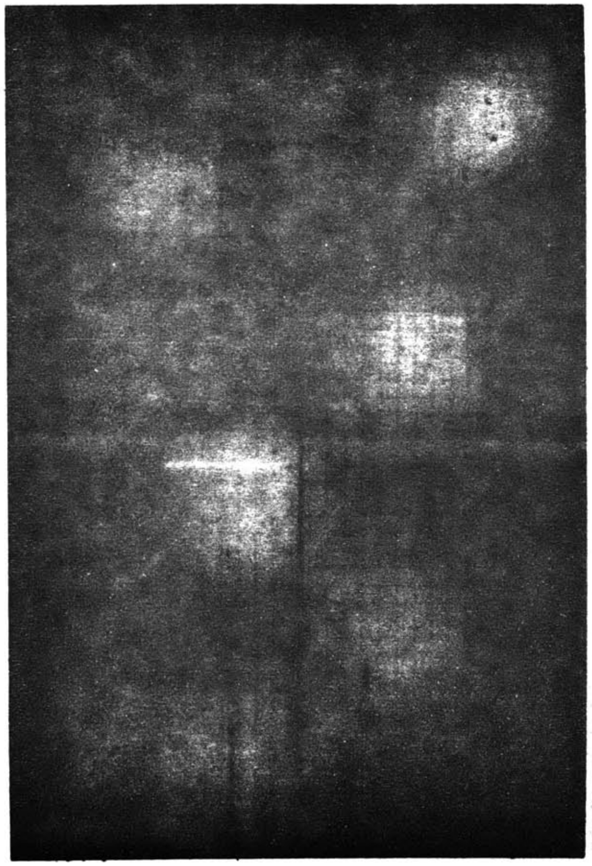

Figure 5.1a
Run #11
P = 4 bars
Time = 4.0 msec

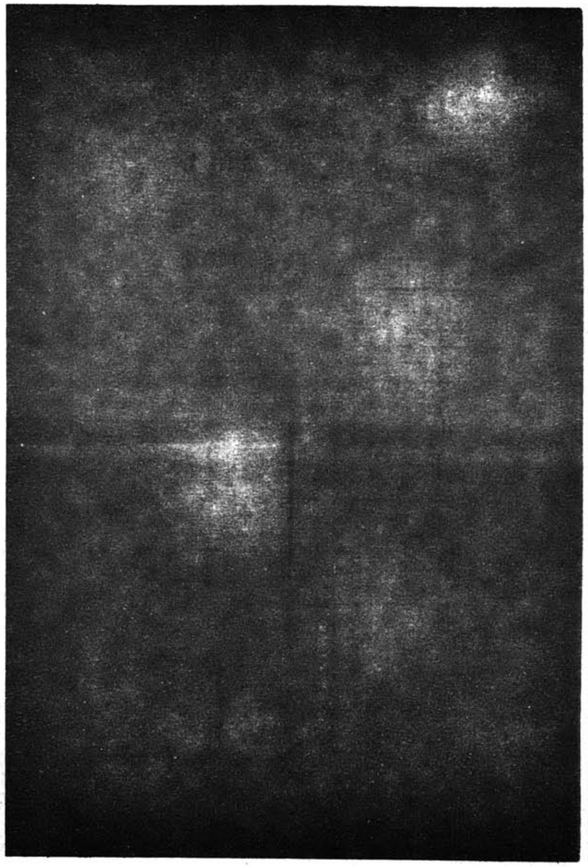

Figure 5.1b
Run #11
P = 4 bars
Time = 7.9 msec

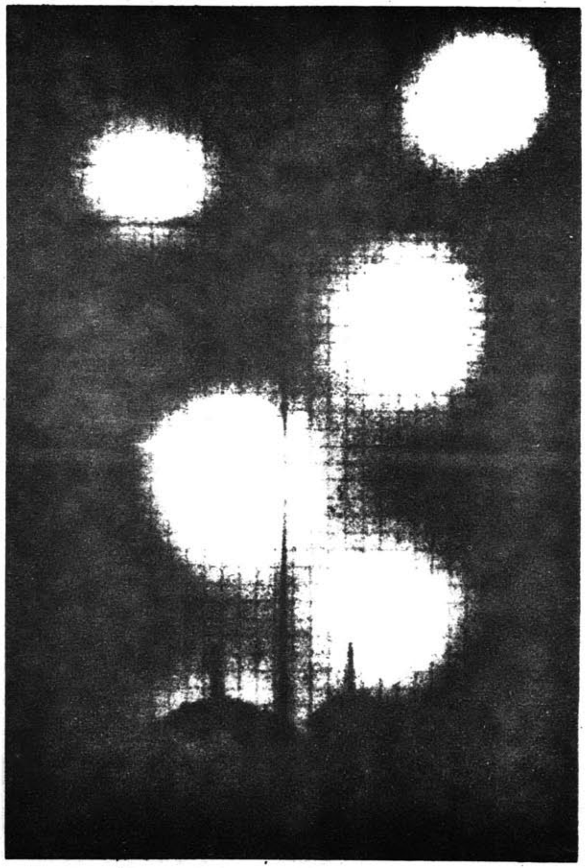

Figure 5.1c
Run #11
P = 4 bars
Time = 10.5 msec

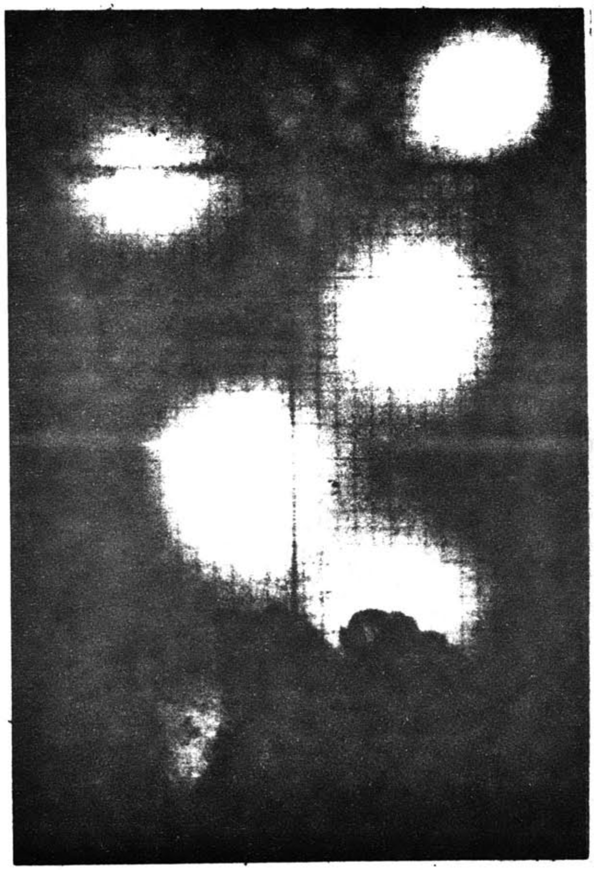

Figure 5.1d
Run #11
P = 4 bars
Time = 14.5 msec

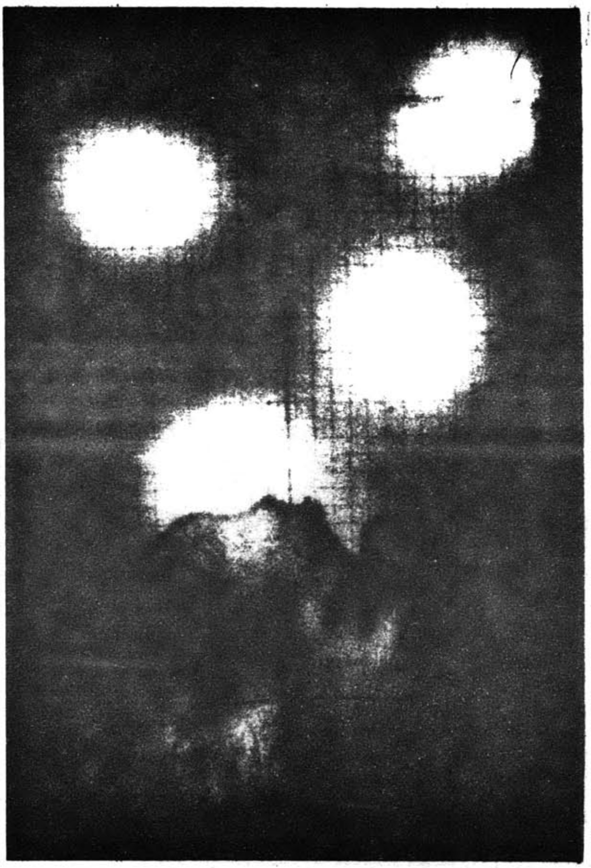

Figure 5.1e
Run #11
P = 4 bars
Time = 19.7 msec

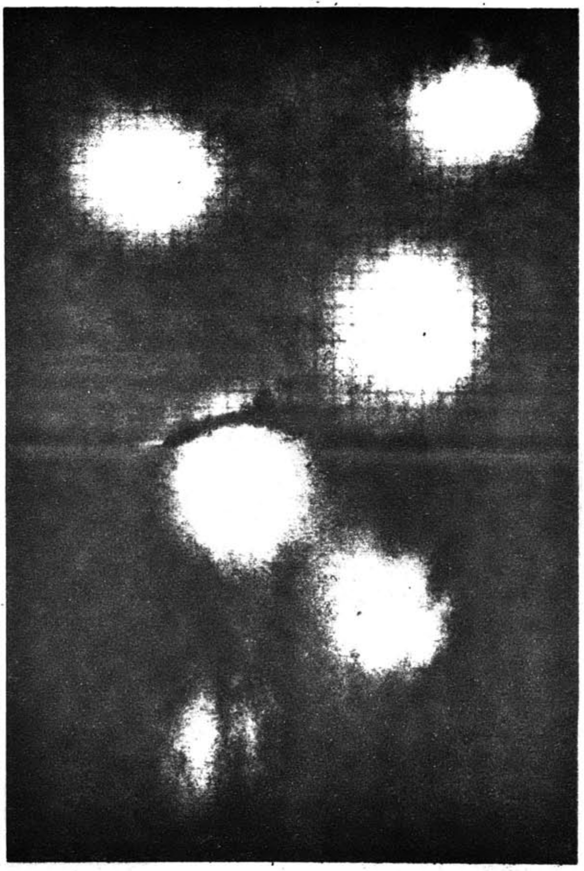

Figure 5.1f
Run #11
P = 4 bars
Time = 26.3 msec

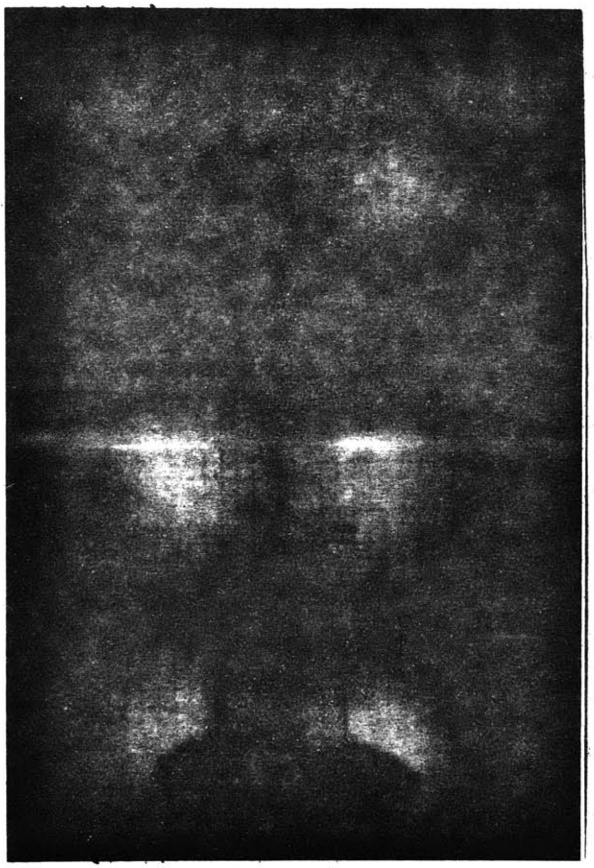

Figure 5.2a
Run #17
P = 8 bars
Time = 2.6 msec

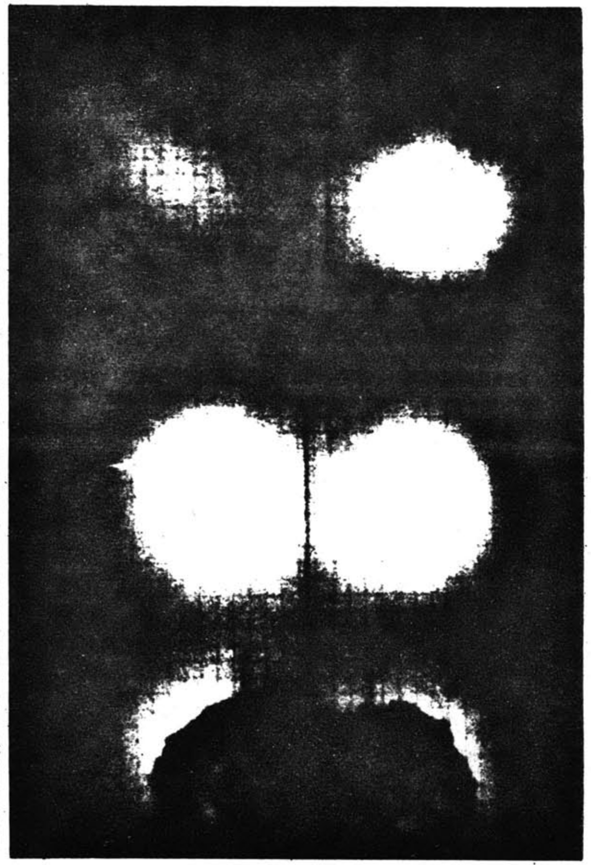

Figure 5.2b
Run #17
P = 8 bars
Time = 5.0 msec

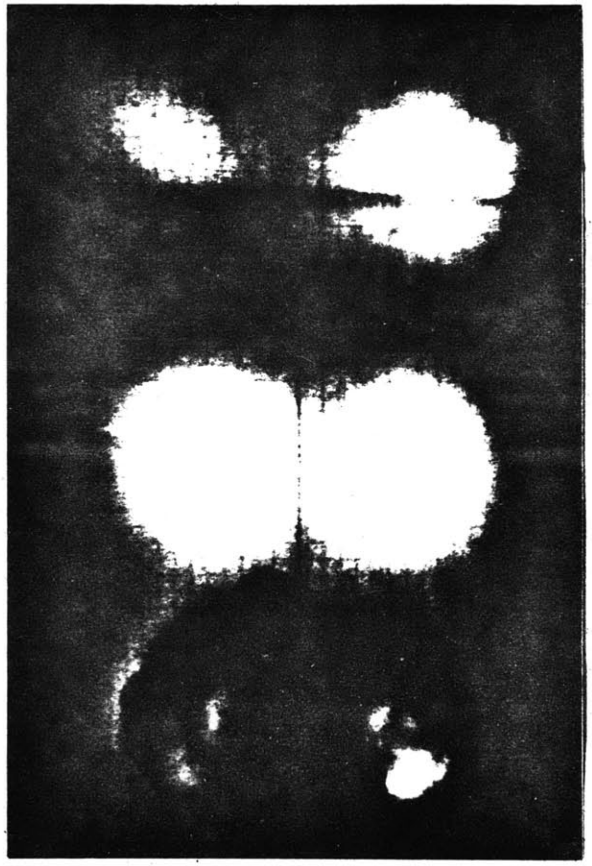

Figure 5.2c
Run #17
P = 8 bars
Time = 7.4 msec

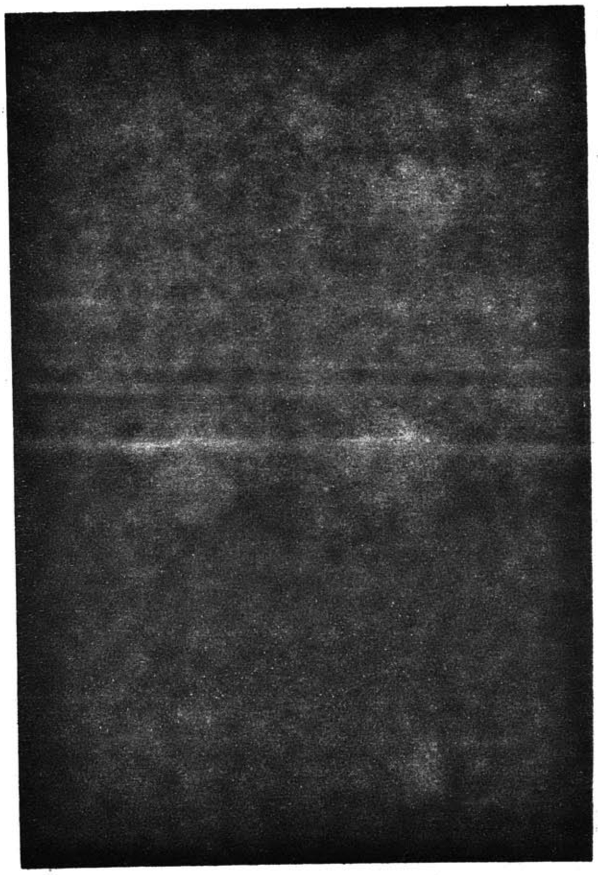

Figure 5.2d
Run #17
P = 8 bars
Time = 9.7 msec

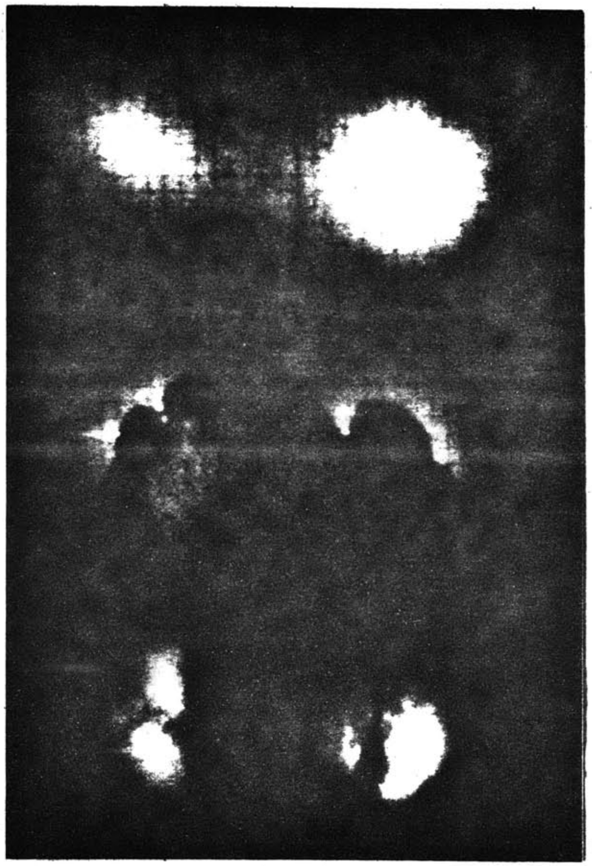

Figure 5.2e
Run #17
P = 8 bars
Time = 12.9 msec

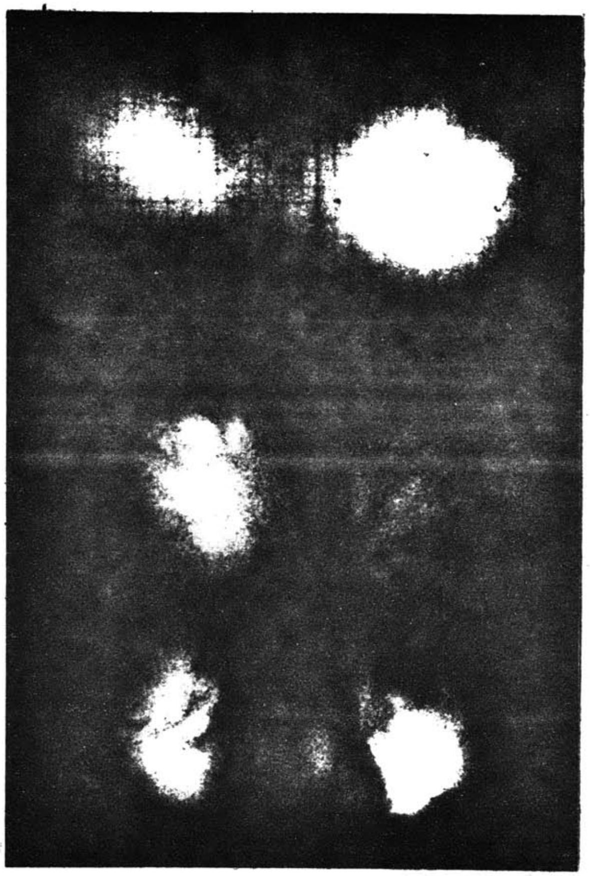

Figure 5.2f
Run #17
P = 8 bars
Time = 16.3 msec

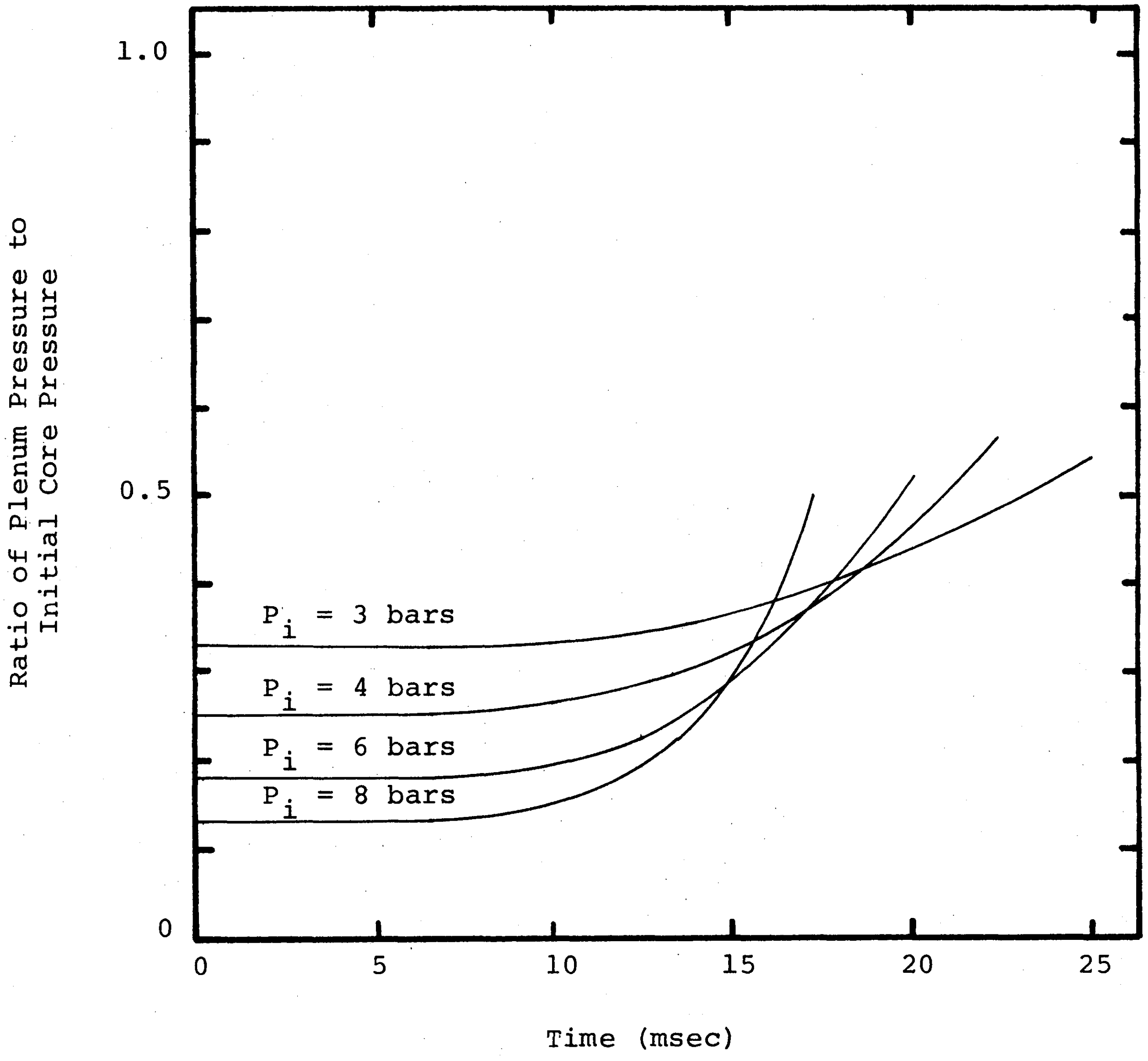

Figure 5.3: Ratio of plenum pressure to initial core pressure versus time for initial core pressures of 3, 4, 6, and 8 bars

From Figure 5.3 this is seen quite clearly.

The rate of compression increased with time for higher pressures. In fact, from the original pressure traces, the peak pressure in the plenum occurred much sooner in the high pressure runs. No shock waves were detected in this data.

The error in this measurement was principally from reading of the recorded output. Since no experiment lasted through the pressure peak, no overshoot of the signal trace occurred. Overshoot is caused by large fluctuations in a short time. Error from the scaling resistors could contribute as much as 10% in the absolute pressure measurement.

The blowdown chute pressure transducer, located approximately midway between the viewing region bottom and top of the rupture flange assembly on the centerline, produced a slight decreasing pressure of approximately 0.6 P_i after the jet cleared the chute, as shown in Figure 5.4. This pressure data was also normalized to the initial core pressure. The band or range of data is indicated on this figure for the different pressure runs. Error in this measurement was principally from reading the recorded output. The resistor scaling could contribute as much as 10% error to this measurement. However, this pressure trace also included reflections of the shock wave and thus has superimposed oscillations. This data was averaged or smoothed to account for the shock wave. Since the deflection of the Visicorder was at most restricted to two inches, overshoot was of little concern, (approximately

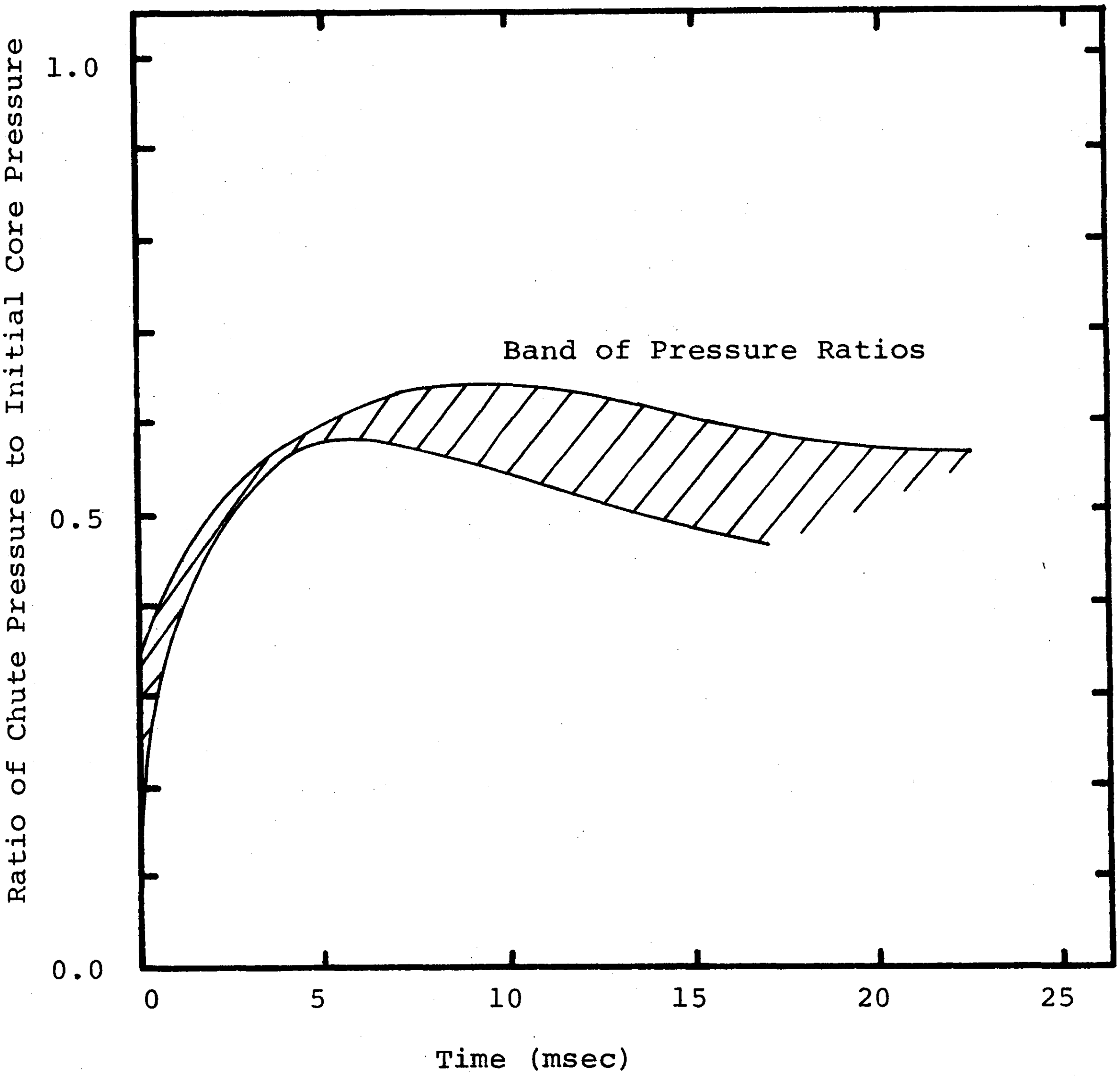

Figure 5.4: Ratio of chute pressure to initial core pressure versus time

2%).

Typical core depressurization, shown in Figure 5.5 normalized against the initial pressure and smoothed, exhibited even a lesser rate of depressurization than the blowdown chute (after jet penetration into the viewing region). Initially, when the rupture disk breaks, the volume of the core undergoes a rapid volumetric expansion. Since the conductive heat transfer in the steel structures is so slow compared to the expansion rates (time constant approximately equal to 2 seconds) the expansion can be assumed isentropic and adiabatic. If the rupture flange region were evacuated, the new pressure would be 0.74 P_i. However, this is not the case experimentally. The rupture flange volume is at an elevated pressure or near atmospheric at the time of the expansion. Experimentally, it was found that the pressure just after rupture was 0.87 P_i ± 0.02 P_i for all runs.

The original pressure traces did indicate a shock wave traversing the entire core volume. Thus, the analysis required smoothing to obtain an average pressure. In order to compensate for the change in volume, the product of pressure and volume was smoothed for the entire time interval and then normalized according to each respective volume at a given time. Error in this measurement as was with the other measurements was mostly from reading the recorded output. Overshoot error, again was insignificant. The smoothing was performed by hand calculator and thus could account for part of the error. The error is estimated to be no more than 10%.

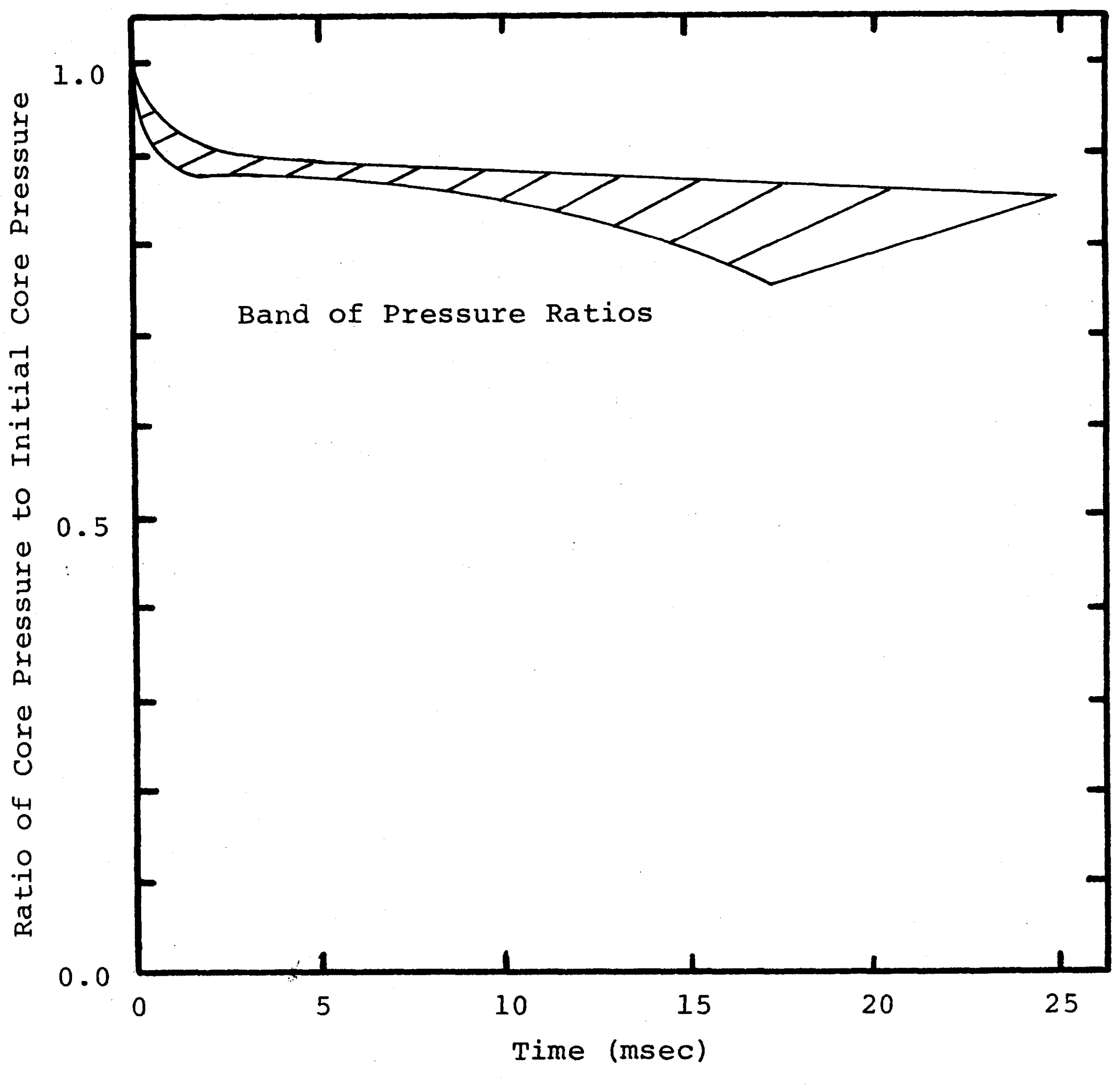

Figure 5.5: Ratio of core pressure to initial core pressure versus time

During the expansion, the change in core pressure because of gas loss through the solenoid valve was assumed insignificant over the time scale of the experiment. The blowdown chute area, 9.68 cm^2, is 3.4 times larger than the solenoid valve area, 2.85 cm^2, thus the pressure loss is small. Experimentally, the exit from the flange region to the solenoid valve is almost always blocked by the foil of the rupture disk as during rupture, it peels back to the inside walls of the rupture flanges.

The expanding volume in the viewing region typically reached a maximum of 10% of the core volume (5800 cm^3) for the maximum pressure run (10 bar). Thus, the loss of gas from the core would only contribute a maximum of 12% loss in core pressure. From these observations, the core should depressurize slowly, as was found.

Since the blowdown chute pressure was approximately half that of the core pressure during a blowdown, the transient was checked for choke flow through the blowdown chute. The critical pressure ratio for air (assuming ideal conditions) is 0.528. Thus, by taking the ratio of average blowdown chute pressure to average core pressure, Figure 5.6 results. As can be seen from Figure 5.6, a choked flow condition does not exist during the transient for any runs.

The adiabatic condition assumed for the duration of the transient is well justified. Heat transfer in the core and rupture flanges is quite slow because of the massiveness and thermal conductivity of the steel. Although smaller, the

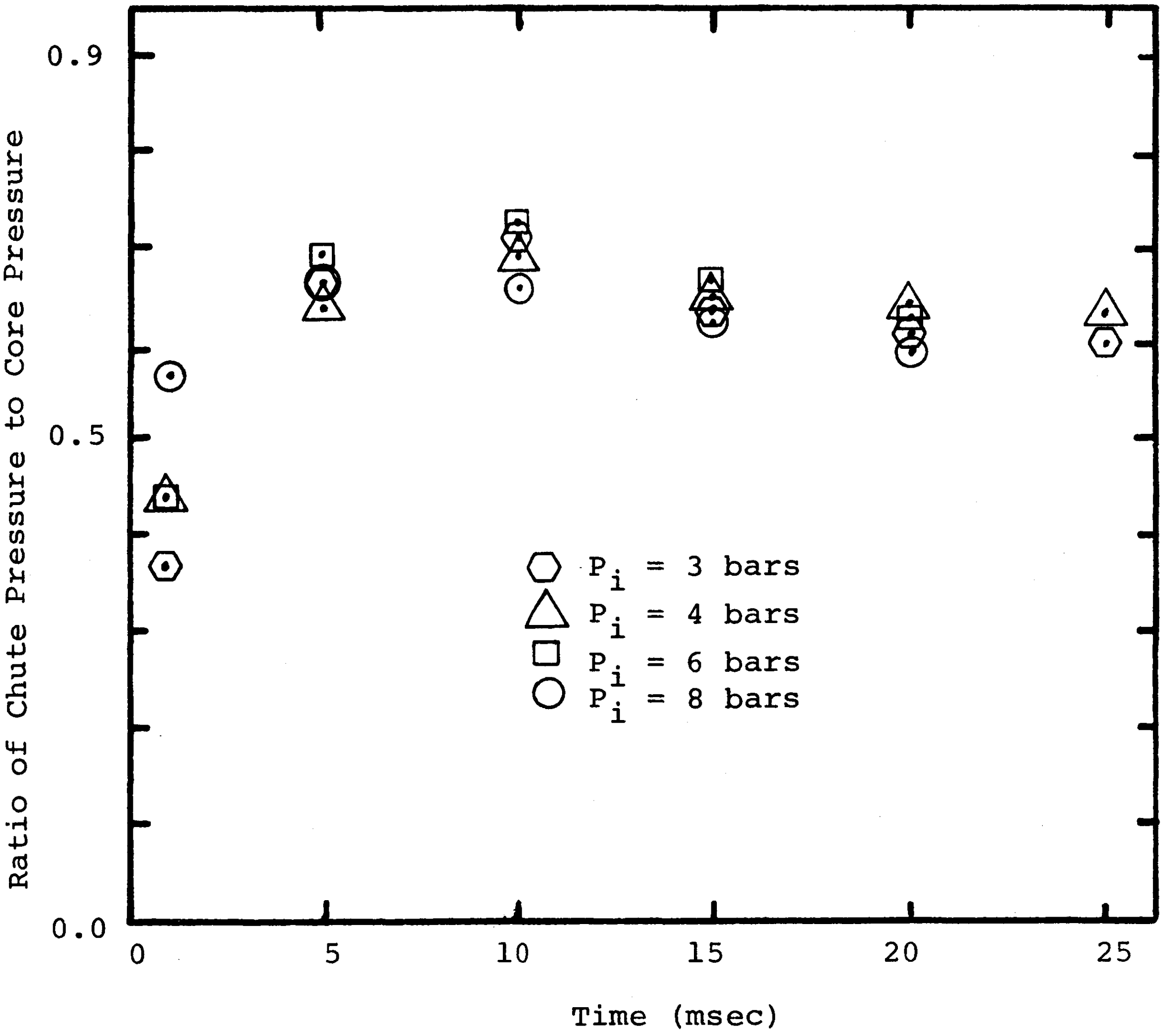

Figure 5.6: Ratio of chute pressure to core pressure versus time to test for a choked flow discharge

blowdown chute produces insignificant heat transfer from the steel to the air. This argument can also be applied to the heat transfer of the gas in the plenum during the experiment because the Lexan® has a lower thermal conductivity than steel.

5.4 Entrainment Results

Liquid entrainment by the gas as it enters and expands in the blowdown chute and the viewing region was determined by visual observation of the fast movie films of the experiments. The volume of liquid entrained is the difference in the liquid pool volumetric displacement and the gas jet volume. The liquid pool displacement was determined by calculating the overall pool volume from the observed height of the pool, as a function of time, and subtracting the initial pool volume. Both these quantities are known precisely up until near the end of the experiment when the pool surface experiences large instabilities. The gas jet volume was determined by adding up the projected area of the bubble with the help of the grid on the back window. Human error of judgement was introduced at this point while counting partial squares from the grid. Also, at times the bubble boundary was not well defined as lighting varied from run to run. The error estimated in observing this volume was calculated by assuming that the bubble may be considered a section of a cylinder. From the measured bubble volume, the radius of the section was found. The maximum error was then found as the difference between a calculated volume and the measured volume if the calculated volume had a radius equal to the inferred bubble radius plus one-half centimeter. The lower error bound was similar except the modified calculated radius was the inferred radius minus one-half centimeter. For larger bubble volumes, this error is small; but for smaller bubble volumes this error is large and is considered conservative.

The two volumes, the change in pool volume and the gas jet volume as a function of time are shown in Figures 5.7, for a pressure of 6 bars (Run 15). This is typical of all runs except for the 10 bar run, which will be discussed later.

In this figure, the initial entrainment when the jet enters the blowdown chute cannot be measured directly since the blowdown chute is not visible to the camera during an experiment. However, when the bubble emerged into the viewing region, the liquid entrainment was found at this point. This constitutes the first data point on this figure. From the point in time where the jet emerges until the end of the experiment, the chute volume was considered part of bubble volume and thus included in the entrainment calculations.

The entrained liquid volumes as a function of time for the 3, 4, 6, and 8 bar pressures, are shown in Figure 5.8. As can be seen from this figure, the amount of liquid entrained increased with initial core pressure. Also, the rate of entrainment or slope of this data increases with pressure. If the assumption of a linear relation between entrained volume and time is made, applying a least-squares fit to the data reveals

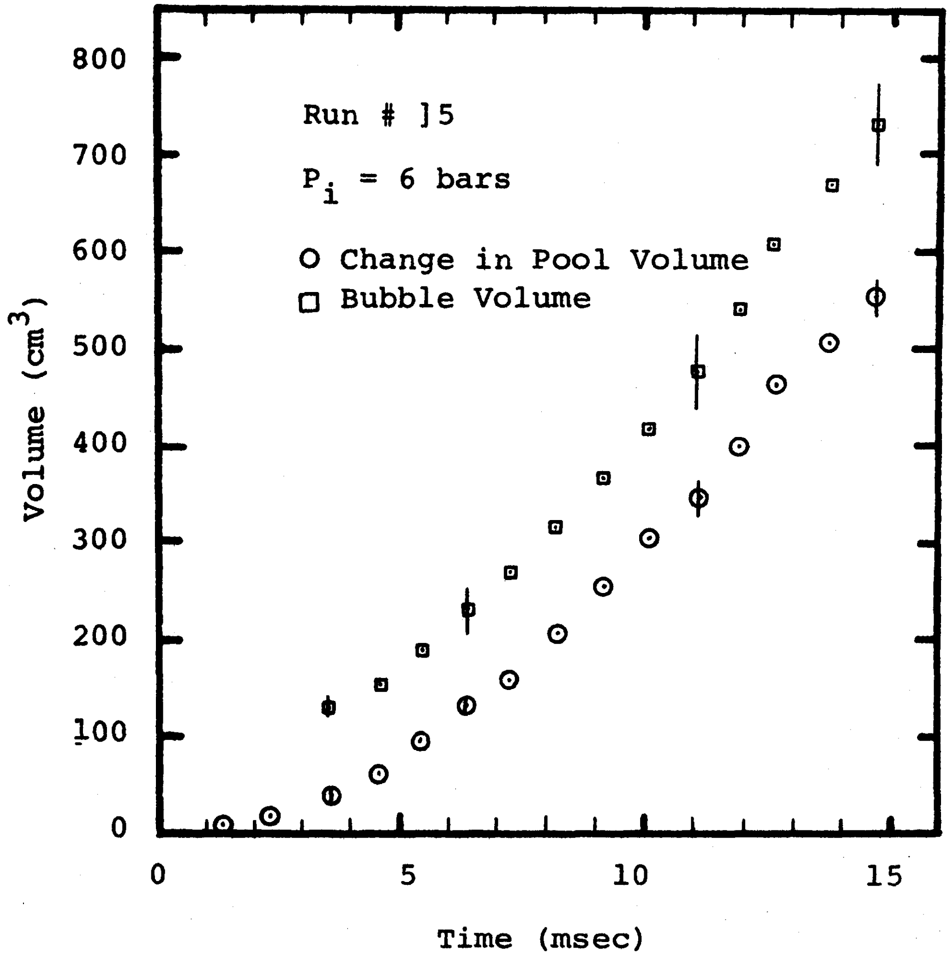

Figure 5.7: Change in pool volume and bubble volume versus time for Run # 15, P_i = 6 bars

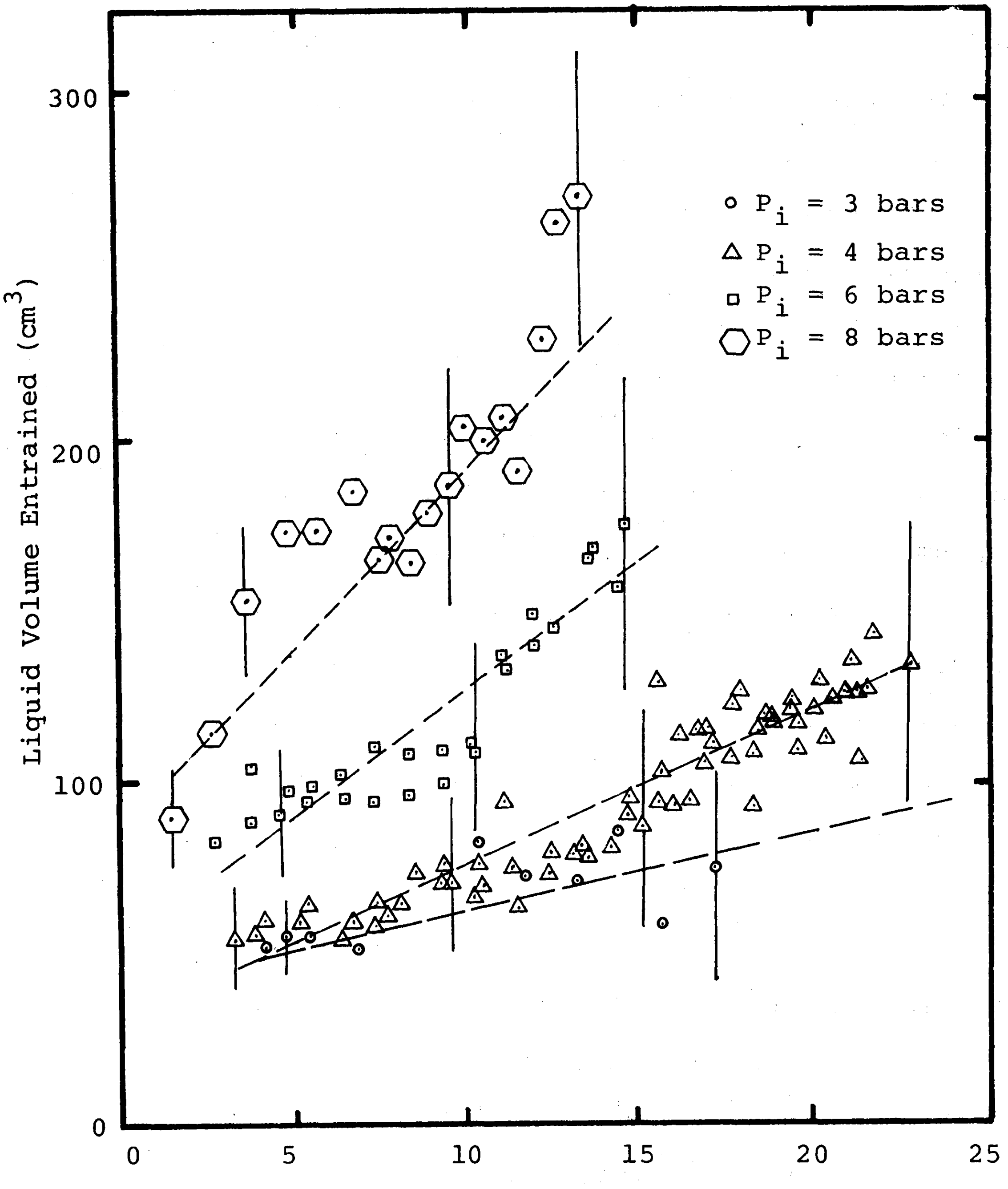

Figure 5.8: Liquid volume entrained versus time for initial core pressures of 3, 4, 6, and 8 bars

rates of 1.3, 4.4, 7.0, and 12.8 cubic centimeters per millisecond for the 3, 4, 6, and 8 bar core pressures, respectively. This is a rough approximation intended only to illustrate the trend.

From this data, the initial entrainment from the chute was seen to increase with pressure. The time when the jet emerged from the chute decreased with increasing core pressure. These results were expected since with higher pressures, jet acceleration will be higher and thus a higher entrainment rate.

The percentage entrainment, defined as the liquid volume entrained divided by the bubble volume and expressed in percent, is shown in Figure 5.9. As clearly seen, the relative entrainment does not vary significantly with pressure. Only the initial entrainment is higher for higher pressures. After approximately 10 milliseconds, nearly all the data from all pressures remain within the ascribed error bounds. However, from the data of Figure 5.9 for the respective pressure and the trend illustrated by Figure 5.7, it is seen that the final bubble volumes increase with pressure, even though the volumetric fraction of the liquid is approximately the same at each pressure. Clearly, the relative entrainment is greatest at the onset of the bubble expansion.

In addition to the above mentioned experiments, two runs (24 and 26) were made at initial core pressures of 10 bars. The pressure histories of these runs behaved quite the same as the lower pressure runs with no abnormalities in the results.

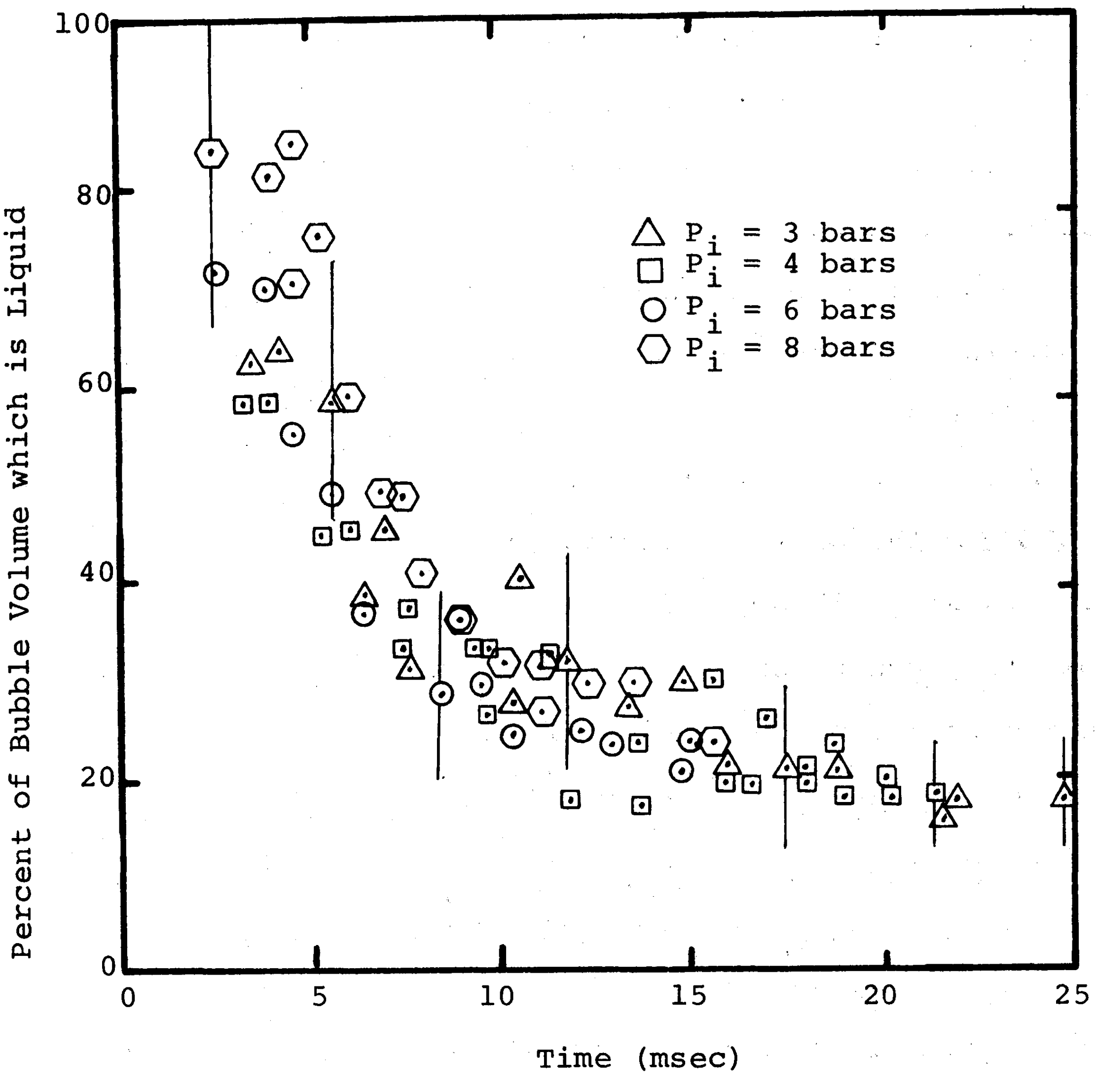

Figure 5.9: Percent of bubble volume containing water for initial core pressures of 3, 4, 6, and 8 bars

However, the entrainment exhibited an anomalous behavior. Liquid volume entrained as a function of time for both runs is shown in Figure 5.10. As can be seen, the entrainment rate became negative at approximately 5 milliseconds and again positive at approximately 10 milliseconds. This trend, in both runs cannot be explained within error bounds of each data set. This trend did not appear in any of the data sets at lower pressures. This behavior could not be explained, and will not be pursued in the present work. However, it is recommended that experiments of higher pressures be performed to determine whether this trend will occur at pressures higher than 10 bars.

A transient entrainment model developed at MIT [13] was applied to the present experiments. A description of the model is given in Appendix F. A detailed development of the model is given by Corradini [13]. Briefly, the overall model assumes isentropic expansion of the core gas, isentropic compression of the cover gas, and two models for the entrainment. One entrainment model for a turbulent jet is similar to Ricou et al. [5] entrainment model and the other is based on the Taylor instability phenomenon.

Calculations using the model were made and the results are shown in Figure 5.11. As Figure 5.11 indicates, the general behavior of the data is agreeable with the model. An initial amount of water is entrained in the chute and then a plateau occurs. This plateau corresponds to the lateral growth of the bubble, thus the entrained volume is constant because of the

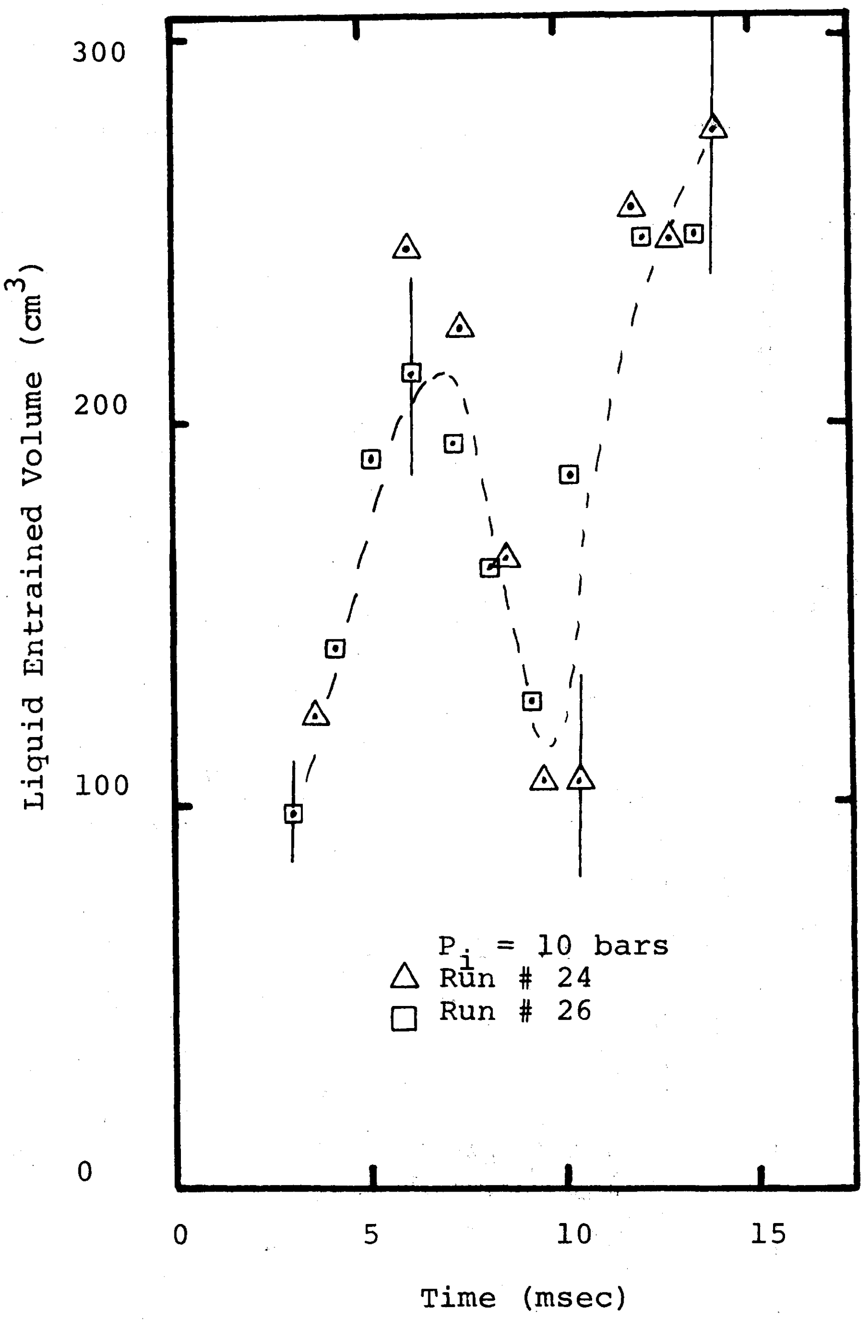

Figure 5.10: Entrained liquid volume versus time for an initial core pressure 10 bars

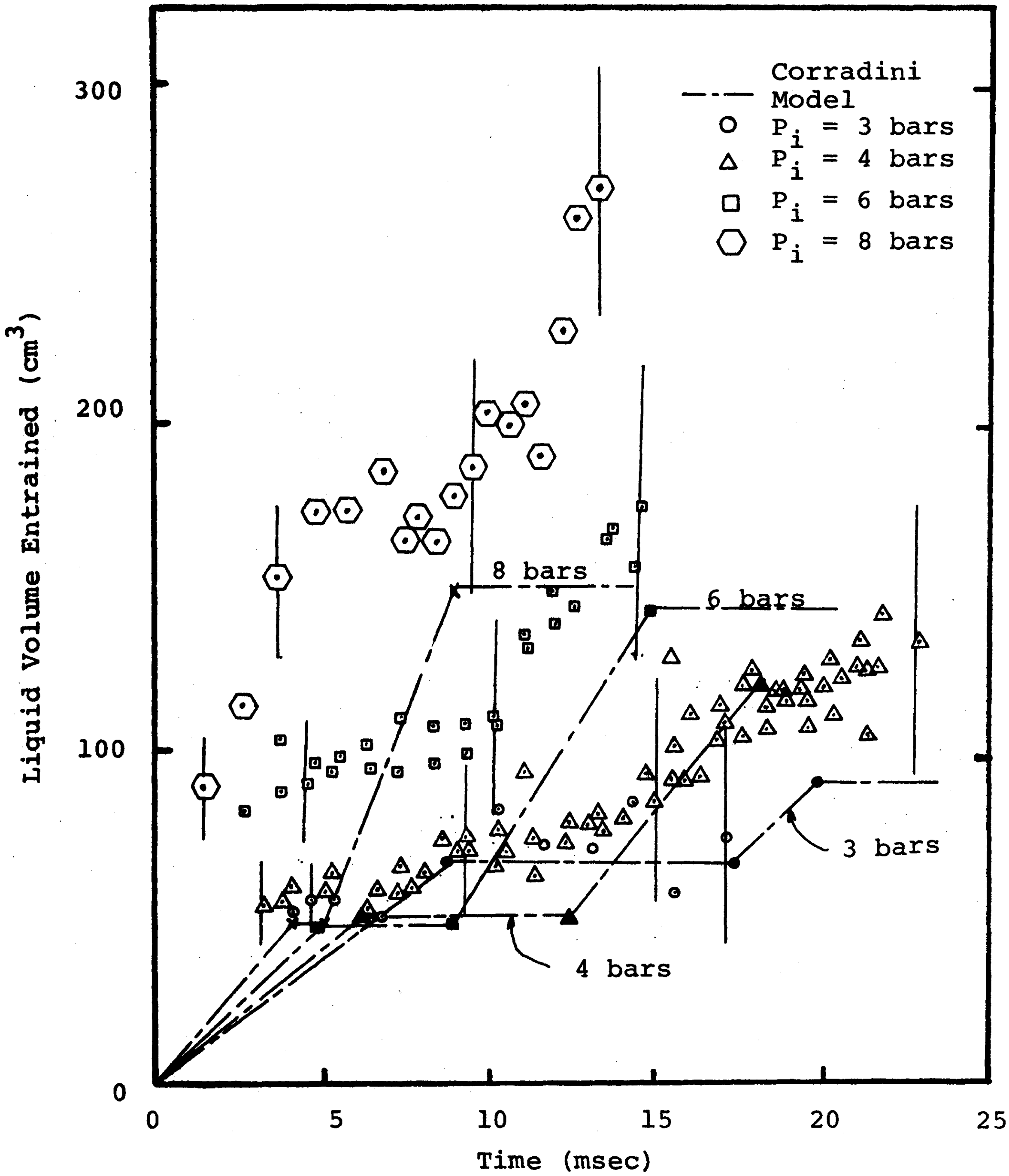

Figure 5.11: Experimental and entrainment model results for liquid volume entrained versus time for initial core pressures of 3, 4, 6, and 8 bars

deceleration of the gas/liquid interface. The model does not include the lateral expansion since it is based on a one-dimensional slug movement. The plateau region is determined from the experimental results by observing bubble growth. Arbitrarily, the pool was assumed to undergo one-dimensional movement upward when the ratio of total gas volume to initial gas volume reached 1.04. The plateau begins when the bubble emerges from the chute. The second plateau is assumed to begin at a volume ratio of 1.09. This is most pronounced for the data at 4, 6, and 8 bars. Once the bubble is close to its maximum width and begins an upward one-dimensional growth in the viewing region, the acceleration turns positive (gas to water) and entrainment due to Taylor instabilities can occur. If measurements were made beyond the point when bubble pressure equaled the cover gas pressure (maximum expansion), another plateau would be expected due to the negative acceleration (water to gas).

Quantitatively, two observations can be made about the agreement between the experimental data and the calculation:

1) The prediction of the water volume entrained during gas expansion in the blowdown chute is below the experimental value and the difference varies from a negligible amount to almost 40 cubic centimeters (low pressures and high pressures, respectively).

2) The water entrained as predicted by the model during the expansion in the viewing region is in good agreement with the experimental data.

This indicates that Taylor instability is the primary mode of entrainment for this expansion.

A possible reason for this disagreement about the chute region entrainment could be that a substantial volume was left on the walls of the chute and is removed during the viewing region expansion. This will also explain the internal jet seen in the photography of the blowdown. Thus, the liquid is not entrained initially (although the data analysis assumed it was entrained when the jet emerged into the viewing region). Further analysis of the chute effects may reveal a new transient entrainment mechanism since this acceleration is relatively quite high during the chute expansion at high pressures.

5.5 Chute Effects on the Blowdown

Two experiments, Runs 25s and 27s, were made to determine the effect of the blowdown chute on development of the jet and the entrainment. This was achieved by placing an aluminum foil barrier at the top of the blowdown chute, at the entrance to the viewing region, thereby eliminating any initial liquid presence in the chute.

In Run 25s, with an initial pressure of 4 bars, an irregular breaking of the aluminum foil occurred, creating two separate bubbles, one forming either side of the chute. However, each bubble had formed a volume of about 11 cubic centimeters when the foil over the chute eventually broke cleanly. At that point, the bubble grew laterally almost to the sides of the viewing region before any significant vertical growth took place. Then the bubble became curved on the leading edge and experienced one-dimensional upward growth. There was essentially no visible entrainment of the liquid during this entire period and the interface was crisp in appearance. Compared to the other 4 bar hydrodynamic runs, the growth was much more lateral initially, expanding approximately to the same volume in a slightly shorter length of time. Analysis of the photography data revealed little entrainment, less than 10% of the expansion volume, of the liquid. The abnormal initial stage of the expansion in this measurement makes it difficult to attach much significance to this result. However, this entrainment result agrees with the results of Christopher [14] for approximately the same pressure of 4.5 bars. Other geometrical parameters were similar to the present work, except for the fact that a three-dimensional pool instead of a two-dimensional pool were used. As was expected, the volume entrained in run 25s was less than that of the other 4 bar runs by 50 to 80 cubic centimeters. This volume accounts for the entrained volume in the blowdown chute.

The faster lateral growth in this run can be attributed to the lesser momentum imparted to the leading edge by the incoming gas than in the other 4 bar hydrodynamic runs with an equal volumetric expansion rate. The mass flow rate of gas into the blowdown chute from the rupture flange volume (other experimental parameters being equal) should be approximately the same for both runs. However, since in the former case water is contained in the chute and clearly is entrained as the gas moves through the chute, one would expect the momentum of this two-phase fluid to be greater than that of the pure gas. As best as can be determined the gas volume, volumetric flow rate, and pressure are approximately the same in the chute when the ject emerges from the chute for both runs, the two phase density is greater than the single phase (gas) density. Thus, with the theory of the vortex ball developed by Abramovitch and modified by Theofaneous [12], the observed diminishing of the upward penetration rate by the single phase fluid jet is explained since the ratio of the jet fluid density to the liquid density is greater for the two phase jet. Figure 5.12 is a graph of the width (D) and the height (L) of the bubble in the viewing region for both types of runs illustrating the relative growth characteristics. As can be seen in this figure, the growth rates of L and D are faster for the "without chute" runs than the normal runs.

The 8 bar run, Run 27s, exhibited growth characteristics similar to run 25s except that entrainment of the liquid at the interface during the transient was clearly seen. There were no irregularities in the break-up of the aluminum foil. The entrainment trend was similar to that of Figure 5.9 with nearly 100% entrainment in the first 2 milliseconds decaying to approximately 25% entrainment near the end of the transient.

Again, as in 25s, the entrained volume was initially lower than the other 8 bar hydrodynamic runs by 40 to 80 cubic

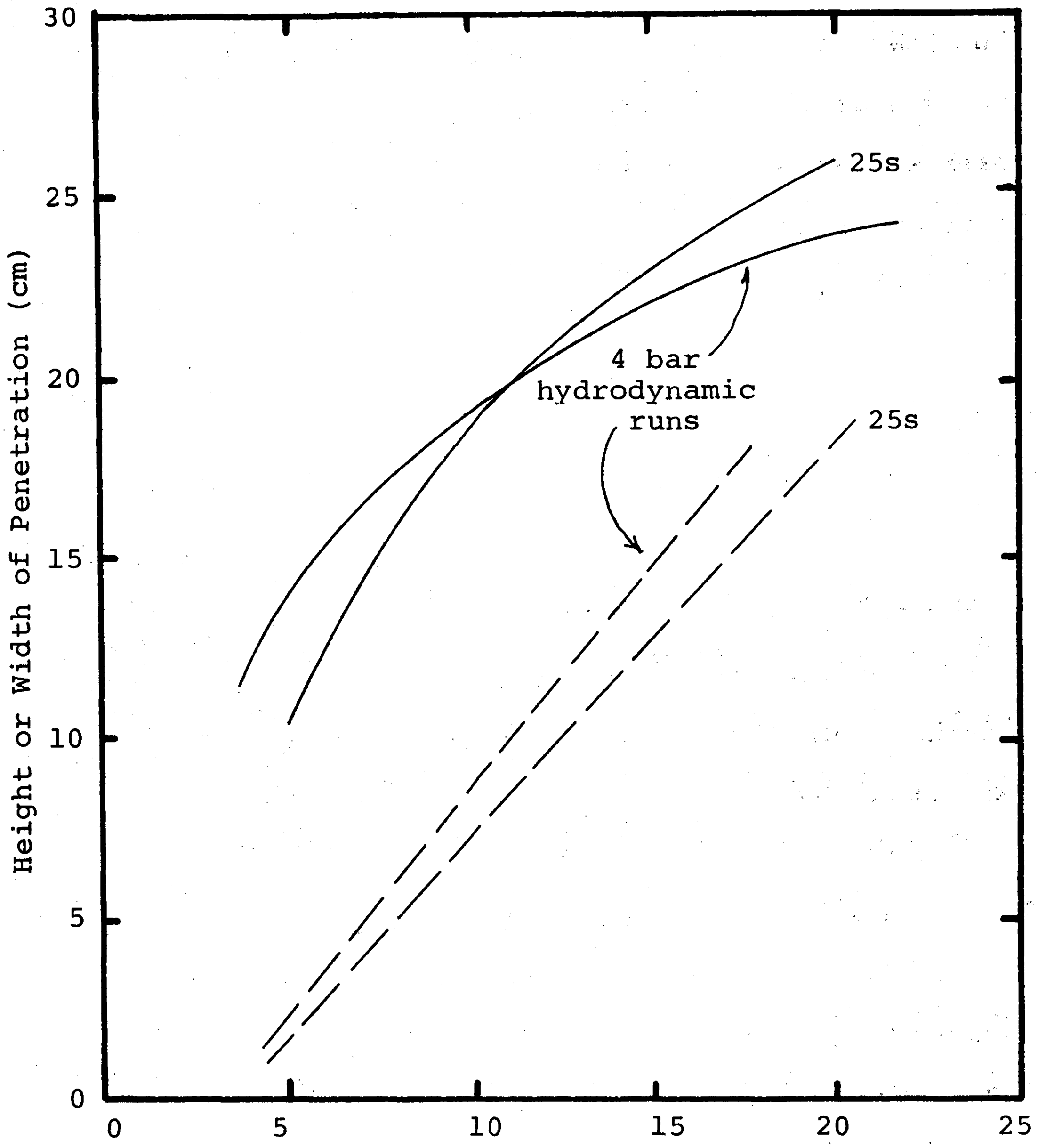

Figure 5.12: Height and width of penetration versus time for an initial core pressure of 4 bars with and without blowdown chute included in the initial liquid volume

centimeters. This volume corresponds to that of the blowdown chute, within the experimental error. The Corradini model predictions of the entrainment for this case are lower than the observed entrainment by about 100 cubic centimeters at the end of the transient. This again suggests that there may be another entrainment mechanism associated with high pressures.

5.6 Growth Characteristics of the Expansion

The growth characteristics are defined by the height (L) and width (D) and the rates of change of these dimensions in the viewing region. Figure 4.1 illustrates these dimensions.

The height of penetration versus time is shown in Figure 5.13. This data is the best least-squares linear fit to the data at each pressure. As clearly seen, the rate of the penetration length increase is greater for higher pressures, which is expected. Also, the maximum height obtained increases with increasing pressure. This figure also gives a better representation of the experimental times of each of the runs. The lines are plotted with the minimum and maximum times for the expansion as the endpoints of the line. The width of the penetration versus time is shown in Figure 5.14. Here a logarithmic least-squares fit was used. As seen in Figure 5.14, the magnitude of the width reaches approximately a constant value, 25 cm (overall width 30.5 cm), in increasingly longer time for

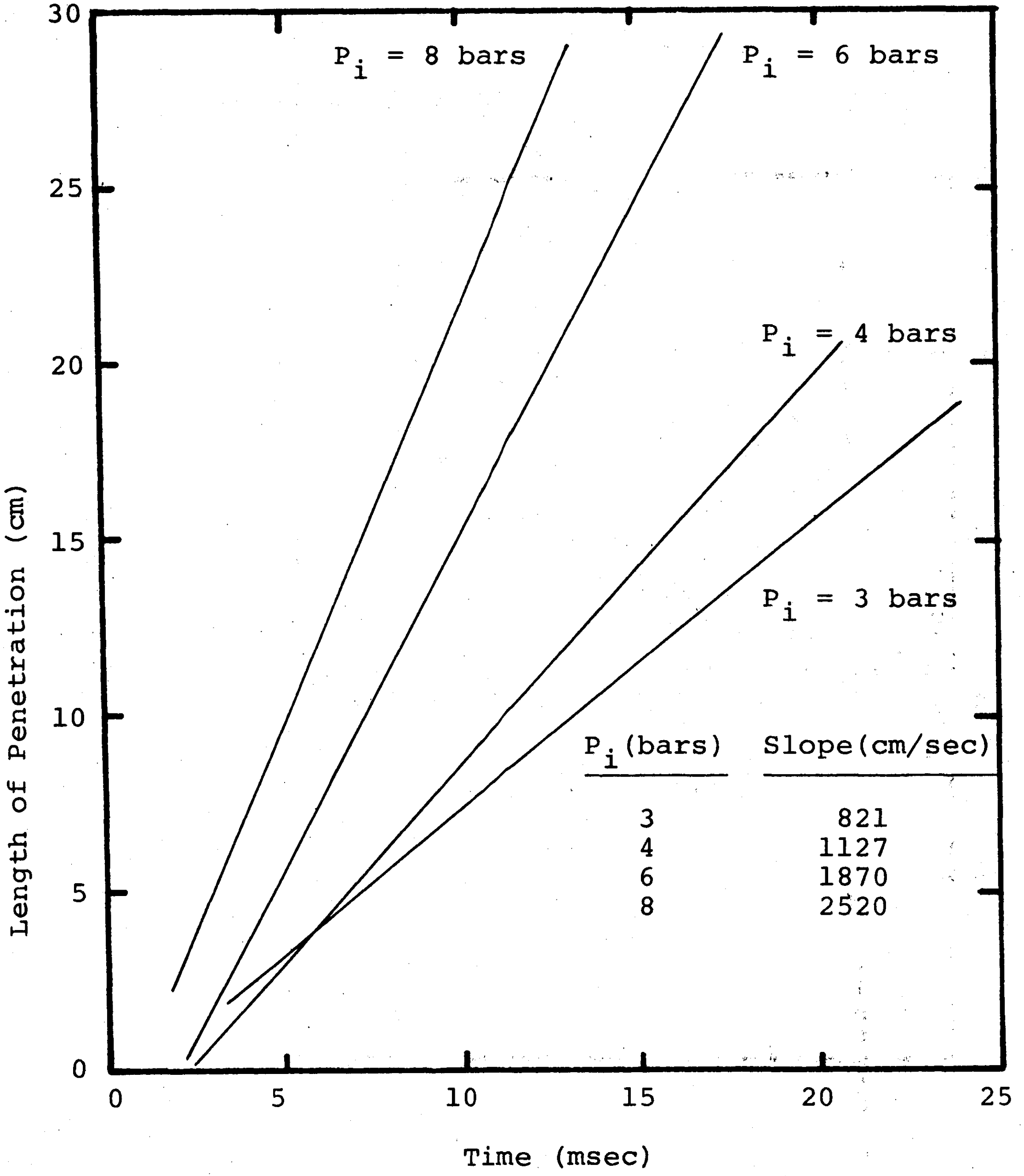

P_i(bars)	Slope(cm/sec)
3	821
4	1127
6	1870
8	2520

Figure 5.13: Length of penetration of discharge versus time for initial core pressures of 3, 4, 6, and 8 bars

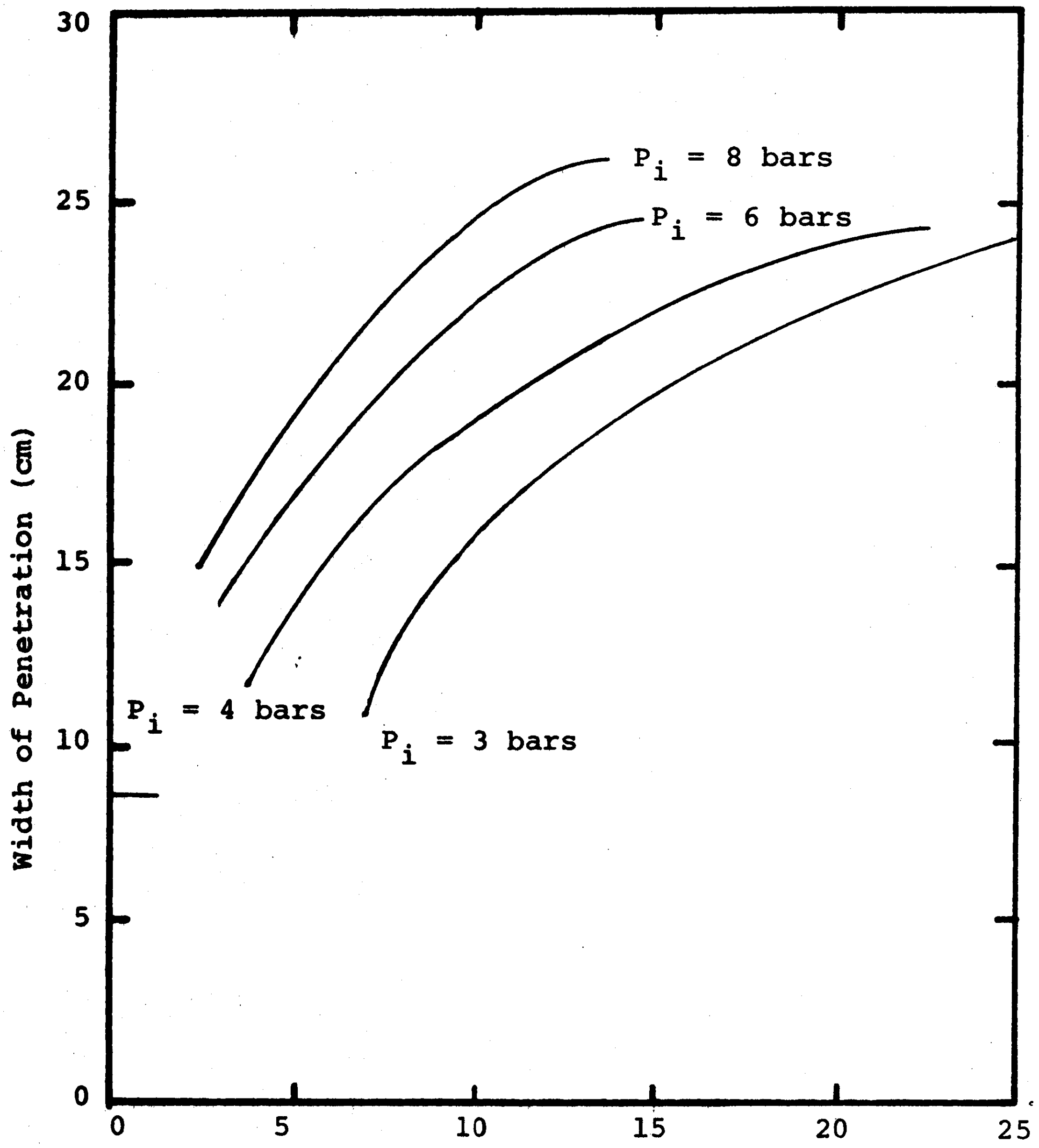

Figure 5.14: Width of penetration of dishcarge versus time for initial core pressures of 3, 4, 6, and 9 bars

decreasing pressures. The data set for any given pressure indicates that the rate of width growth decreases as the bubble width approaches the overall width of the viewing region. Also, the relative rates of growth, indicated by the steepness of the curves, increases with pressure. The initial width a few milliseconds after the bubble emerges is higher for higher pressures.

The curve fits applied to the data sets are not intended to model the phenomenon of width growth or height of penetration. Instead, this method allows a more clear presentation of the data to indicate relative growth rates between the different pressures.

5.7 Relevance to LMFBR Safety Analysis

A model was developed for the assessment of the work potential resulting from a mechanical disassembly of the voided Fast Flux Test Facility (FFTF) core by Cho and Epstein [23]. The model was based on a homogeneous mixture of fuel vapor and liquid ejected into the liquid sodium pool forming a single bubble. They considered two types of entrainment mechanisms. One assumed that the sodium-to-fuel mass ratio was constant; the other was described by an entrainment law for turbulent gas jets (Ricou and Spalding [5]). Also, their model considered work energy effects due to both fuel expansion and potential vaporization of sodium mixed with the ejected fuel. Although many conclusions were drawn from their calculations, the one particularly of interest here is that a certain value of sodium entrainment was found to lead to a maximum work potential. More sodium was seen to quench the expansion and reduce the work potential. This sodium-to-fuel mass ratio was found to be 0.2.

It is of interest to interpret the significance of the present hydrodynamic experiments in light of the Cho-Epstein calculations. The experiments are not exactly representative of the LMFBR geometry. The volume of liquid sodium removed from the pool was calculated by subtracting the Cho-Epstein calculated bubble volumes, at the time of slug-impact, for no entrainment and with entrainment. The value of 0.5 (50% entrained liquid sodium by volume) is concluded if no sodium were vaporized but entrained as a liquid into the developing bubble.

Lenz [24] also made calculations of the work potential at slug impact in the FFTF for fuel temperature of 4000 °K. These calculations were based on an assumed fuel-to-sodium mass ratio at impact.

Figure 5.15 illustrates the resutls of these calculations of work potential at slug-impact for different sodium-to-fuel ratios. Both Cho and Epstein's and Lenz's calculations are shown. The figure also shows the data from the present experiment (Figure 5.9).

From Figure 5.15 it can be seen that Cho and Epstein's calculation for the maximum work potential occurs on the right side of the experimental range, thus indicating that sodium

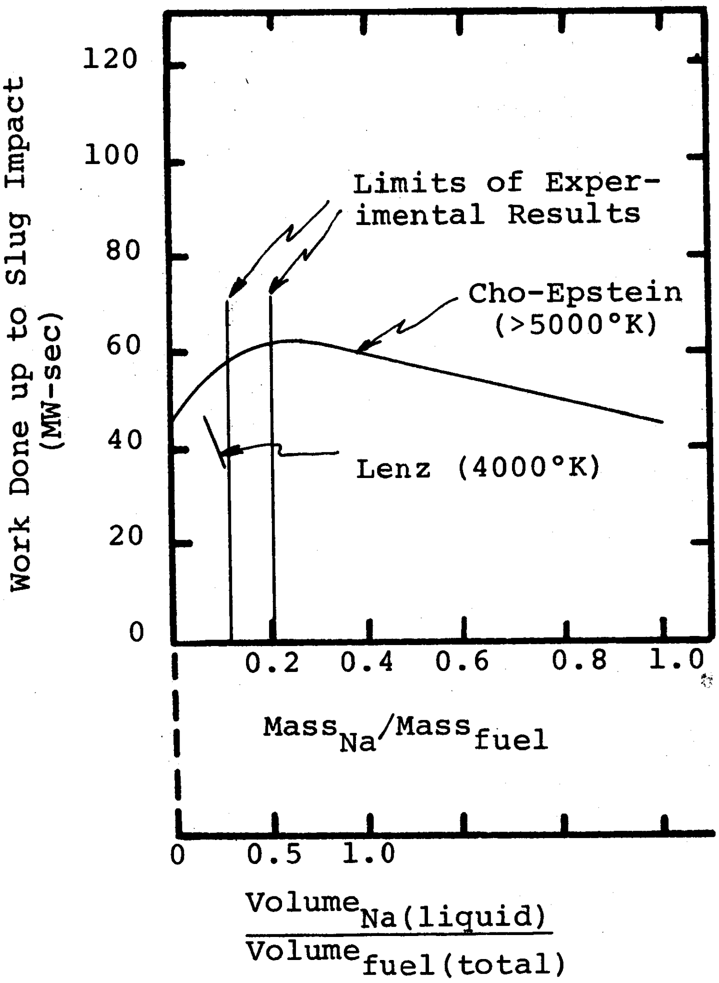

Figure 5.15: Work done until slug impact in a HCDA versus fuel/sodium mass and volume ratios

entrainment in this case will play an important factor in determining the work exerted at slug impact.

While sodium entrainment is seen to increase the work potential above the no entrainment conditions in the Cho-Epstein case, the opposite is true for the case analyzed by Lenz. Thus, it seems important to continue to investigate the mechanisms of entrainment, under the conditions of interest to the LMFBR, in order to get proper assessment of the potential mechanical energy imparted on the vessel under such hypothetical conditions.

VI. THERMAL-HYDRAULIC EXPERIMENTAL RESULTS

6.1 Introduction

The thermal-hydraulic (T-H) experimental results are discussed in the following five sections: 1) a qualitative discussion of the T-H blowdown, 2) a quantitative presentation of the typical pressure histories, 3) a quantitative presentation of the liquid entrainment measurements, 4) the growth characteristics of the bubble in the viewing region, and 5) a discussion of the significance of the results relative to models for assessment of the mechanical work potential following a hypothetical accidental disassembly of a fast reactor core. The experiments undertaken in the present work and the initial experimental conditions are listed in Table 4.1. The heated T-H experiments are called superheated or TH/SH and the non-heated T-H experiments are called subcooled or TH/SC. A set of experiments at subcooled conditions were run to serve as a reference for the superheated experiments.

Since, in the T-H experiments, a heated gas (above the) boiling point of the liquid) was injected into a near saturated liquid, the initial temperature of the gas (air) must be known. The temperature was measured at two locations within the core vessel. The average of the two temperatures was then calculated as the bulk temperature of the gas at injection.

The gas did undergo an isentropic expansion, thus lowering the injection temperature to 91% of its initial value. From experience it was seen that the gas underwent a less than isentropic expansion and thus did not reach the lower limit temperature of 91% the initial value. Experimental conditions limited the degree of superheat to approximately 12 °C above the boiling point of the freon R-113, (boiling point of R-113 is 44 °C at 1 bar pressure). The expansion of the gas jet into the viewing region is such that the bulk pressure of the pool remains near atmospheric for the initial period of the blowdown through scaled slug impact. Since no pressure wave was detected on the plenum pressure history, it was assumed that the superheat condition could cause vaporization. However, it should be noted that if vaporization of the freon occurs, it would occur at the interface of the gas and liquid since the entrained liquid will have a higher boiling point because of the higher pressure within the bubble. The gas above the pool in the viewing region was purely freon R-113 vapor. Since the freon vapor is heavier than air, it would displace the air from this region. This was noted visually during the course of the experiments.

6.2 Qualitative Description of the T-H Blowdown

Experiments were performed at two initial pressures, 4 bars and 6 bars. The initial development of the bubble was different for each of these runs, but basically similar to the hydrodynamic experiments. The 4 bar runs, both subcooled and superheated, developed as two nodes emerging from the chute, symmetric with respect to the centerline and similar to the hydrodynamics runs. The cleavage between the nodes did not disappear with further development but instead grew deep as the bubble developed. The tread effect of the gas/liquid interface was more pronounced than the hydrodynamic runs with some actual visual liquid entrainment of the liquid off the bottom of the viewing region into the bubble. The internal jet, although still present, was not seen as streams of liquid from the edges of the chute like the hydrodynamic runs, but rather as a uniform flow over the width of the chute.

The subcooled and superheated 6 bar experiments developed as two nodes also, but the cleavage disappeared within a few milliseconds of emergence. From that point on, the bubble mushroomed rapidly in the lateral direction with a less pronounced tread effect on the gas/liquid interface.

As with the hydrodynamic runs, the expansion was faster and larger in volume for the 6 bar runs compared to the 4 bar runs. No visual differences were noted between the subcooled or superheated runs for either pressure.

In the T-H experiments, the visual color or shade of the bubble was more uniform gray with less black and white areas, especially in the centers of the nodes. The bubble color was black as the bubble emerged from the chute.

The collapse of the bubble was symmetric on the viewing region centerline. The bubble developed into two swirling bubbles as the center of the upper edge collapsed. This was different than the hydrodynamic runs which completely lost symmetry and form at collapse.

6.3 Typical Pressure Histories

The pressure histories of the T-H runs were similar to the hydrodynamic data for each respective transducer. However, the principal means of determining whether vaporization of the liquid freon occured was the depressurization rate of the core and chute. It is hypothesized that if some of the liquid were to be vaporized, either the depressurization rate of the core would decrease or the volumetric expansion rate of the bubble would increase or both. This would occur because of the additional vapor or gas introduced into the gas volume by vaporization, thus contributing to the overall gas pressure and gas volume. The liquid volume is assumed not to be significantly affected by the losses due to vaporization.

Experimental error of the gas volume measurements is identical to that of the hydrodynamic results, and is assessed at being no more than ± 20%.

The plenum pressure normalized against the initial core pressure as a function of time is shown in Figure 6.1 for 4 and 6 bars, TH/SC and TH/SH runs. Comparing this to Figure 5.3, the plenum pressurization rate is slower. This can be attributed to the freon density being 50% greater than that of water and thus having a higher inertial resistance to an upward motion. The compression was again isentropic in this region.

The blowdown chute pressure normalized against the initial core pressure as a function of time is shown in Figures 6.2 and 6.3 for 4 and 6 bars pressure, respectively. Both TH/SC and

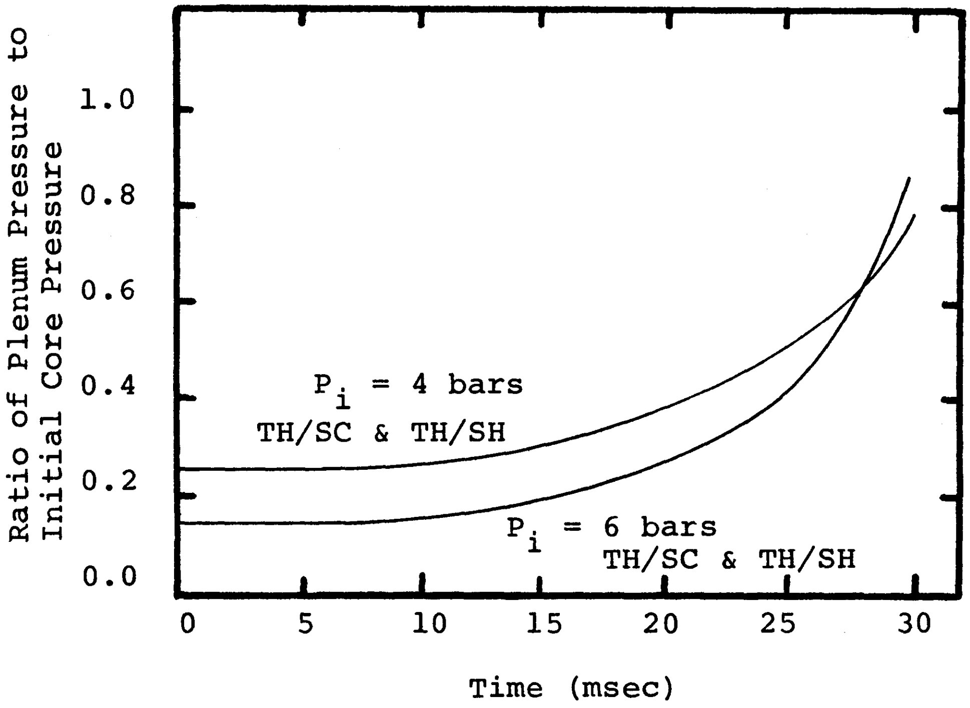

Figure 6.1: Ratio of plenum pressure to initial core pressure versus time for T-H runs at pressures of 4 and 6 bars

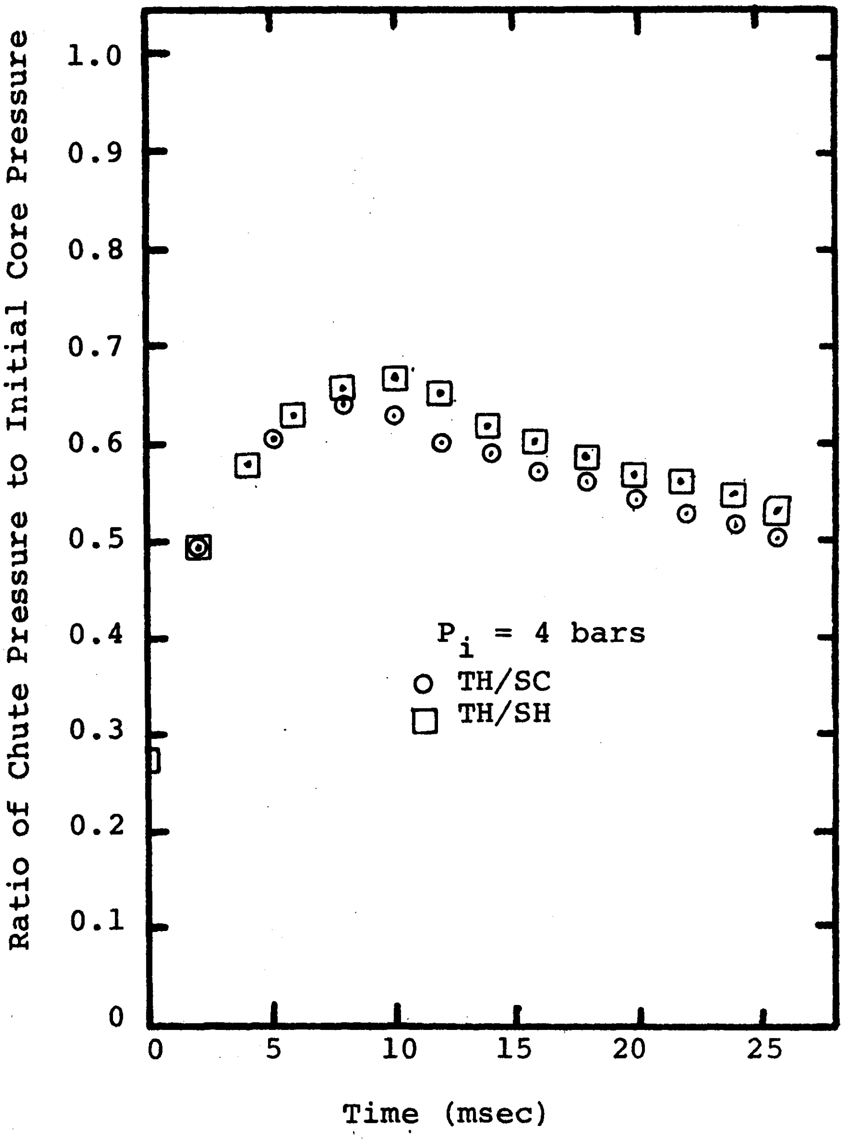

Figure 6.2: Ratio of blowdown chute pressure to initial core pressure versus time to T-H 4 bar runs

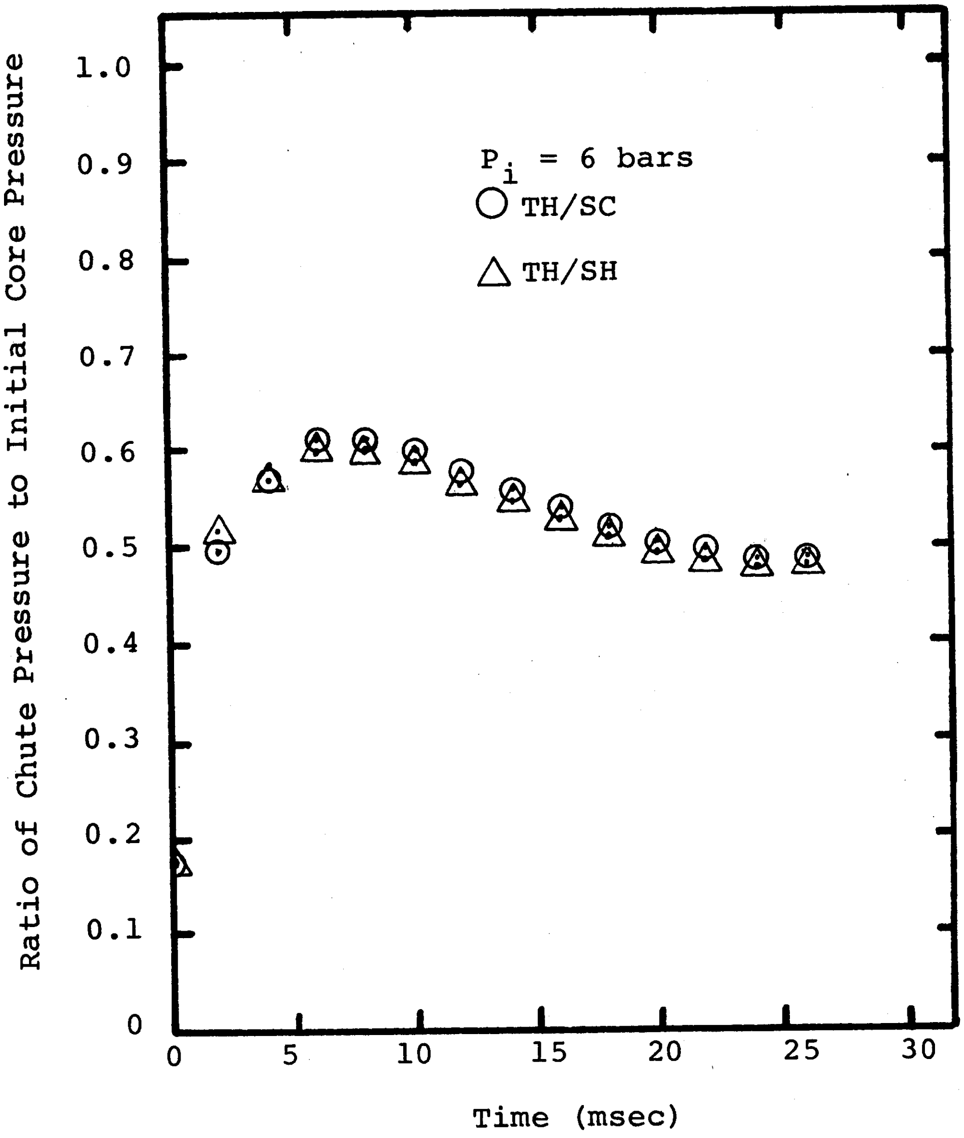

Figure 6.3: Ratio of blowdown chute pressure to initial core pressure versus time for T-H 6 bar runs

TH/SH data are shown on these figures. As shown by this data, within the 10% error of the readings, the data for superheated and subcooled runs were approximately the same. This data, compared to Figure 5.4, illustrates a similar trend with approximately the same magnitude.

A more detailed analysis was made of the core pressure with emphasis on the depressurization rate of the core after the initial pressure change. Figure 6.4 shows as a function of time the core pressures relative to the initial pressure, for 4 bars initial pressure. Similar trends exist for the T-H data as that displayed by the hydrodynamic results of Figure 5.5. However, a noticeable difference in the depressurization rate is found to the right of the line indicated on Figure 6.4. From the least-square linear fit of the data for the 4 bars data, the TH/SC runs depressurized at a greater rate (-4.09×10^{-3} sec^{-1}) than the TH/SH runs (-3.82×10^{-3} sec^{-1}). A similar analysis of the chute data yielded poor fits and thus was not considered valid for such small differences in the rates. Similar analysis was performed on the 6 bar data. The results did not indicate any difference in the depressurization rate from the subcooled runs.

An analysis to test for choked flow in the blowdown chute showed that the flow was not choked during any of the T-H blowdowns.

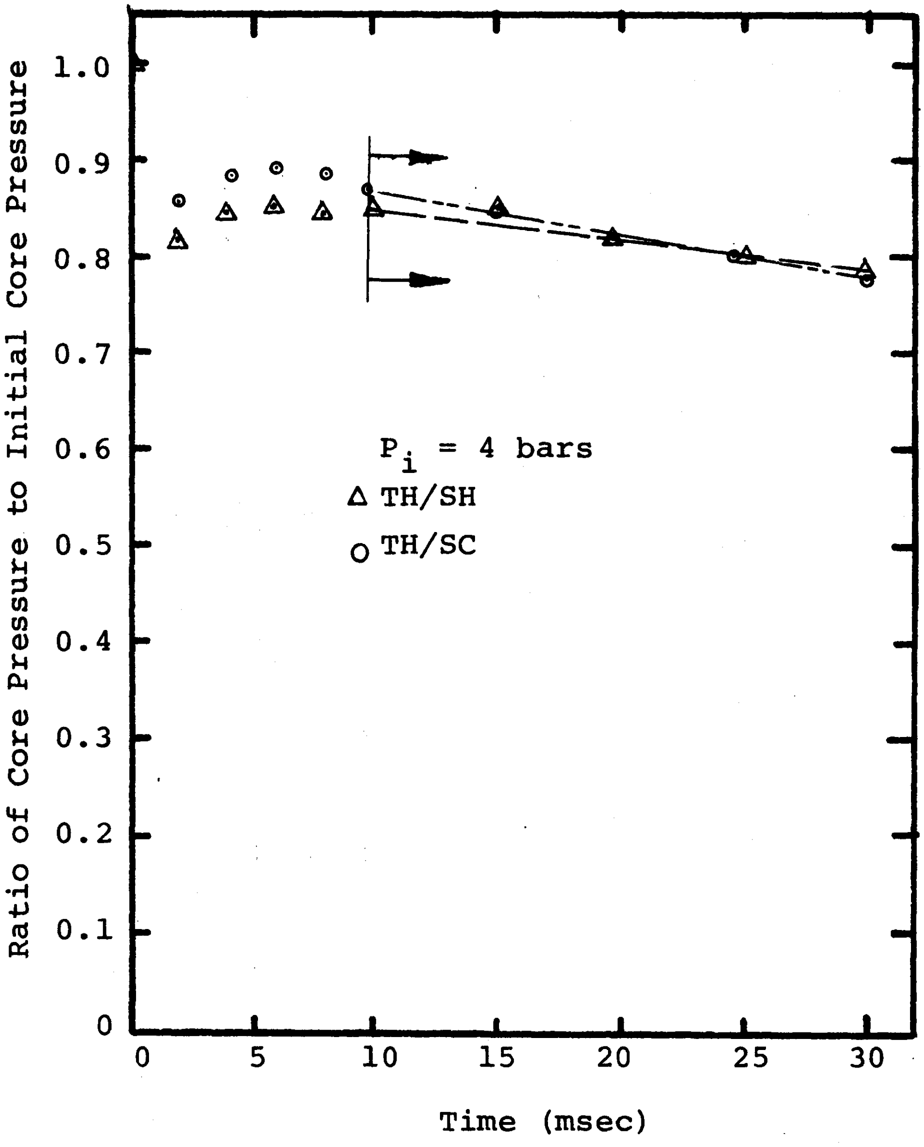

Figure 6.4: Ratio of core pressure to initial core pressure versus time for initial core pressure of 4 bars T-H runs

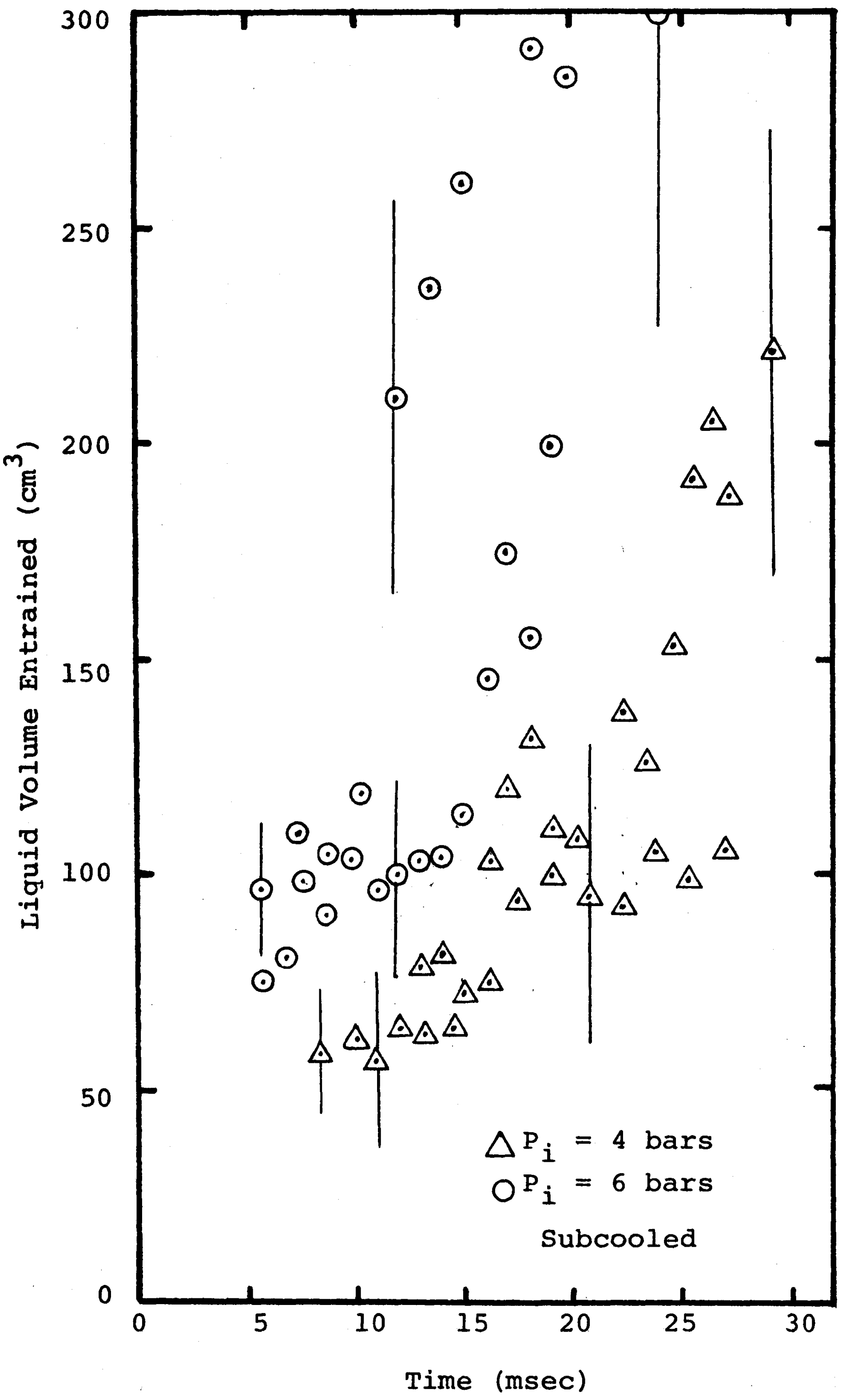

Figure 6.5: Liquid volume entrained versus time for T-H runs under subcooled conditions

6.4 Entrainment Results

Liquid entrainment by the gas as it enters the viewing region was determined by visual observation of the high speed movie films of the experiments. Techniques and definitions similar to those of section 5.4 are used here.

Volume of liquid entrained for the subcooled runs at 4 and 6 bars pressure are shown in Figure 6.5. Linear least-squares fits were performed on the data by pressure group. The 6 bar runs had an entrainment rate of 8.68 cubic centi meters per millisecond while the 4 bar runs had an entrainment rate of 3.79 cubic centimeters per millisecond. This data behaved as the hydrodynamic data did. A similar graph of the superheated data is shown in Figure 6.6. Entrainment rates of 5.90 and 9.52 cubic centimeters per millisecond were calculated from least square linear fits for 4 and 6 bars data, respectively. Thus, for the superheated experiments, a somewhat larger entrainment rate is found. The comparison of the subcooled and superheated data for 4 and 6 bars initial pressure is shown in Figures 6.7 and 6.8, respectively.

In Figure 6.9, the percent volume of the bubble which is liquid is shown as a function of time for all the T-H data and the hydrodynamic data. As seen in this figure, initially, a higher entrainment seemed to have occured for the T-H runs. However, in time, the percent of the bubble volume which was liquid reached a level of approximately 20% as did the hydrodynamic data also.

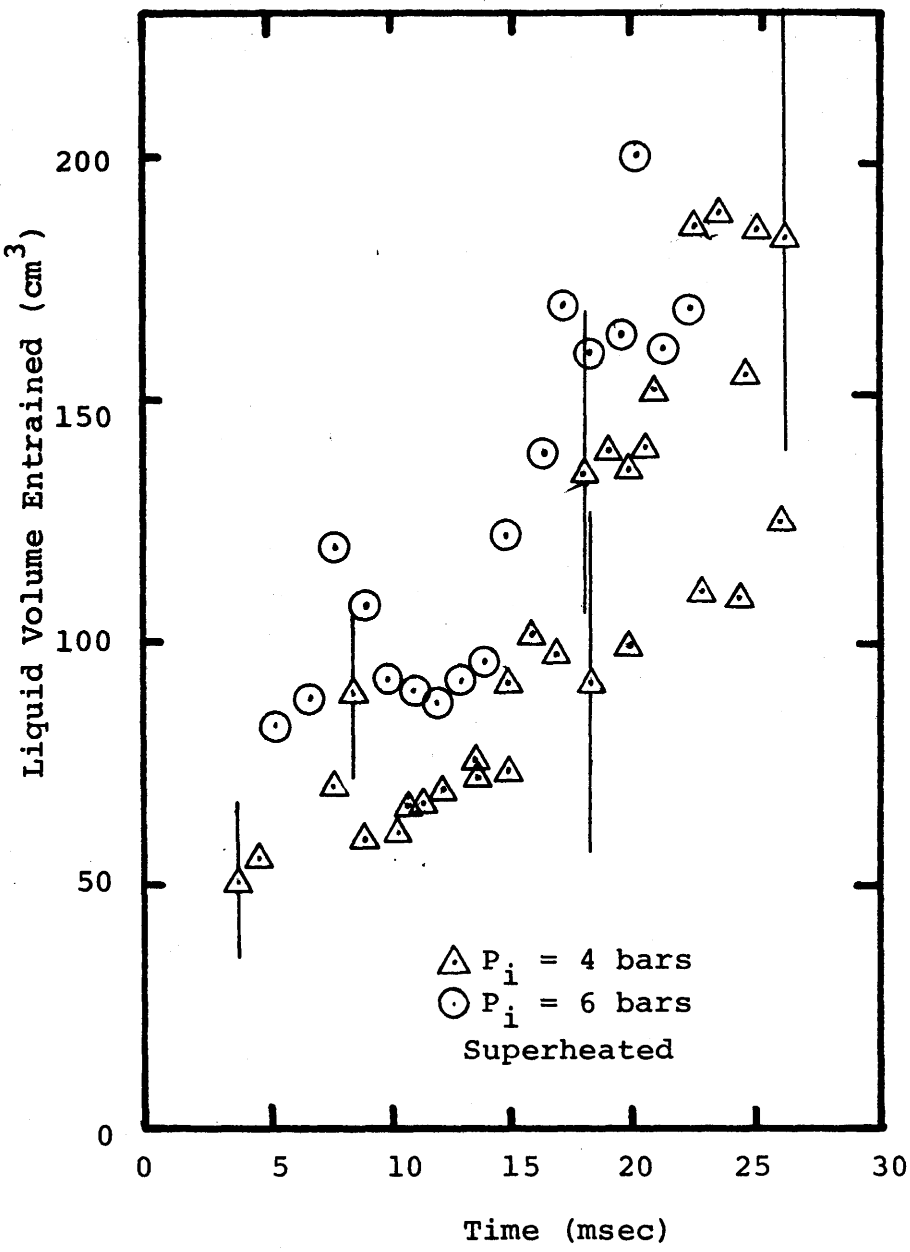

Figure 6.6: Liquid volume entrained versus time for T-H runs under superheated conditions

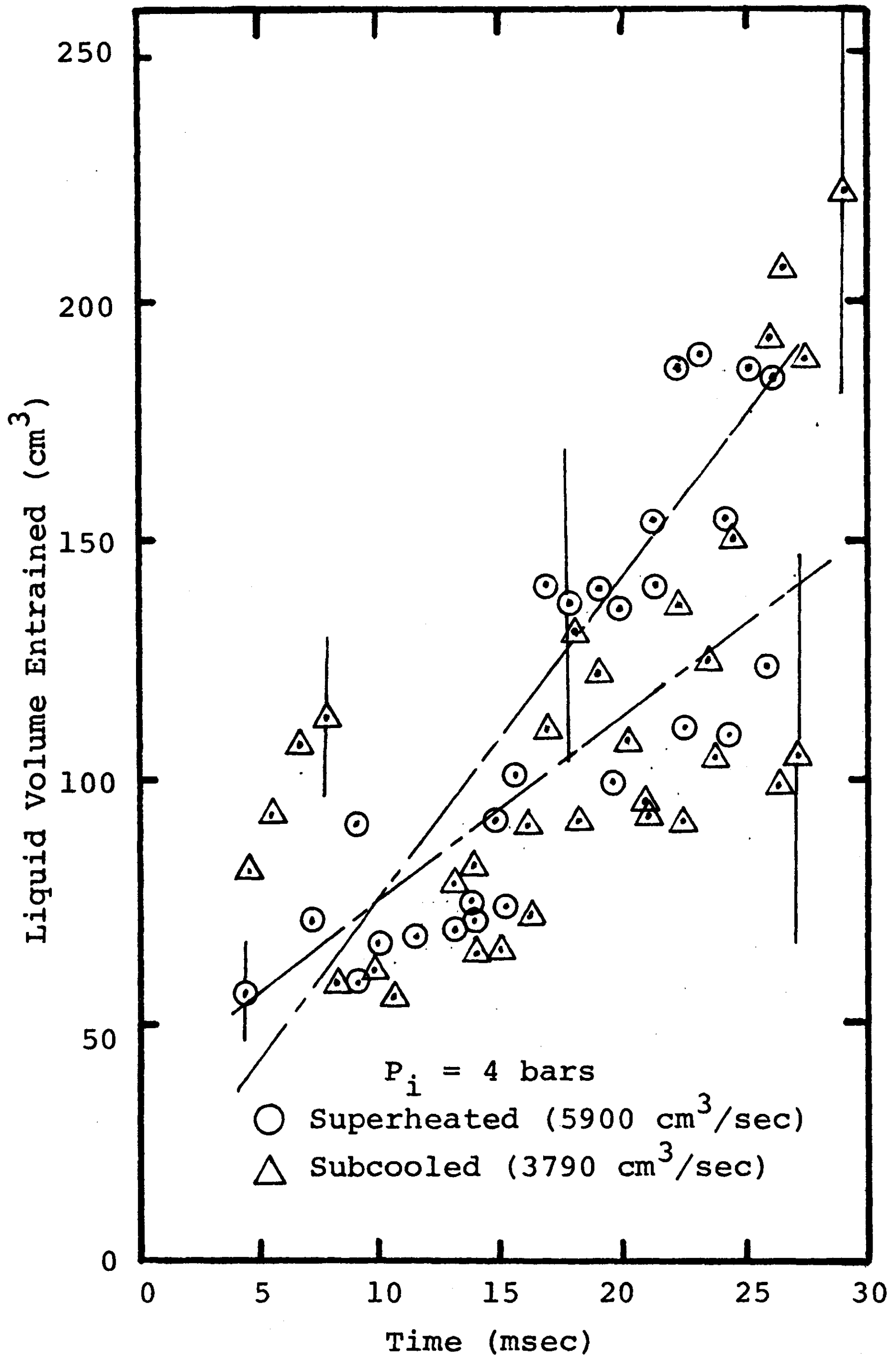

Figure 6.7: Liquid volume entrained versus time for T-H 4 bar runs

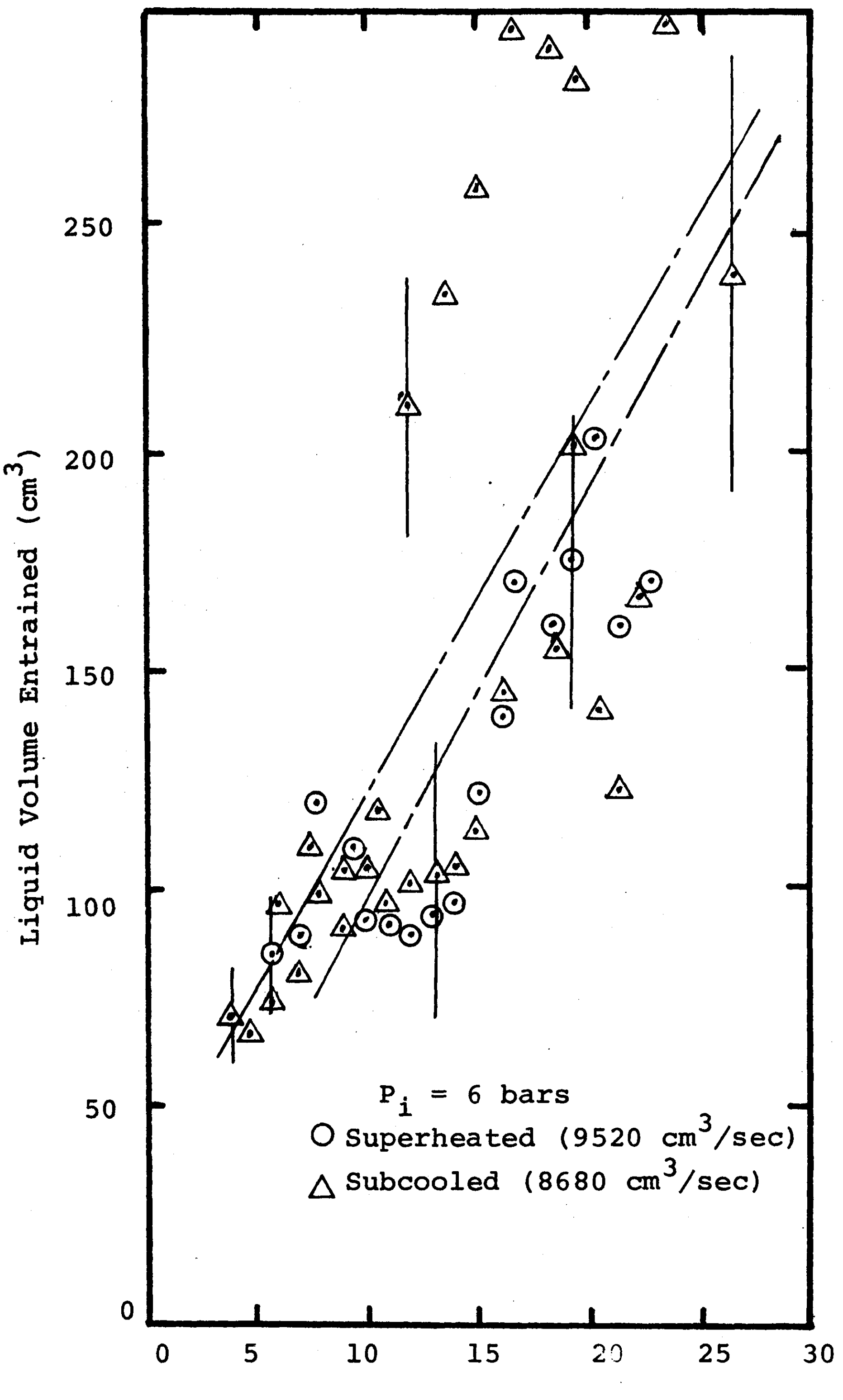

Figure 6.8: Liquid volume entrained versus time for T-H 6 bar runs

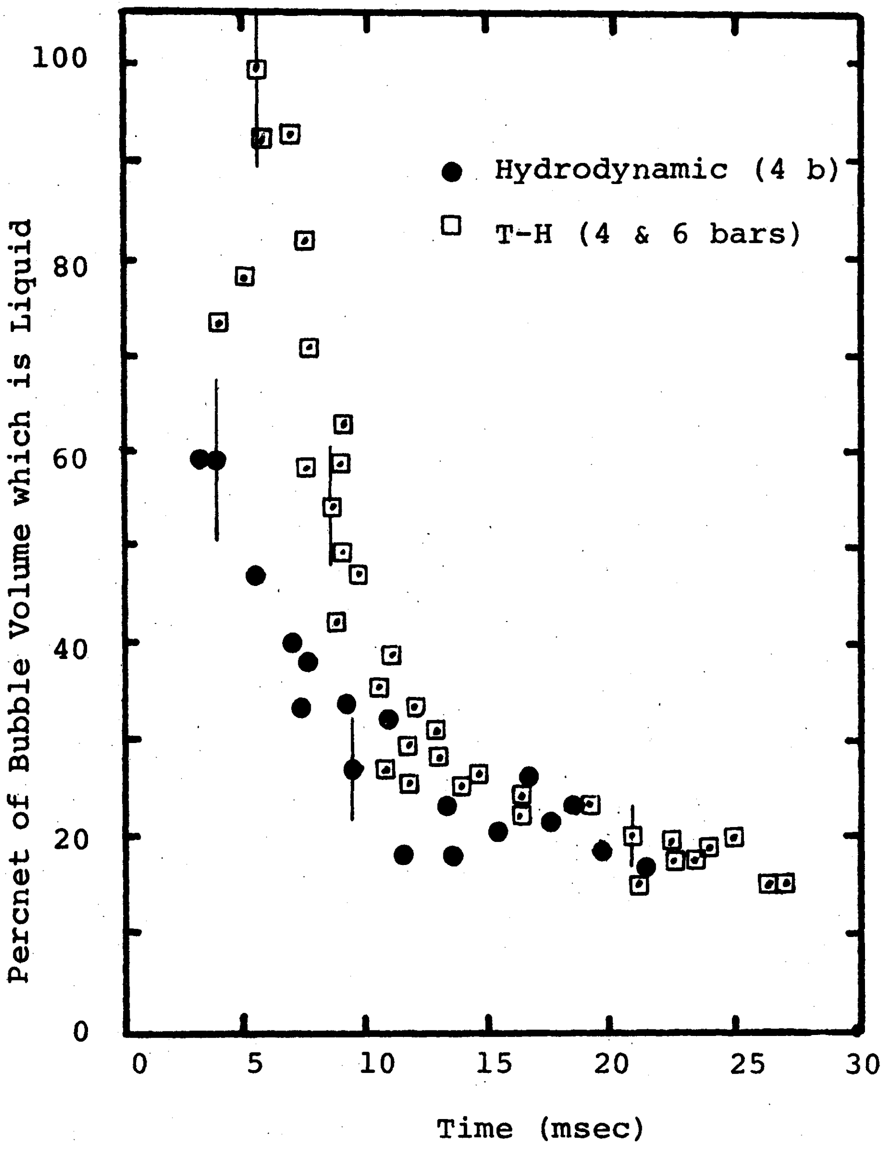

Figure 6.9: Percent of bubble volume which is liquid versus time for 4 bar hydrodynamic and T-H runs

As mentioned in Section 6.3, it was hypothesized that, if vaporization occurred, either the depressurization rate of the core would decrease or the volumetric expansion rate of the bubble would increase or both. Figure 6.10 is a graph of the best fit linear least squares fit data of the volumetric expansion of the bubble in time. Because the fits were excellent, the TH/SH data indicates a higher expansion rate than the TH/SC data for both pressures. Thus, in the case of the 4 bar runs, some vaporization of the liquid freon may have occurred. For the 6 bars data, since the depressurization rate of the core was approximately the same for the TH/SC and TH/SH runs, the higher expansion rate would seem to indicate vaporization. A strong case cannot be made for vaporization because of the limited data available for verification. In both pressure cases, the data was not overwhelmingly distinctive, especially in the case of 6 bars pressure.

6.5 Growth Characteristics of the Expansion

The growth characteristics of the bubble are defined by the penetration height (L) and the width (D) and the rates of change of these dimensions in the viewing region. Figure 4.1 illustrates these dimensions.

The height of the bubble versus time is shown in Figure 6.11 for the T-H and hydrodynamic runs at initial pressures of 4 and 6 bars. There was no significant difference in the growth rates between the TH/SH and TH/SC data of the 4 bar runs. Also, these data were approximately parallel to the hydrodynamic

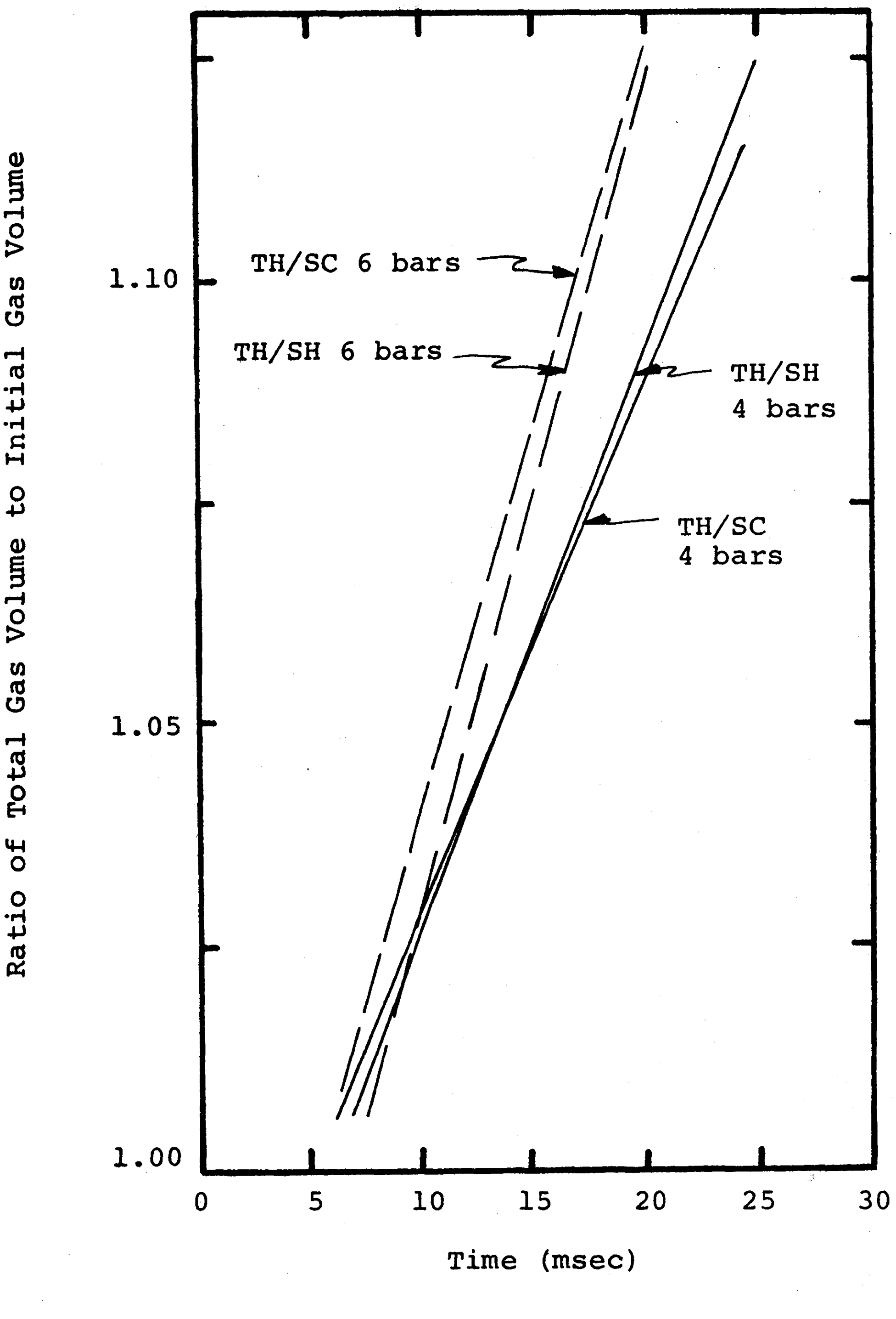

Figure 6.10: Ratio of total gas volume to initial gas volume for T-H runs

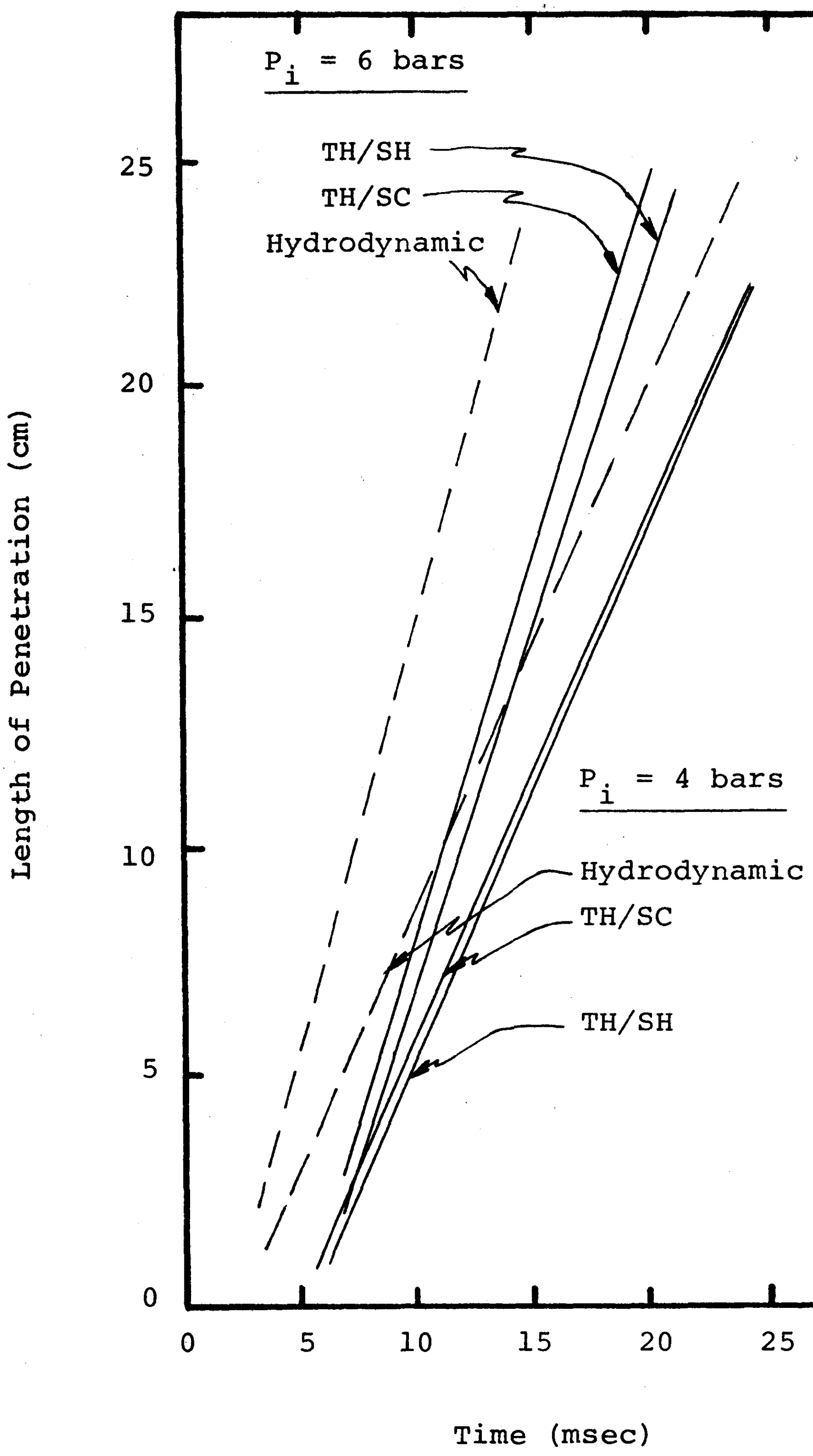

Figure 6.11: Length of penetration versus time for T-H runs

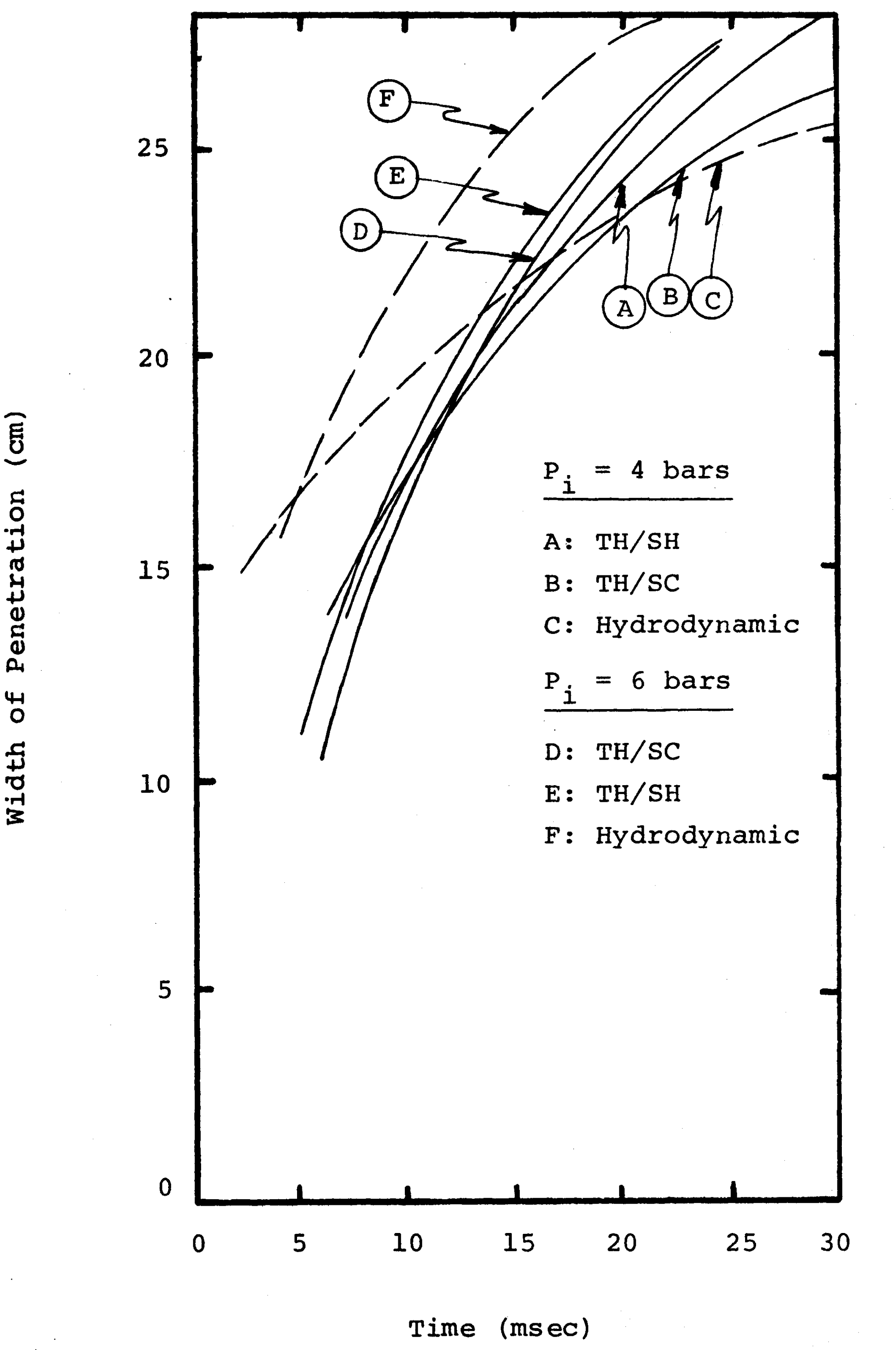

Figure 6.12: Width of penetration versus time for T-H runs

data. The 6 bar runs data yielded results which show a significant decrease in height growth rate for the T-H data.

The width of the bubble versus time for the T-H and hydrodynamic runs for 4 and 6 bars initial pressure is shown in Figure 6.12. The 4 bar data shows a significant increase in lateral growth rate. Recall that there was a pronounced tread effect during these runs causing rapid lateral growth. The 6 bar data indicates only a slight increase in lateral growth rate. In comparison of the T-H and hydrodynamic results, the maximum heights are obtained faster in the hydrodynamic runs. However, at the lower pressure the lateral growth rate is faster for the T-H runs while the opposite is true for the higher pressure.

The data displayed in Figures 6.11 and 6.12 are least-squares fits of the actual measurements. A logarithmic fit was applied to the width data and a linear fit applied to the height data. These fits are used only to present the data as clearly as possible.

6.6 Relevance to LMFBR Safety Analysis

A similar analysis was performed on the thermal-hydraulic data as that of Section 5.7 and compared to the two models [23] [24] presented for work potential at slug impact during a mechanical core disassembly. From the T-H data of Figure 6.9, for scaled impact of the mass slug, 30 to 40% of the bubble volume is liquid. Again, it is of interest to interpret the present T-H data in light of Cho and Epstein calculations although these experiments are not exactly representative of the LMFBR geometry.

Referring to Figure 5.15 which illustrates the results of the calculations of work potential at slug impact for different sodium-to-fuel ratios, similar conclusions can be drawn concerning the work potential since only a smaller band exist in approximately the same location as is on Figure 5.15.

VII. MAJOR CONCLUSIONS AND RECOMMENDATIONS

7.1 Introduction

The present experiments, hydrodynamic and thermal-hydraulic, investigated liquid entrainment, jet development, and the possibility of liquid vaporization by a noncondensible gas. The experiments were similar in all respects except initial pressure conditions and fluid types (Table 4.1). The results of these experiments were used to evaluate the importance of liquid entrainment when the bubble expands in the upper plenum during a hypothetical accident in the LMFBR. Although the apparatus is not a true representation of the geometry in the LMFBR, a closer examination of the phenomena involved is facilitated with its two-dimensional design.

7.2 Entrainment and Growth Characteristics

Liquid entrainment during jet expansion in the plenum was seen to increase with increasing pressure. However, the fraction of the expansion volume which is liquid starts high and decreases to approximately 25% at the end of the expansion. Higher initial entrainment was seen for a more dense fluid. A Taylor instability mechanism for entrainment seems to underpredict the rate of entrainment. Another entrainment mechanism besides that of Taylor instabilities may exist at higher pressures. For the same liquid, heated experiments yielded a slightly higher entrainment rate than the unheated experiments.

Lateral and vertical growth rates were seen to increase with increasing pressure. The growth type trend, bubble or jet, predicted by the modified Abramovich model [12] (i.e. the dependence of the trend on the ratio of the fluids) agrees with the present experimental observations.

7.3 Potential for Vaporization

The potential for vaporization of the liquid by the hot gas in the heated experiments was investigated by the injection of a hot gas into a near saturated liquid. The data indicates vaporization may have occurred for initial core pressures of 4 bars with an initial bulk gas temperature 12 °C above the liuqid freon boiling point. For similar temperature conditions but at a core pressure of 6 bars, vaporization of the liquid could not be determined for lack of data.

7.4 Relevance to LMFBR Safety

A comparison of the results of two models used to assess the work potential during a hypothetical LMFBR accident was made to evaluate the significance of the present experimental results. Based on the present results, sodium entrainment would increase the work potential for the case of high fuel temperature (> 5000 °K) but reduce the work potential in the low fuel temperature case (4000 °K). Further investigation of the entrainment mechanisms under the LMFBR conditions would assist in the development of models for hypothetical accident consequence assessment in a LMFBR.

7.5 Recommendations for Future Work

Further investigation of the geometry effects such as chute width, pool width, and initial pool height on entrainment and bubble development should be pursued. A repeat of the thermal-hydraulic runs at higher temperatures as well as perhaps, further verification of the present work is desirable. It is necessary to obtain a more evenly distributed temperature of the gas in order to obtain more reliable initial temperature measurements. For more typical LMFBR conditions, experiments using condensible vapors at temperatures above the liquid's boiling point should be made, thus combining the effects of condensation and vaporization in the blowdown.

As for the experimental setup, the initiation mechanism for the blowdown is suitable. A first priority is to assemble a more reliable synchronization mechanism to determine more accurately the timing of the data acquisition systems. Accuracy of the photography data can be improved with more lighting evenly distributed on the back window of the apparatus using a diffuser or ground glass. Further experimentation can be improved significantly with these modifications.

REFERENCES

[1] Smith, L. L., Boudreau, J. E., Bell, C. R., and Bleiweis, P. B.; "SIMMER-I, An LMFBR Disrupted Core Analysis Code," Presented at the Fast Reactor Safety and Related Physics Conference, Chicago, Ill., CONF761001, 1976.

[2] Preliminary Safety Analysis Report Clinch River Breeder Reactor, Project Management Corp., Vol. 10, App. D., 1975.

[3] Massachusetts Institute of Technology Fast Reactor Safety Course Notes, Cambridge, Mass., May 1977.

[4] Schlichting, H., Boundary Layer Theory, McGraw-Hill pub., 6th edition, 1968.

[5] Ricou, F. P. and Spalding, D. B., "Measurements of Entrainment by Axisymmetrical Turbulent Jets," Jounral of Fluid Mechanics, Vol. 11, 1961.

[6] Kerney, P. J., Faeth, G. M., and Olson, D. R.; "Penetration Characteristics of a Submerged Steam Jet," AIChE Journal, Vol. 18, No. 3, May 1972.

[7] Tsai, S. S. and Kazimi, M. S., "The Potential for Penetration of a Hot Vapor Jet into a Subcooled Liquid," ASME Journal, 76-WA/HT-78, 1976.

[8] Abramovich, S. and Solan, A., "The initial Development of a Submerged Laminar Round Jet," Journal of Fluid Mechanics, Vol. 59, 1973.

[9] Chawla, T. C., "Rate of Liquid Entrainment at the Gas-Liquid Interface of a Liquid Submerged Sonic Gas Jet," Nuclear Science and Engineering, 56, 1-6, 1975.

[10] Tong, L. S., Boiling Heat Transfer and Two-Phase Flow," John Wiley & Sons, Inc., pub., 1966.

[11] Bell, R., Boyce, B. E., and Collier, J. G., J. British Nuclear Energy Society, 11, p. 183, 1972.

[12] Theofanous, T. G., Grolmes, M. A., Lambert, G. A., and Epstein, M.; "Transient Development of Two-Phase Jets: LMFBR/HCDA Energy Yield and Core Material Transport," Presented at the Fifteenth National Heat Transfer Conference, San Francisco, CA, 1975.

References (continued)

[13] Corradini, M., "Heat Transfer and Fluid Flow Aspects of Fuel Coolant Interactions," Ph.D. Thesis, M.I.T., (to be published), COO-2781-15TR, 1978.

[14] Christopher, D. M., "Transient Development of a Two Phase Jet," Master's Thesis, Purdue University, May 1977.

[15] Ploeger, D. and Cagliostro, D. J.; "Development and Characterization of a Liquid-Vapor Bubble Source for Modeling HCDA Bubbles," Stanford Research Institute, Menlo Park, CA, Technical Report No. 2, March 1977.

[16] Ploeger, D. and Cagliostro, D. J., "Experimental Model Studies of Bubbles Generated in Fast Breeder Reactors During a Hypothetical Core Disruptive Accident," Stanford Research Institute, Menlo Park, CA, Quarterly Progress Report No. 4, March 31, 1976.

[17] Cagliostro, D. J. and Florence, A. L.; "Characterization of an Energy Source for Modeling Hypothetical Core Disruptive Accidents in Nuclear Reactors," Stanford Research Institute, Menlo Park, CA, First Interim Report, October 1972.

[18] Florence, A. L. and Abrahamson, G. R., "Simulation of a Hypothetical Core Disruptive Accident in a Fast Flux Test Facility," Stanford Research Institute, Menlo Park, CA, HEDL-SR1-1 UC-79p, May 1973.

[19] Quinn, D., Personal Communication, Massachusetts Institute of Technology, Cambridge, MA, May 1978.

[20] Fike Metal Products, Personal Communication with Ed Tosh, Quality Assurance Supervisor, Blue Springs, MO, April 1978.

[21] Reactor Saqety Study: An Assessment of Accident Risks in U.S. Commerical Nuclear Power Plants, Appendix III, Failure Data, WASH 1400, (NUREG 75/014) 1975.

[22] Florence, Alexander, Stanford Research Institute, Menlo Park, CA, Personal Communication, July 1978.

[23] Cho, D. H. and Epstein, M., "Work Potential Resulting from a Mechanical Disassembly of the Voided FFTF Core," Argonne National Laboratory, Reactor Analysis and Safety Division, Argonne, Ill, ANL/RAS 75-17, August 1974.

References (continued)

[24] Lenz, William F., Jr., "Mixing Requirements for the Limiting Fuel-Coolant Interaction in Liquid Metal Fast Breeder Reactors," COO-2781-8 TR, Dept. of Nuclear Engineering, Massachusetts Institute of Technology, Cambridge, Mass., November, 1976.

APPENDIX A

ANALYSIS OF RUPTURE DISK METHOD FOR EXPERIMENT INITIATION

An independent study was made of the rupture disk method for experiment initiation in order to determine the time required for opening of the disks. Pleoger et al. [15] have also made a brief analysis of this problem and the sliding door technique. Pleoger's results based on a 3000 psi test of nitrogen below an 11.8 inch head of water with the diaphram separating the fluids, reveal an opening time of approximately 2 milliseconds. Recent testing by Stanford Research Institute [22] has shown with gas in the above, center, and lower regions of a double diaphram system with 2000 psi pressures that time intervals for disk opening are on the order of 1 to 2 milliseconds. Also, one disk systems with liquid on top and pressures of 1500 psi opened in less than 1 millisecond. Although these pressures are two orders of magnitude larger than the present experiments, so also are the diaphram thicknesses.

In the present experiments, the entire 6 inch opening is not required to be 100% open for the transient. The ratio of the blowdown slot to diaphram area is 0.053. Thus, the diaphrams must open 5% to be equal to the area of the blowdown slot.

A separate experiment was performed to determine the diaphram opening time. The core and rupture flanges were lowered below the blowdown chute and set with a top disk of 34 psig and a lower disk of 104 psig. The top disk was completely open to the atmosphere with no obstructions. A movie was shot of the disk opening with an initial 110 psig pressure. From the movie, the disk opening was approximately 0.4 milliseconds. From the pressure history of the blowdown, the core had depressurized to less than 50 psi in less than one millisecond. The final disk opening was approximately 80% of the full area. Some fragmentation of the disk did occur. However, because the disk is not allowed to flap completely beyond the flange thickness during an experimental blowdown, the fragmentation may be less. Figure A.1 is the pressure history of this blowdown for initial pressure of 110 psig.

From the pressure histories of other experiments, changes in the local pressures of the core and blowdown chute occurred within 1 millisecond. If the shock wave from the lower rupture disk is responsible for the breaking of the other disk and foil, it would require approximately 0.3 milliseconds to reach the blowdown chute. Since, the local pressure histories do indicate a change in pressure within 1 millisecond and the shockwave could be responsible for the breaking of the other disk and foil, then it can be concluded that the breaking time of the disks is insignificant relative to the time scale of this experiment. This verifies the independent test.

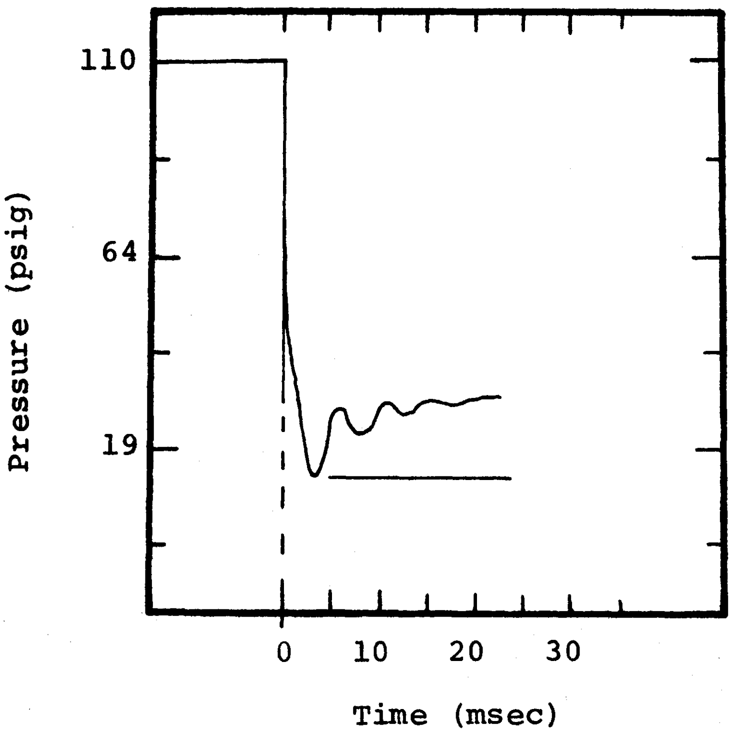

Figure A.1: Pressure history of the independent blowdown of the rupture test

APPENDIX B

EXPERIMENTAL PROCEDURES

The hydrodynamic experimental procedures require approximately one hour to perform under normal conditions. Initial set-up may take as long as one hour. However, the electronic equipment should all be turned on at the start of the day of the runs to allow warm-up for at least one hour. Replacement of the pressure seals requires a complete disassembly of the viewing region. Although disassembly and reassembly require approximately 4 hours, the RTV Silicon seal which is used as the gasket requires at least 24 hours curing time. In addition, the lower edge of glass on the baseplate is sealed with epoxy cement. All contact surfaces should be cleaned before the silicon is applied. Thus, the total downtime for replacement of the seals is about two days. All three procedures will be described separately.

Set-up Procedure

1. Turn on all electronic equipment. This includes:
   Signal Generator (oscilloscope)
   Vacuum Tube Voltmeter
   Visicorder (main power only)
   Transducer Amplifiers/Power Supplies
   Impedance Matching Power Supply
2. Set Visicorder recording speed to desired setting (50 inches per second).
3. Connect transducer cables to power supply and check for open or short circuit on amplifier meter.
4. Connect outputs of transducer amplifier/power supply to input of impedance circuit.

5. Connect output of impedance circuit to Visicorder input channels 1, 2, and 3.

6. Connect the output of the signal generator to Visicorder channel 4 directly.

7. Connect output (tee section of output from signal generator) of signal generator to relay (DPDT) such that the signal out from the relay is active when relay is normally closed (off).

8. Connect relay output to Visicorder channel 5. Make sure the grounds (shield of cables) are connected to eliminate 60 Hz bleedover from relay coil.

9. Set signal generator on 1000 Hz (preset if oscilloscope is used) at 1/2 volt peak to peak.

10. Set VTVM scale to 0.003V full scale.

11. Secure high speed movie camera to tripod. Set camera height to approximately 5 ft and distance from viewing region 6 ft.

12. Focus and assemble camera cables according to the manual for the camera.

    Camera Speed 5000 pps
    Clutch set to 0
    H/L Switch to H
    Limit switch for remote starting set at about 50 ft.
    Interval timing lamp to 1000 pulses per second
      (leave off until ready for experiment)
    f/stop 1.4 (This should be checked with the lightmeter).

13. With the core tank lowered, plug the inlet hole to the center volume of the rupture flanges with a finger & purge the solenoid operated valve (SOV) under pressure. Repeat several times to insure valve is operating properly.

14. Affix the external timing lamp (ETL) to the left side of apparatus viewing region such that it is in view of the camera as is the entire viewing region.

15. Connect the SOV, ETL and relay into one electrical tee. This tee should be placed in a protective box.
16. Connect the electrical tee into the external trigger circuit (ETC) line from the camera.
17. Test the synchronization circuit by connecting the power side of the ETC to 110 VAC. Make sure the SOV energizes, the ETL comes on, and the relay energizes. Do not leave the ETC plugged into 110 VAC when test is completed.
18. Turn on Visicorder lamp.
19. Insert the proper resister card into the Visicorder. Use the "Low" card for pressure below 4 bars. Use the "100" card for pressure 4 to 10 bars. Use the "200" card for pressures 10 to 50 bars.
20. Set the Visicorder traces such that the plenum channel can go positive the maximum possible amount (1 inch mark). Set the throat channel at about 2 inch mark. Set the core channel at about 5 1/2 inch mark.
21. With the apparatus sealed, visually observe trace deflections on the Visicorder by rapidly pulsing the pressure of the apparatus from the gas bottle. Or, with a constant pressure in the apparatus, engage the SOV. Pressure increases should deflect upscale. Pressure decreases should deflect down scale. Reverse leads of Visicorder input for any channel not responding properly. Do not allow pressure to exceed 10 psi during test.
22. Depressurize apparatus and lower core.

General note on set-up procedure: It is possible to blowout the pressure seals under low static pressure. Therefore, never exceed 10 psi when performing set-up test. It may be necessary to put a ruptured rupture disk in the flanges to provide a seal good enough to allow slight pressurization. Consult the Visicorder manual for Visicorder detailed operation.

The pressure seal replacement procedure is as follows:

Disassembly:

1. Remove all nuts from the twenty-five 3/8 inch bolts holding the angle iron frames to the glass and frame.
2. Remove the two 1/16 inch steel plates bolted to the baseplate.
3. Pull and/or unscrew the twenty-five 3/8 inch bolts from the viewing region. Do not force with a hammer and punch as this may fracture the glass. It is best to leave the top row of bolts in until last to prevent the frames from falling off prematurely. The bolts should be removed such that the back frame is removed before the front frame is free from the bolts.
4. With both frames removed, carefully chip the remaining epoxy from the lower edge of the glass windows. The windows may be partially held in place by the remaining silicone sealant and will stand alone. Precautions should be taken to prevent the windows from falling off prematurely if they are loose.
5. Remove windows.
6. Place windows on protected soft surface to prevent scratching.
7. Windows must be cleaned with lint-free cloth.
8. Clean all contact surfaces with remaining epoxy or silicone sealant using a file and/or razor blades. Surfaces must be smooth and clean before reassembly.

Assembly:

9. On the steel frame and base plate, apply a thin (1/8 inch to 1/4 inch) bead of silicone rubber sealant where the glass is going to make contact with the steel. Apply the bead around each bolt hole.

10. A 1/16 inch rubber gasket cut approximately 3/8 inch wide and shaped so that it seals between the glass and baseplate on the silicone bead should be placed on the silicone bead and pressed flat.

11. Apply another bead of silicone sealant on this rubber gasket. If the rubber is too wide, under pressure it will flatten and creep from under the edge of the window possibly blocking the blowdown chute.

12. Carefully place the windows as close to the proper position as possible on the baseplate to prevent smearing of the silicone sealant.

13. Place one frame in place and start the top center bolt through the frame and both windows.

14. Put the other frame in place and start a nut on the bolt.

15. Insert the other bolts carefully. Some may not fit well and thus must be forced. Do not hammer bolt heads. Try screwing the bolts though with light tapping on the boltheads for assistance.

16. With all bolts in place, tighten nuts. The pressure should be applied evenly as the bolts are tightened. The final tightness should be about 10 or 20 foot-pounds torque.

17. Apply epoxy along lower edge of the windows sparingly.

18. Replace 1/16 inch steel plates on baseplate. Bolt in place when applying a load such that these are flush against the bottom edge of the windows.

General Note on Assembly

Time is critical once the silicone sealant is applied. It should not require longer than 30 minutes to apply the silicone and set the windows. Full pressure should be applied by the bolts within one hour. If time is available, let the silicone dry

24 hours before applying the epoxy and steel plates. Then let the epoxy set 24 hours with the plates in place. The valve and inlet on the upper tank should be open during the setting process. The windows and frames will only fit one way.

Experimental operating procedure:

1. Fill 1/2 gallon bottle with water and place out of the way.
2. From calculations, decide which rupture disks are to be used.
3. Place rupture disk in rupture flanges. Handle the rupture disks carefully. Make sure the proper disk is in its proper position and sitting straight in the flanges.
4. Tear off a sheet of aluminum foil approximately 8 to 10 inches wide. Fold two opposite edges so that it is 8 inches wide.
5. Place above the top rupture flange. Make sure there are no holes or creases in this foil.
6. Raise the core tank making sure all flanges fit together snuggly. Keep the boltholes of the flanges colinear during this process.
7. With the jack applying a slight upward force on the apparatus, secure the core with the eight 3/4 inch bolts. These bolts must be tightened with at least 50 foot-pounds torque.
8. Set the floodlights in place. Make sure the paper grid is in place on the back window and centered on the blowdown chute slot.
9. Lower jack and check to see core drain plug is in place.
10. Place missile shield between operating position and apparatus.
11. Record temperature reading of water.
12. Record ambient temperature reading.
13. Record atmospheric pressure reading.

14. Record date and time.

15. Record pressure disk used, liquid and gas types, and run number.

16. Load one roll of 7277 High Speed 4-X Reversal B&W film into the movie camera under subdued light conditions. See camera instruction manual for procedure.

17. Depress safety switch in camera with the eraser end of a pencil. No power should be to the camera at this point.

18. Label all film containers.

19. Check Visicorder paper supply. 10 to 30 feet of paper is required for each run depending on the operation. If empty or below 10 feet, replace with a new roll of Visicorder paper.

20. When the water temperature is approximately ambient temperature, (or for freon out of the can) insert into viewing region to a level 12 inches above the baseplate. Close the air bleed valve and liquid intake port.

21. Record liquid level height.

22. Check that no obstructions exist between the camera lens and the apparatus.

    Note: Steps 23 to 39 are of critical time importance, avoid unnecessary delays.

23. Record temperature of gas plenum.

24. Plug in ice point reference junction to lower thermocouples in core.

25. Plug in power to camera (110 VAC).

26. Plug in external trigger circuit to 110 VAC. If circuit is energized, recheck film loading. Circuit should not be energized.

27. Plug in internal timing light and set to 1000 pulses per second.

28. Check transducer power supplies meter again.

29. Check viewing region to see that all ports are closed off.

30. Open center volume valve (CVV) (rupture flanges) and core tank valve (CTV).

31. Increase pressure (from gas bottle) until center volume is 10 or 20% under the calculated required pressure for the center volume.

32. Close the CVV.

33. Pressurize lower tank to 10 or 20% below the desired level. Do no overpressurize. Keep an eye on the center volume pressure as it should slightly increase to the desired pressure because of the lower disk swelling. If it does not increase to desired level, do not exceed the gauge pressure for rupture of the lower disk but reopen the CVV and pressurize to the desired level. The calculations should have been such that a tolerance of 3-5 psi is allowed. Close the CVV.

34. Bring the core up to desired pressure and close the CTV. Slight leaks from the core (2 psi/minute) can be tolerated. Record both pressures.

35. Record core gas temperature from both thermocouples. Thermocouples require 10 seconds to react.

36. Double check pressure settings. Immediately proceed with steps 37 and 38, if pressure is set.

37. Turn on flood lights.

38. From behind the missile shield, simultaneously start the Visicorder and the camera. If run fails, quickly de-energize the ETC and depressurize the core tank and center volume after immediately turning the Visicorder off. If successful, turn off Visicorder after the audible indication of the blowdown. Human reaction time is long enough so all the data is recorded.

40. Unplug the ETC.
41. Turn off the floodlights (let them cool down).
42. Turn off and unplug the internal timing lamp.
43. Unplug the camera. Remove floodlights.
44. Tear off recording paper from Visicorder and label the traces accordingly.
45. Unload the camera in subdued light.
46. Drain core tank from drain on bottom plate.
47. Release bolts through the rupture flanges and lower tank with jack.
48. Make observations about how the rupture disks broke and any foil blockage.
49. Open top viewing region ports. (air bleed in liquid intake).
50. Refill 1/2 gallon bottle with water and begin again for new experiment.

General Note on Operating Procedure

From time to time, the lower end plate on the core should be removed and the bottom cleaned out. Teflon® seal should be applied to core drain plug and intake plug to insure a gool seal.

After several high pressure (greater than 5 bars) experiments, the seals on the viewing region will fatigue and start to leak. Small leaks can be tolerated. Check the loss of liquid by comparing the volume of liquid drained off to the initial liquid volume. Also, any leak must be of pinhole magnitude since momentum losses could become significant if a large leak developed. Low pressure (less than 5 bars) experiments generally do not fatigue the seals quickly.

For the thermal-hydraulic experiments, it is necessary to let the gas in the core rise to the desired temperature. This is accomplished by the electric heater and should be performed before inserting the liquid freon into the viewing region at step 20 of the operating procedure.

The electric heater is of the immersion type and not specially designed for stagnet air heating. The heater should be kept to no more than 10 watts per square which corresponds to voltage of 60 VAC to prevent burnout of the heater element.

APPENDIX C

CALIBRATION DATA

Calibration was required of the visicorder, thermocouples, and pressure gauges. The pressure transducers were factory calibrated by PCB Piezotronics. The vacuum tube voltmeter was gauged against other voltage sources and meters.

C.1 Visicorder Calibration

The Visicorder required the use of scaling resistors to adjust deflections for certain input voltages. The resistance values were calculated according to the visicorder manual. Three sets of scaling resistors were made. Each set of resistors was placed on a printed circuit board which was plugged into the Visicorder. The boards were titled "low", "100" and "200". The "low" card was set for low pressure, 1 to 4 bars, experiments. The "100" card was set for pressures in the range of 4 to 10 bars experiments. Up to 20 bar experiments can be run with "200" card. Table C.1 lists the shunt and series resistors placed on each card. Table C.2 lists the calibration results of each card for various input voltages. The calibration tests were performed under steady state conditions with the impedance circuit in series. The fourth channel on each card was set for 1/2 volt timing signal.

During the course of the experiments, channels 1, 2, and 3 are hooked up to the plenum, blowdown chute, and core pressure transducers, respectively. From the factory calibration data, each channel inches/volt data was converted to psi/inch data. Table C.3 contains final calibration data for transient pressure measurements.

Error of the calibrations resulted from reading errors of the voltage readings, deflection measurements, and transducer error. The errors were 1.6%, 8.3%, and 13.2% for the "low", "100", and "200" cards, respectively.

C.2 Thermocouple Calibration

The thermocouples were calibrated with an ice bath and a boiling bath. Atmospheric conditions at the time of calibration were 20°C and 15 psi. The results of the calibration are given in Table C.4. The three readings for each of three thermocouples were taken at 10 minute intervals for each bath. The manufacturer specifies an error of 3/4% in linearity over a 500 degree range from 0° to 500 °C. The conversion factor from millivolt thermocouple reading to degrees centigrade is 17.37 "C/mV.

C.3 Pressure Gauge Calibration

The pressure gauges were calibrated with a dead weight tester made by Ashcroft Type No. 1300. Table C.5 shows the calibration data for both gauges.

C.4 Pressure Transducer Calibration

The pressure transducer calibration data is shown in Figure C.1 for all three transducers. Specifications of each transducer are also shown on this figure. Transducer with serial number #526, #1423, and #916 were used in the plenum, blowdown chute, and core, respectively.

TABLE C.1

Resistance Values for each Channel of the Scaling Cards Used in the Visicorder

	Resistance (ohms)	
	Series	Shunt
"Low" Card		
Channel 1	1000	430
Channel 2	1000	430
Channel 3	1000	430
Channel 4	2000	430
"100" Card		
Channel 1	4700	390
Channel 2	4700	390
Channel 3	4300	390
Channel 4	2000	430
"200" Card		
Channel 1	10,000	360
Channel 2	10,000	360
Channel 3	10,000	360
Channel 4	2000	430

TABLE C.2

Resistor Card Calibration Data for Visicorder

	Channel	Voltage Input	Deflection (inches)	Inches per Volt
"Low" Card				
	1	0.50	1.733	3.47
	1	1.02	3.433	3.37
	2	1.02	3.533	3.46
	2	0.50	1.727	3.45
	3	0.51	1.760	3.45
	3	1.00	3.393	3.39
"100" Card				
	1	1.00	0.820	0.82
	1	2.00	1.613	0.81
	1	3.00	2.417	0.81
	2	3.00	2.400	0.80
	2	2.00	1.600	0.80
	2	1.00	0.793	0.79
	3	1.00	0.923	0.92
	3	2.00	1.850	0.93
	3	3.00	2.747	0.92
"200" Card	1	3.00	1.215	0.41
	1	6.00	2.427	0.40
	1	8.00	3.250	0.41
	2	3.00	3.303	0.41
	2	6.00	2.450	0.41
	2	3.00	1.250	0.42
	3	3.00	1.270	0.42
	3	6.00	2.550	0.43
	3	8.00	3.383	0.42

TABLE C.3

Calibration Data for Direct Psi/Inch Readings for the Pressure Measurements

Card	Ch 1	Ch 2	Ch 3
Low	11.3	11.8	12.3
100	47.4	50.8	45.7
200	94.2	99.2	100.0

Calibration from factory

Output (mV/psi)	25.9	24.6	23.8

TABLE C.4

Thermocouple Calibration Data

	Thermocouple (mV)		
	1	2	3
Boiling Water			
100 °C	5.7	5.7	5.8
	5.7	5.8	5.8
	5.8	5.7	5.8
Ice Water			
0 °C	0.0	0.0	0.0
	0.0	0.0	0.0
	0.0	0.0	0.0

TABLE C.5

Pressure Gauge Calibration Data

	Pressure Readings (±.5 psi)	
Pressure (psi)	Gauge 1	Gauge 2
5	5	-
10	10	10
20	20	20
25	25	25
30	30	30
40	40	-
50	50	50
75	76	75
100	101	100
125	126	125
150	150	150
175	175	174
200	200	199

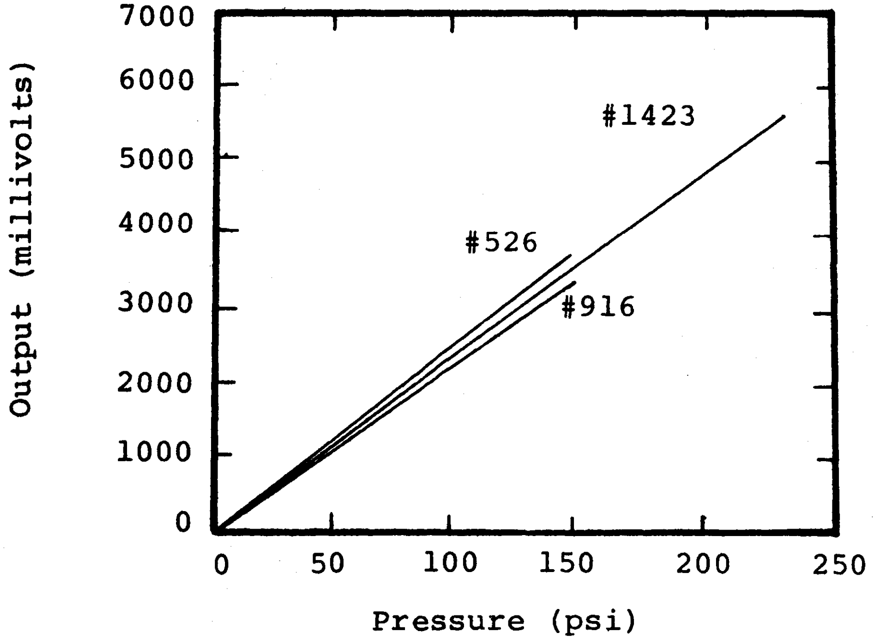

Characteristic	#526	#916	#1423
Sensitivity (mv/psi)	25.9	23.8	24.6
Linearity (%)	1	1	1
Rise Time (μsec)	1	1	1
Natural Frequency (kHz)	450	450	450

Figure C.1: Pressure transducer calibration curves and specifications

APPENDIX D

EXPERIMENTAL FAILURE ANALYSIS

In order to estimate the amount of expendable materials required to perform a set of experiments, a fault tree type analysis was performed on the mechanical, electrical, and human components of the experiment.

The fault tree top box was "failure of apparatus to take data on demand." Thirty-two possible basic errors were identified which could cause a failure of the experiment. Some occurred more than once bringing the total to sixty-seven causes for failure. Since no redundant systems were used, the fault tree consisted of "or" gates. Figure D.1 (14 pages) is a chart of the fault tree showing the connections and logic of the analysis. Table D.1 is a list of the possible failures, with repetitions indicated, the failure class to which it belongs, and failure probabilities. Table D.2 is a summary of failure probabilities according to class. The failure probabilities were determined from manufacture correspondance, Reactor Safety Study [21], and "engineering" guesses. From Table D.2, it can be seen that the rupture disks contribute the most significant portion to the overall failure probability. The final average failure probability is 0.6. This compares well to a hydrodynamic experimental failure rate of 0.61. It should be pointed out that the first seven hydraulic experiments were failures due to adjustment in experimental procedure. As was expected, expertise increased with time as is shown by the lower failure of thermal-hydraulic experiments which was 0.11.

TABLE D.1

Failure Modes and Probabilities

Device	No. of Units	Class	Probability
Pressure Transducer	3	Elec.	5×10^{-7}
Electronics	8	Elec.	5×10^{-7}
Cables	8	Mech.	1.6×10^{-6}
High Speed Camera	1	Mech.	8.3×10^{-6}
Improper Film Loading	1	HC	3×10^{-3}
Camera or Light Misalignment	2	HO	3×10^{-3}
Misalignment after Setup	1	Guess	1×10^{-2}
Camera Lens	1	Mech.	1×10^{-5}
Setting of Camera Lens	2	HC	3×10^{-3}
Lights (6 hr Lifetime)	6	Mech.	1.4×10^{-2}
Relay	1	Elec.	1.2×10^{-9}
Electronics off	5	HO	6.5×10^{-3}
Camera Timing Bulb (10 hr Lifetime)	1	Elec.	8×10^{-3}
Electrical Connection	3	Elec.	1×10^{-2}
Light Bulb (500 hr)	1	Elec.	1.7×10^{-5}
Switching Under Stress	2	Selection	2×10^{-2}
Mechanical Switch	3	Mech.	1.4×10^{-9}

Table D.1 (continued)

Device	No. of Units	Class	Probability
Visicorder	1	Mech.	5×10^{-4}
Visicorder w/o Paper	1	HO	6.5×10^{-3}
Obstructed View	1	HO	6.5×10^{-3}
Gasket Leak	1	Mech.	1.5×10^{-6}
Water not in Place	1	HO	6.5×10^{-3}
Intake Port Open	1	HO	3×10^{-3}
Air Bleed Valve Open	1	HO	3×10^{-3}
Incorrect Pressure	2	Guess	1×10^{-3}
Aluminum Foil	1	Mech.	0.01 to 0.4
Rupture Disk	2	Mech.	0.1
Improper Disk	2	HC	1×10^{-2}
SOV	1	Mech.	2×10^{-5}
AC Power	1	HO	3×10^{-3}
Limit Switch	1	Elec.	6×10^{-6}
Switching No Stress	1	HO	3×10^{-3}

Class Key

Mech. = Mechanical type failure
Elec. = Electrical type failure or pertaining to electronics
HO = Human error by omission
HC = Human error by commission
Selection = Human error by selection of process
Guess = Engineering approximation

TABLE D.2

Summary of Failure Probabilities by Class

Failure	Probability
Mechanical failure not including aluminum foil or rupture disk	0.051
Mechanical failure including aluminum foil and disk	0.41 (average)
Electrical failure	0.037
Human error by commission	0.019
Human error by omission	0.044
Other	0.031

Overall Failure Probability = 0.60

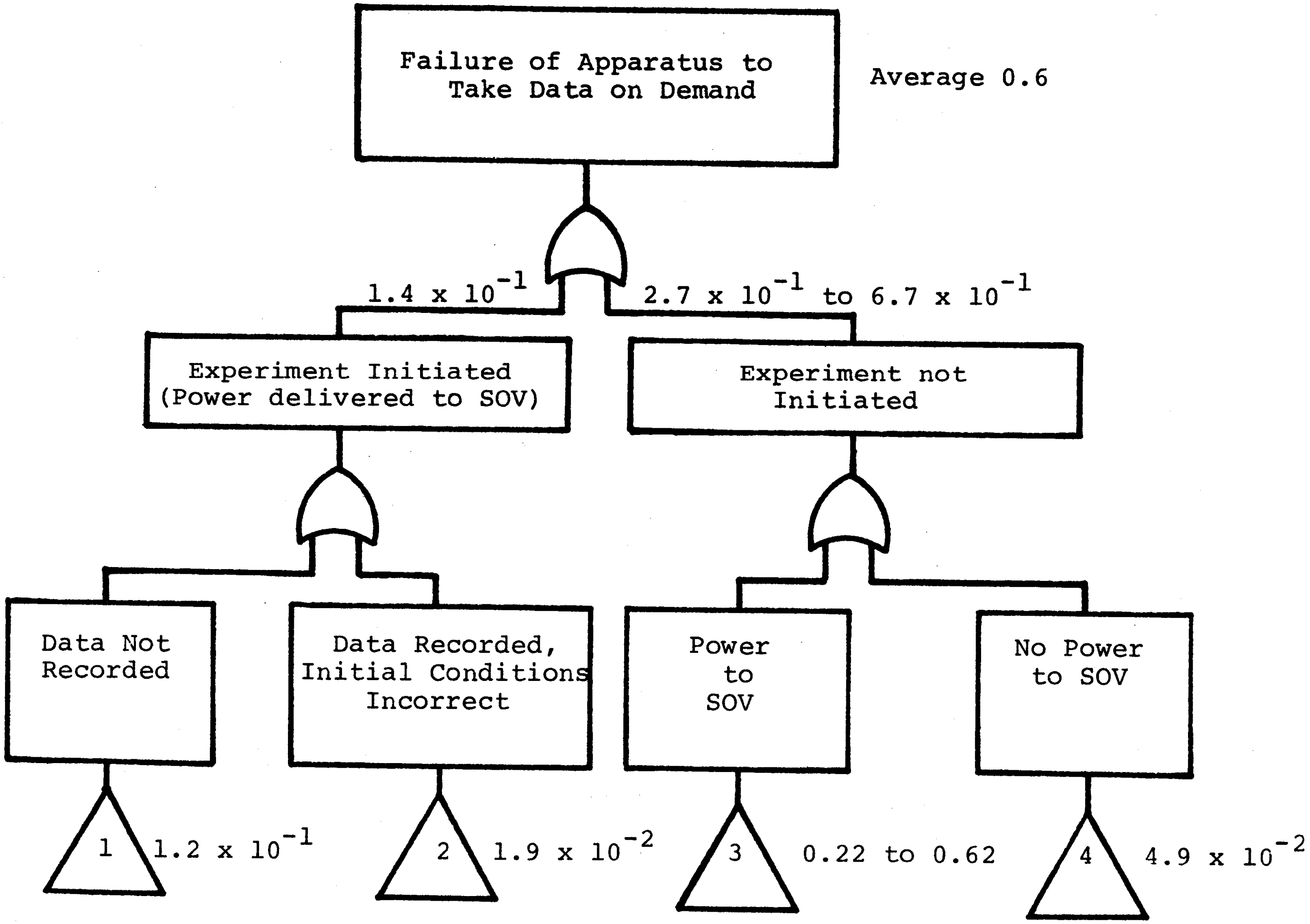

Figure D.1: Fault tree of experimental apparatus (1 of 14)

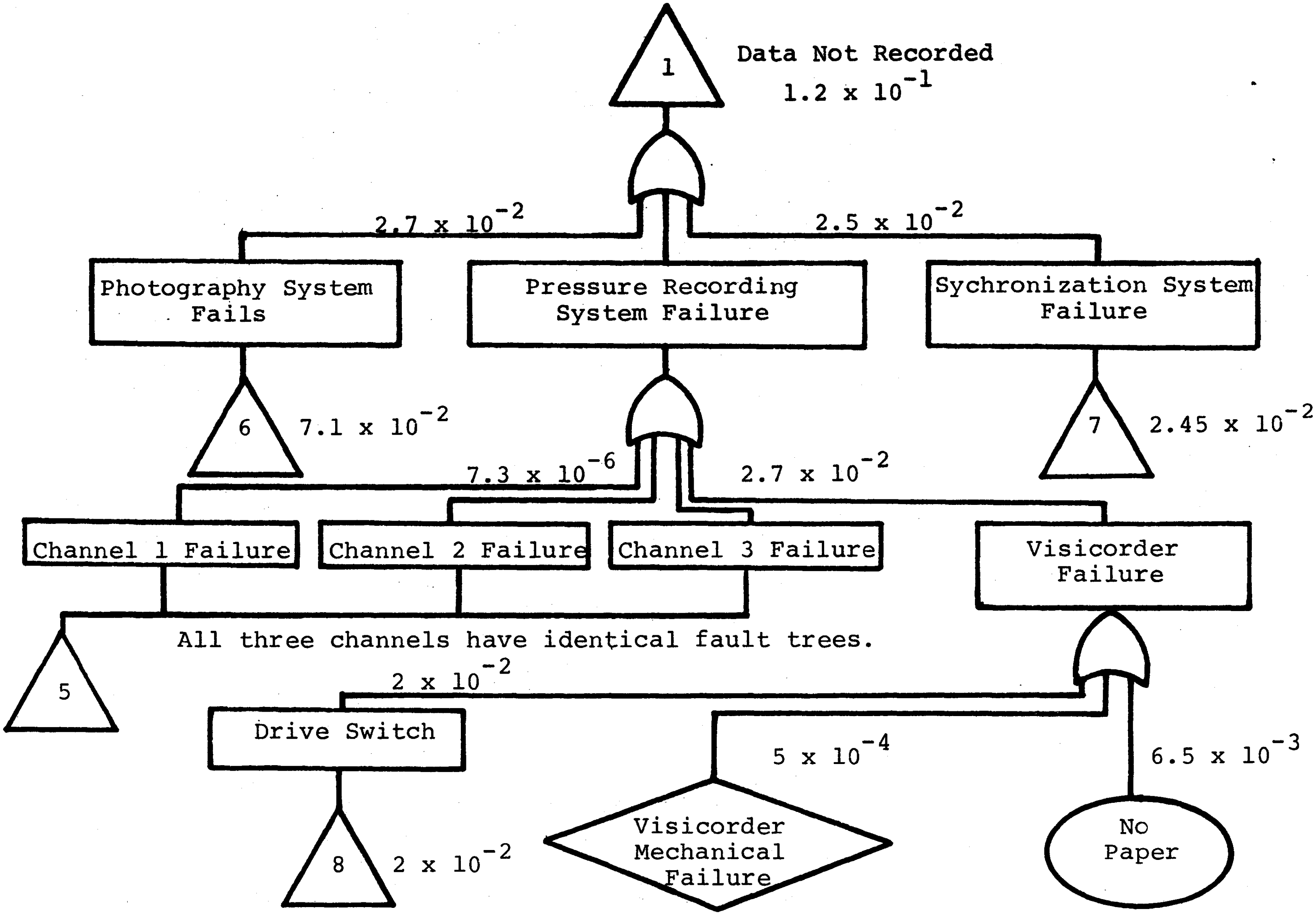

Figure D.1: (2 of 14)

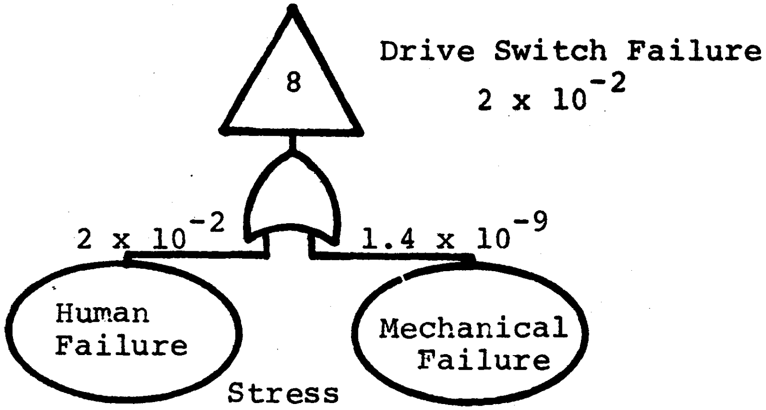

Figure D.1: (3 of 14)

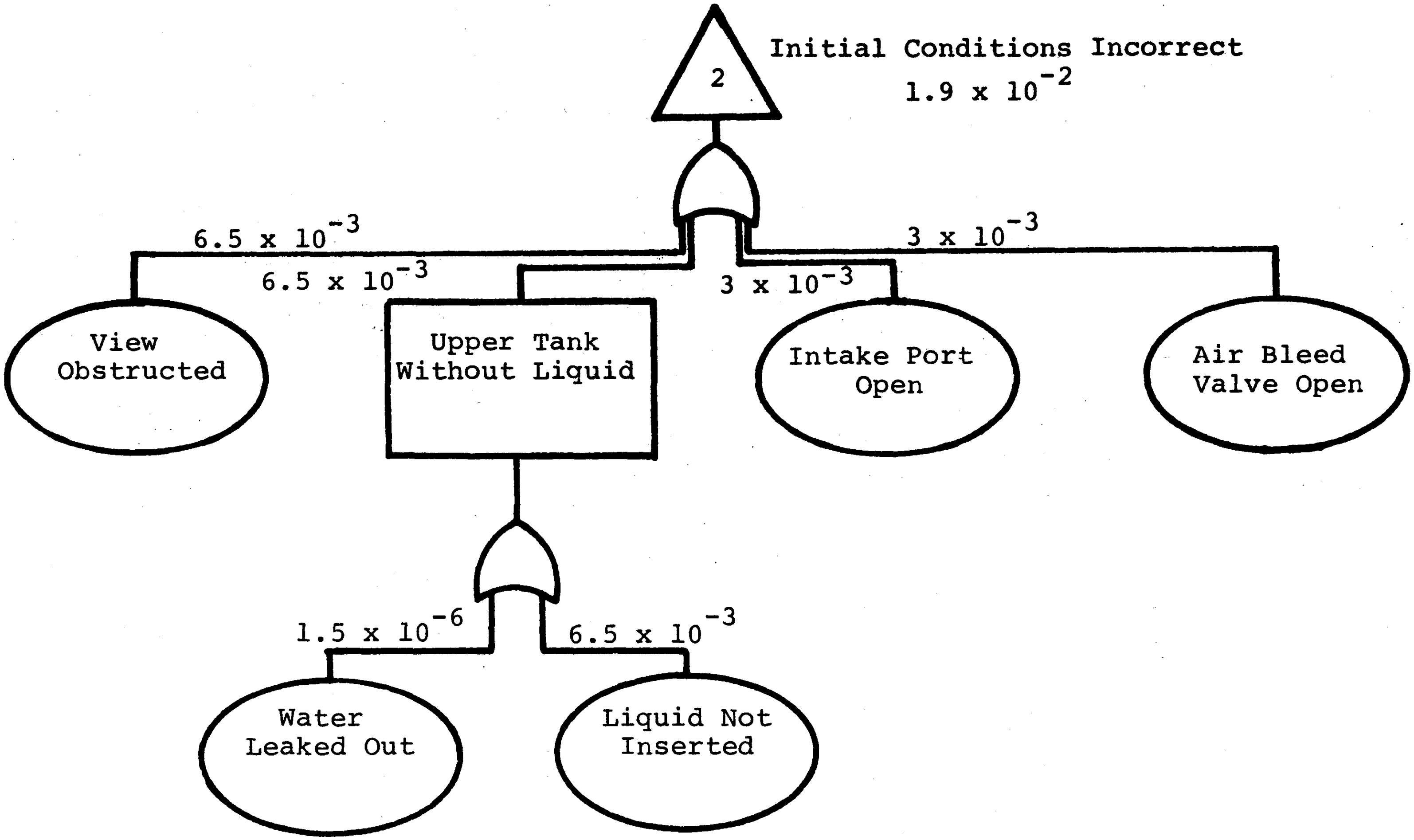

Figure D.1: (4 of 14)

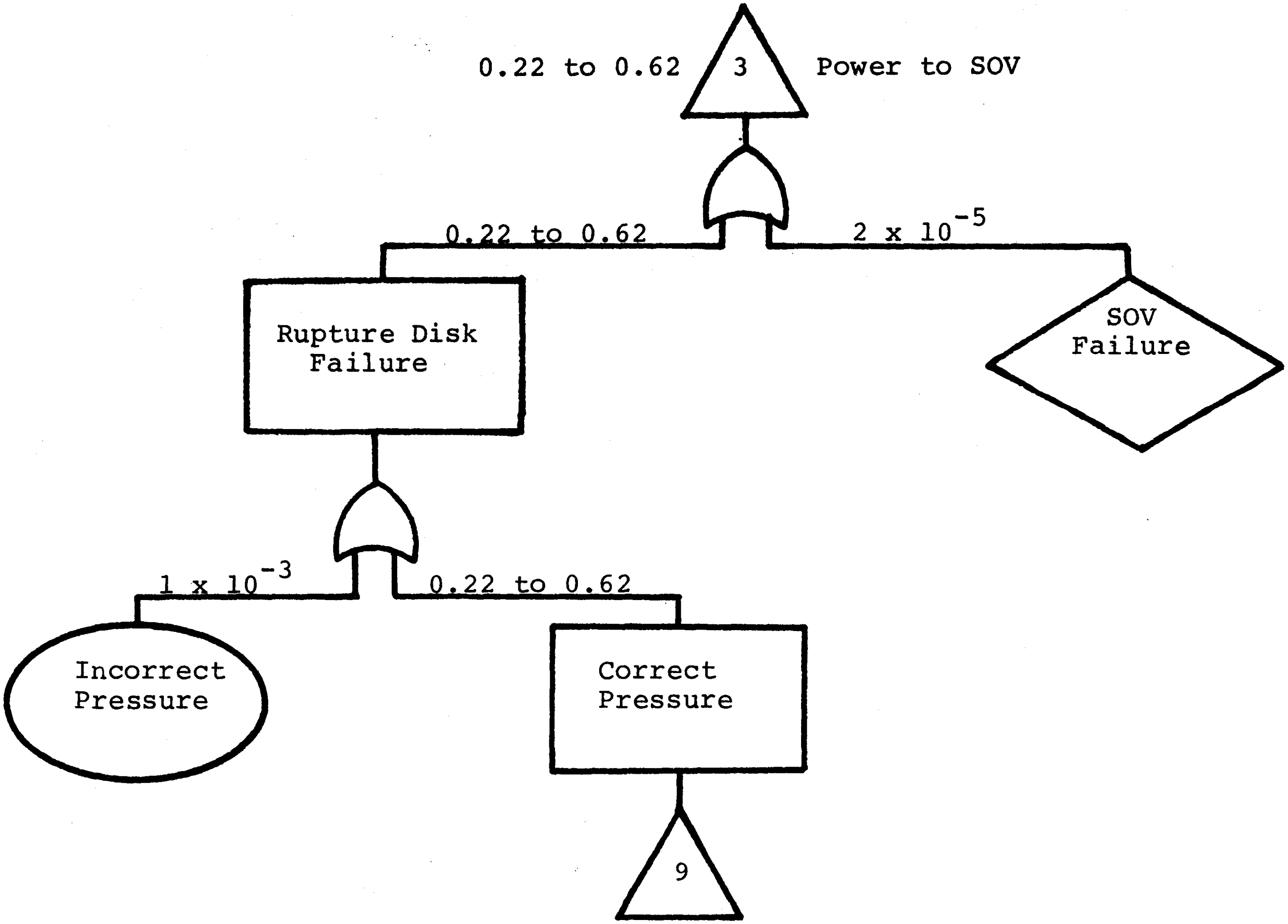

Figure D.1: (5 of 14)

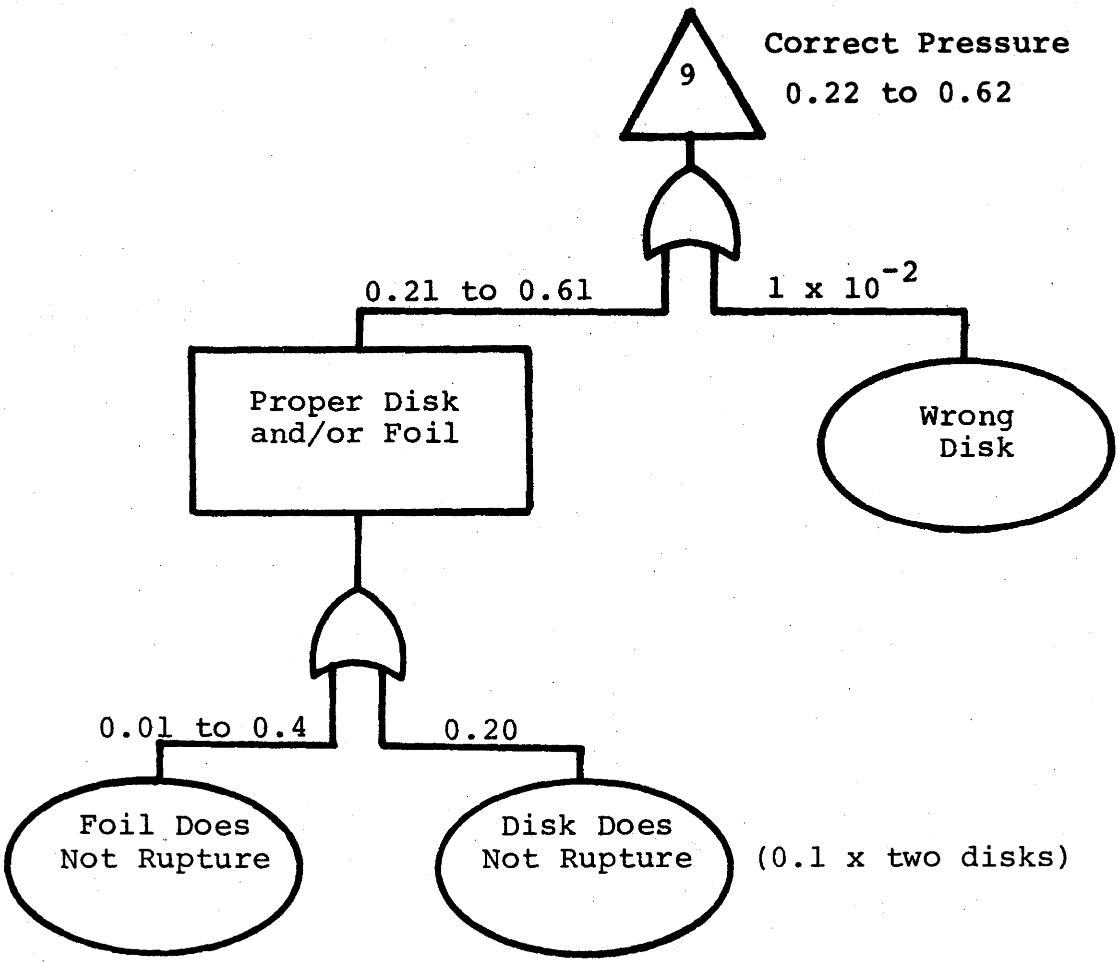

Figure D.1: (6 of 14)

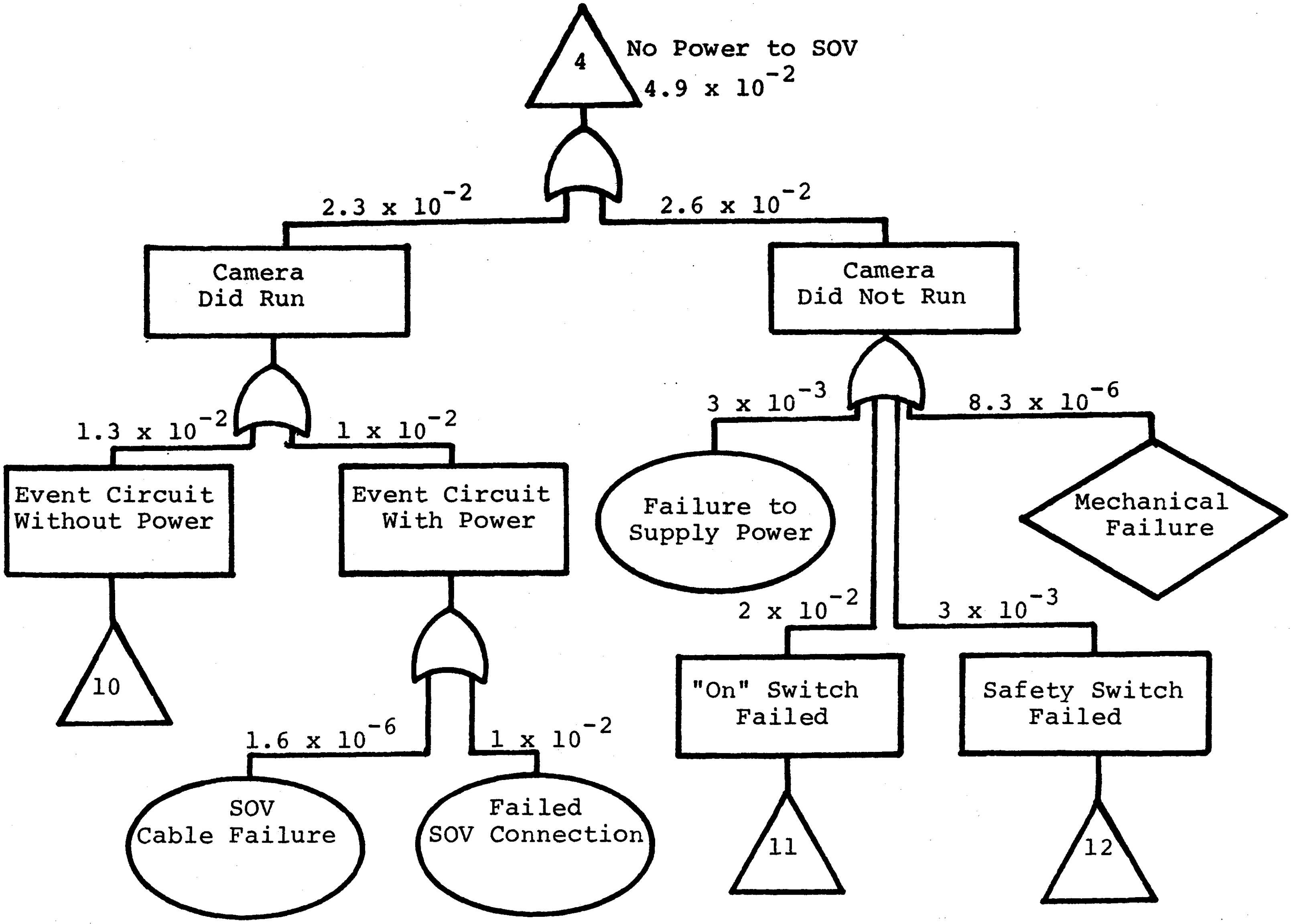

Figure D.1: (7 of 14)

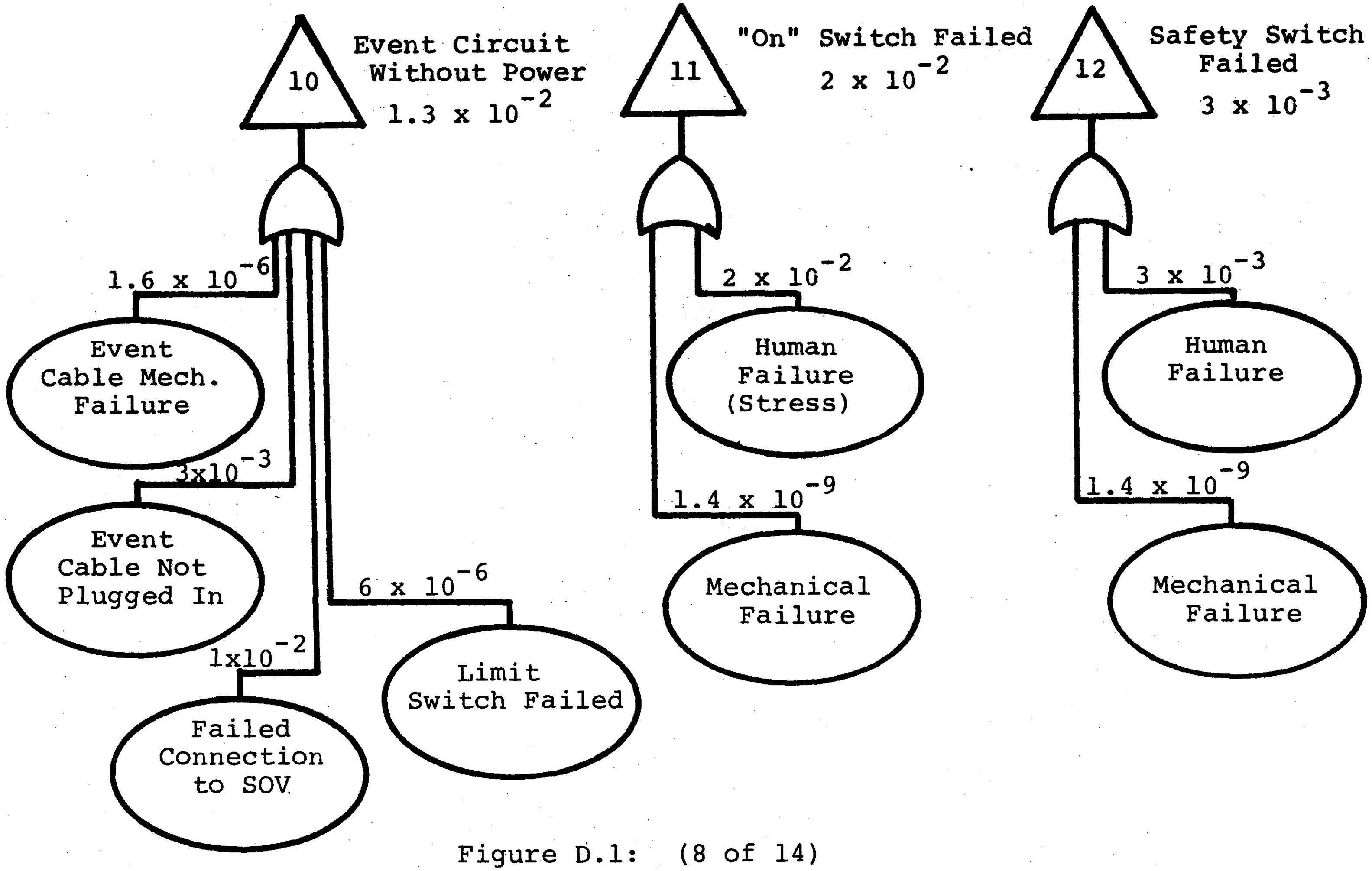

Figure D.1: (8 of 14)

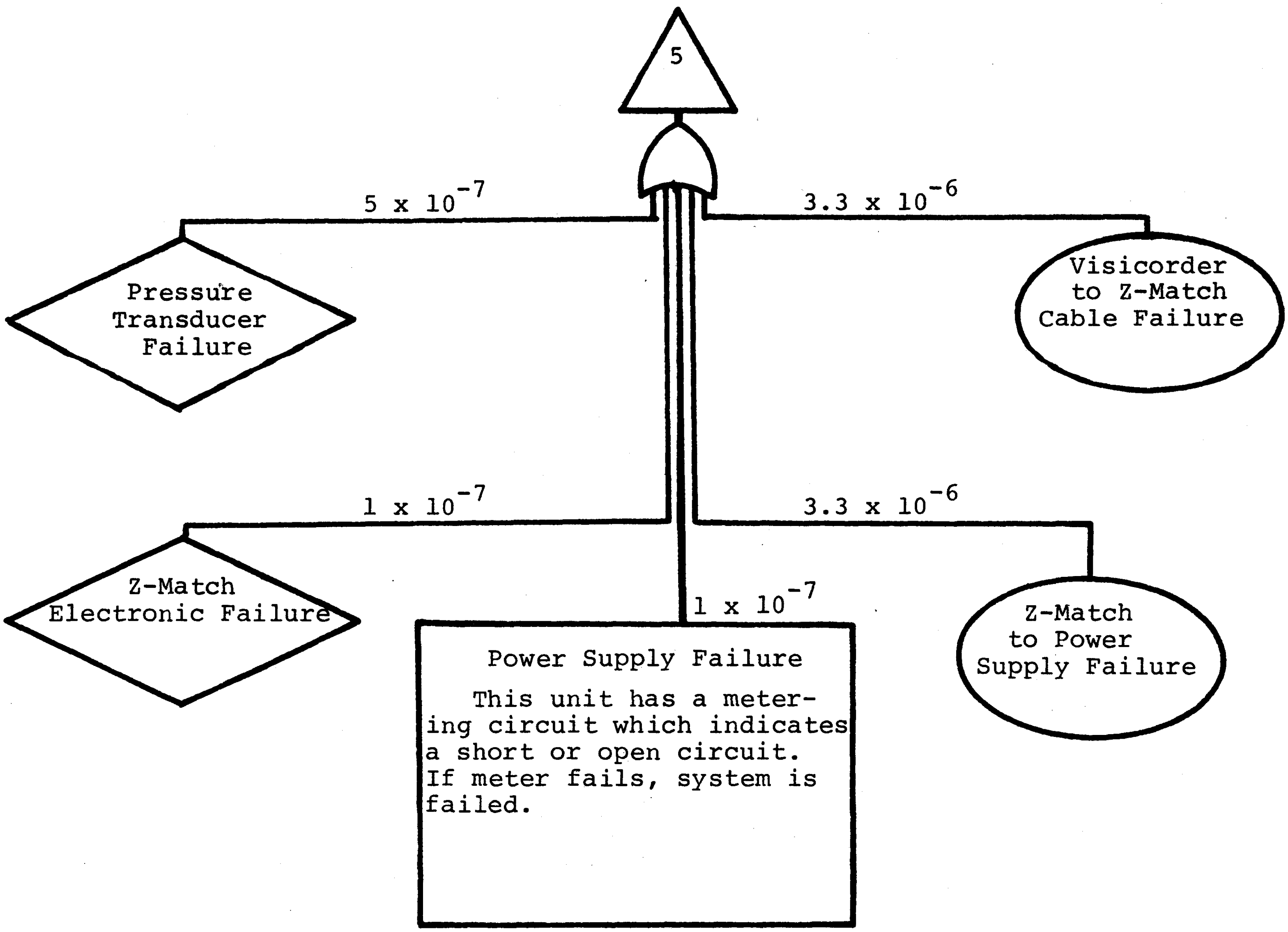

Figure D.1: (9 of 14)

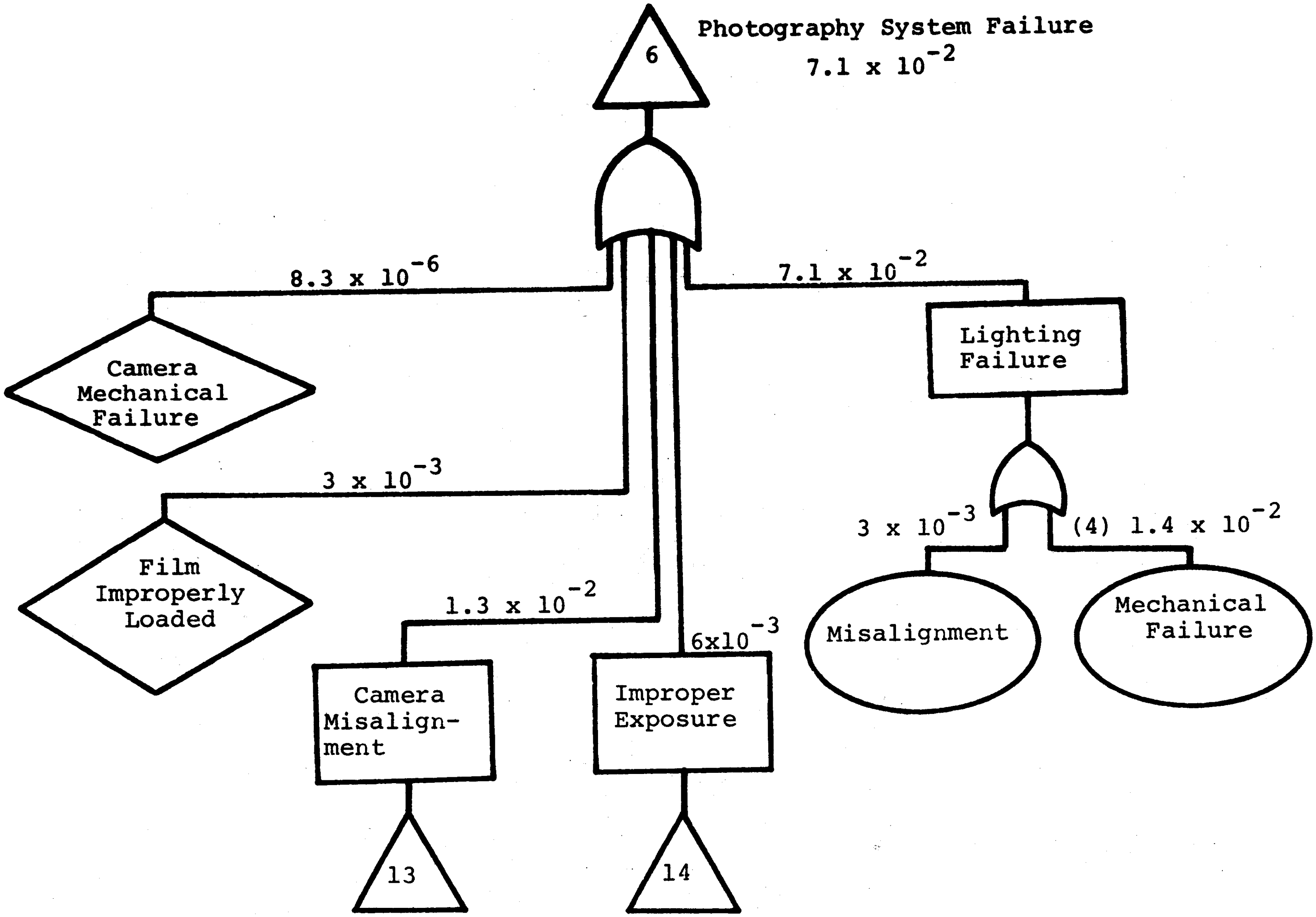

Figure D.1: (10 of 14)

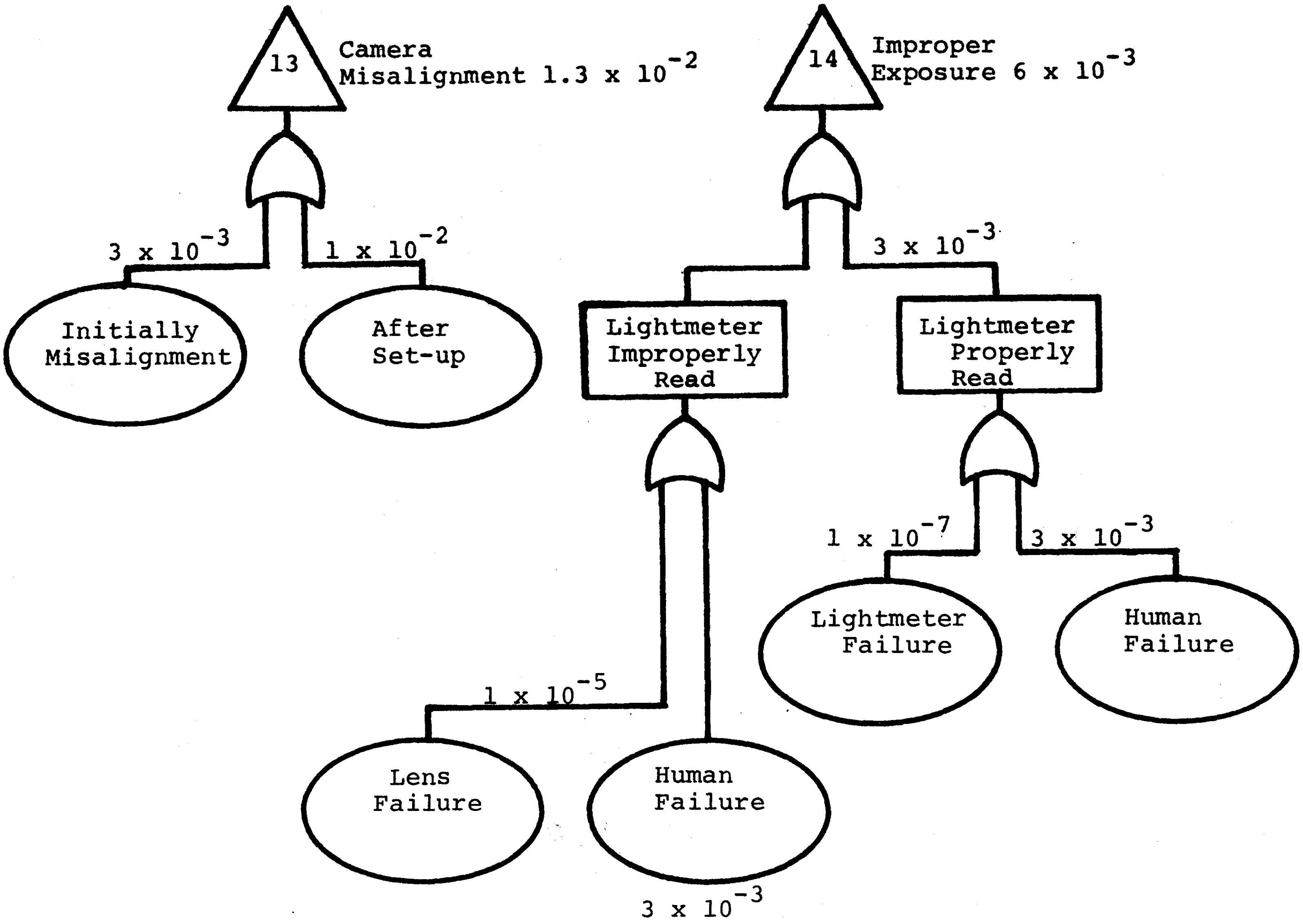

Figure D.1: (11 of 14)

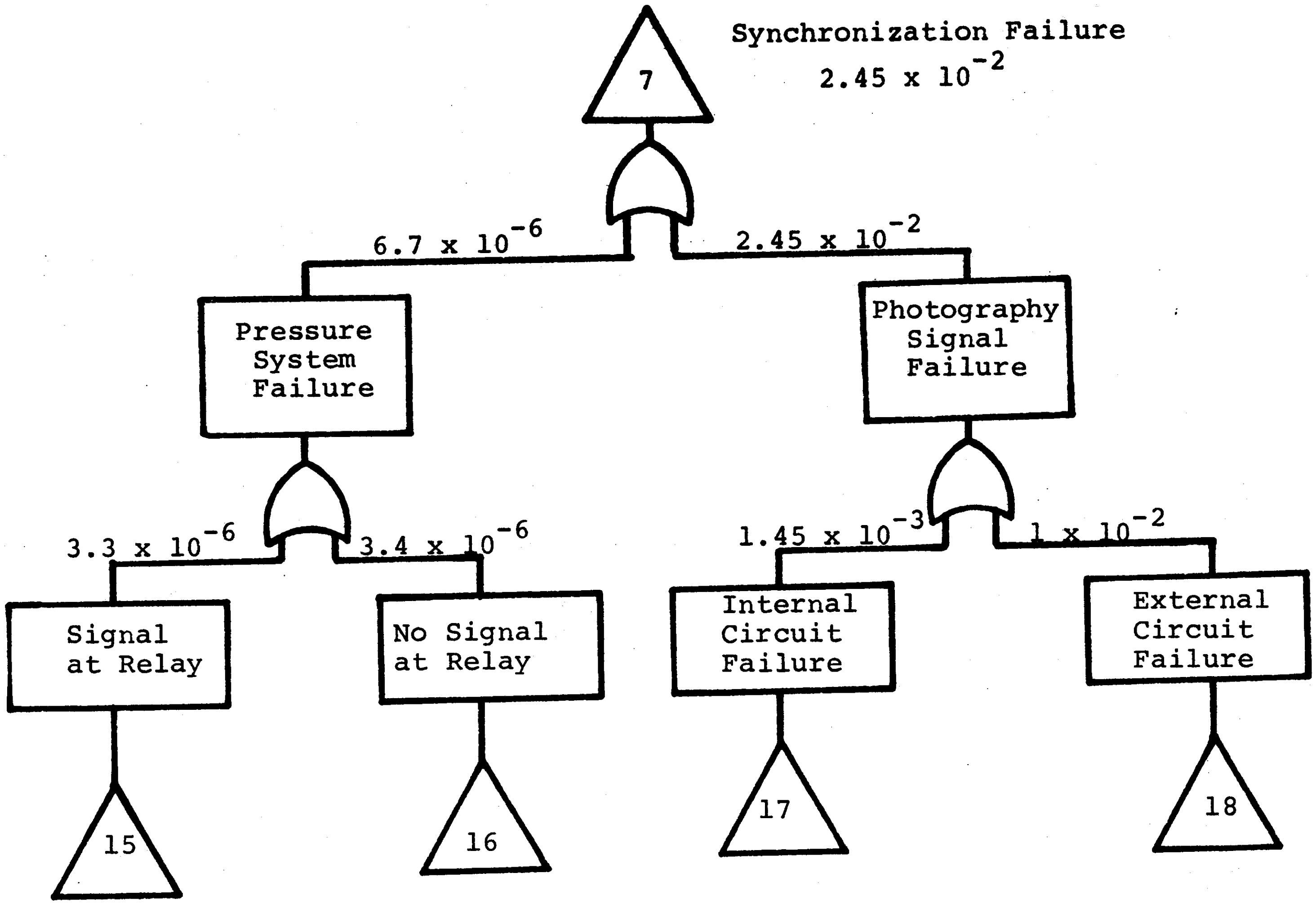

Figure D.1: (12 of 14)

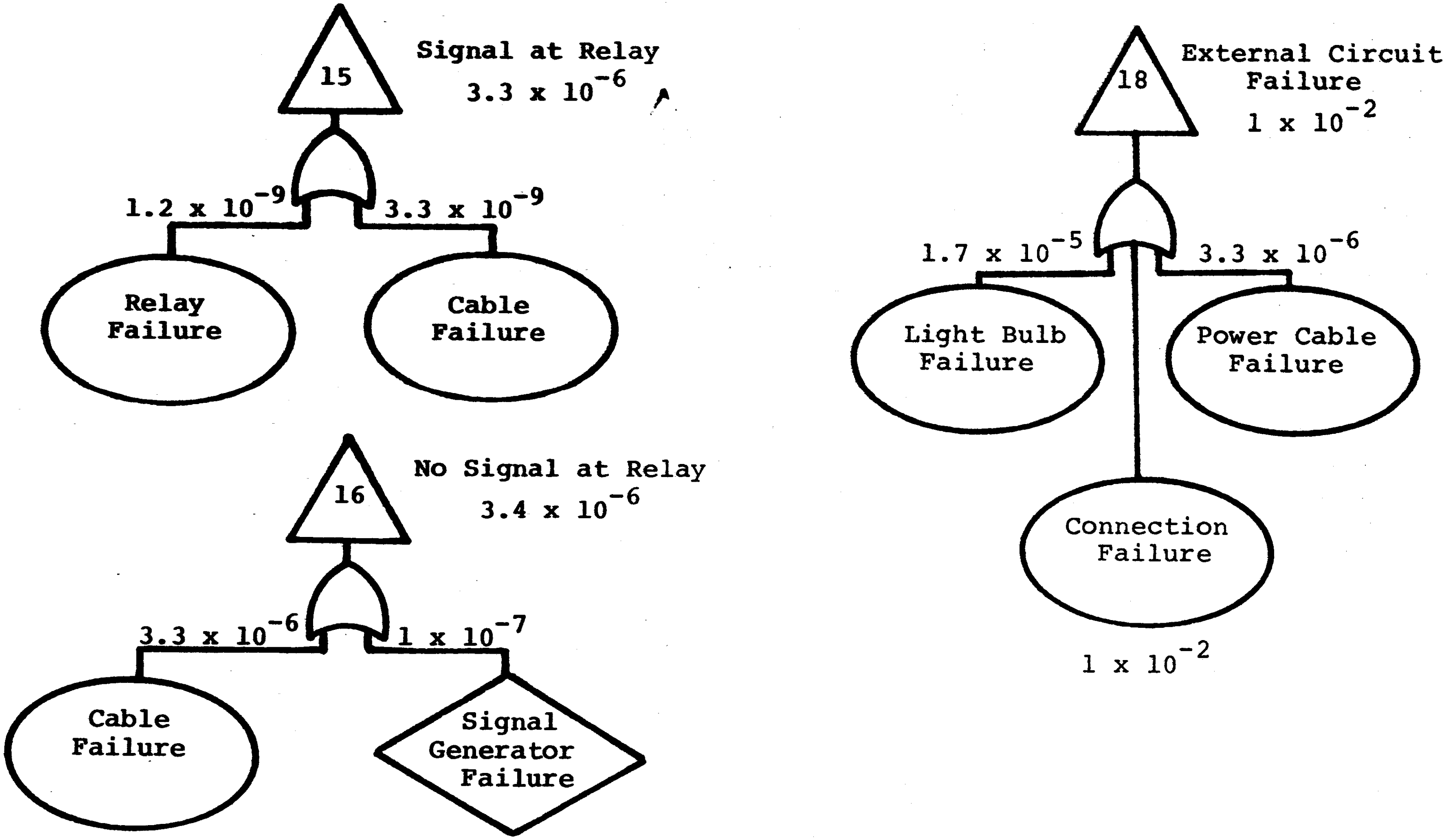

Figure D.1: (13 of 14)

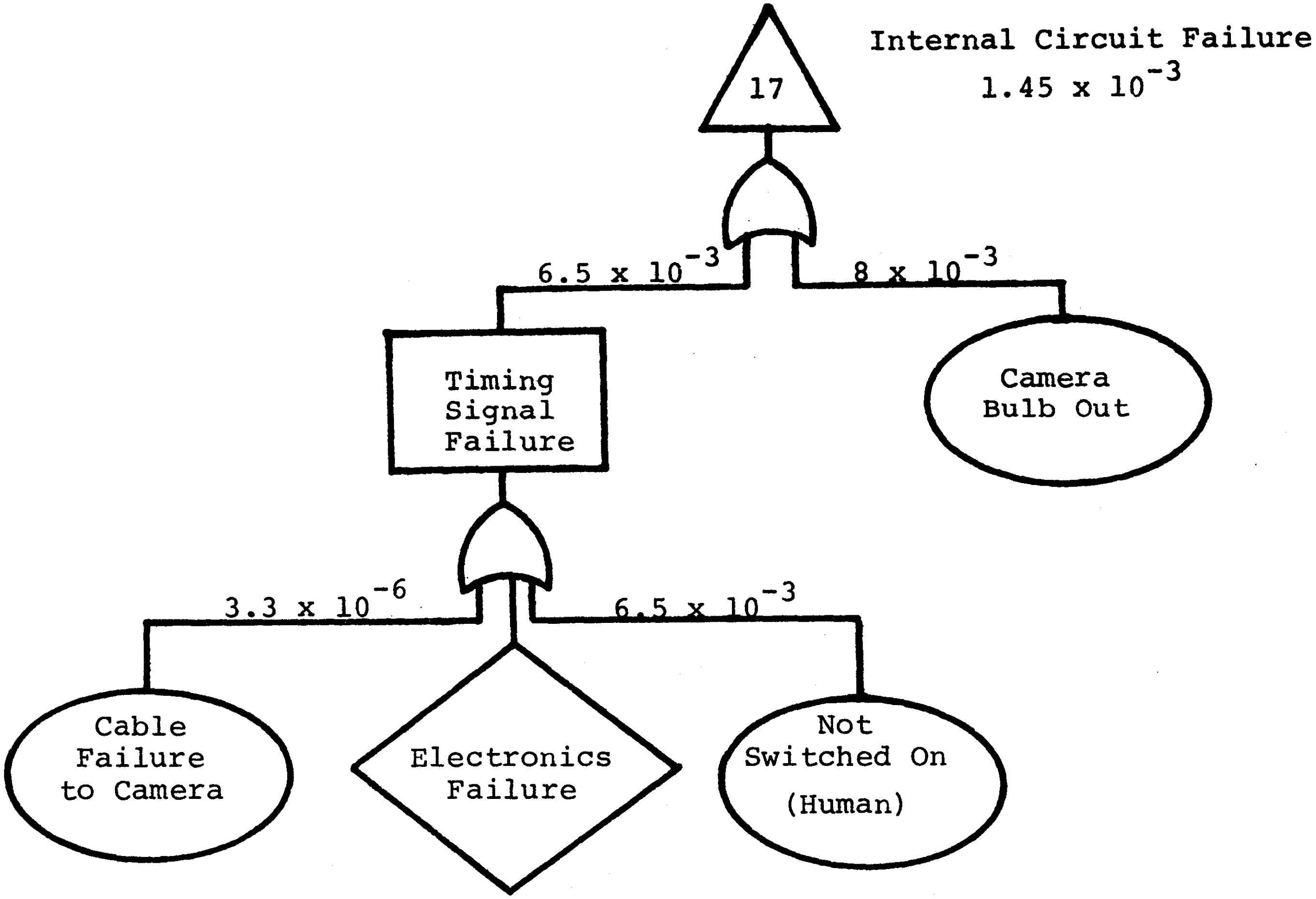

Figure D.1: (14 of 14)

APPENDIX E

TYPICAL PRESSURE HISTORY

An actual pressure history is shown in Figure E.1 for run TH2. This illustrates all the major pieces of information which can be extracted from the Visicorder pressure trace. The major pieces of information are the plenum pressure, chute pressure, core pressure, 1000 Hz timing signal, and starting mark indicator. As shown, the core pressure slightly depresses before actual rupture of the disk. The rupture point is easily detectable from the core and chute pressure traces. Speed calibration is made from the 1000 Hz signal. Pressure values are determined from known calibrations and deflections, and are calculated accordingly. Sample calculations are included in Figure E.1.

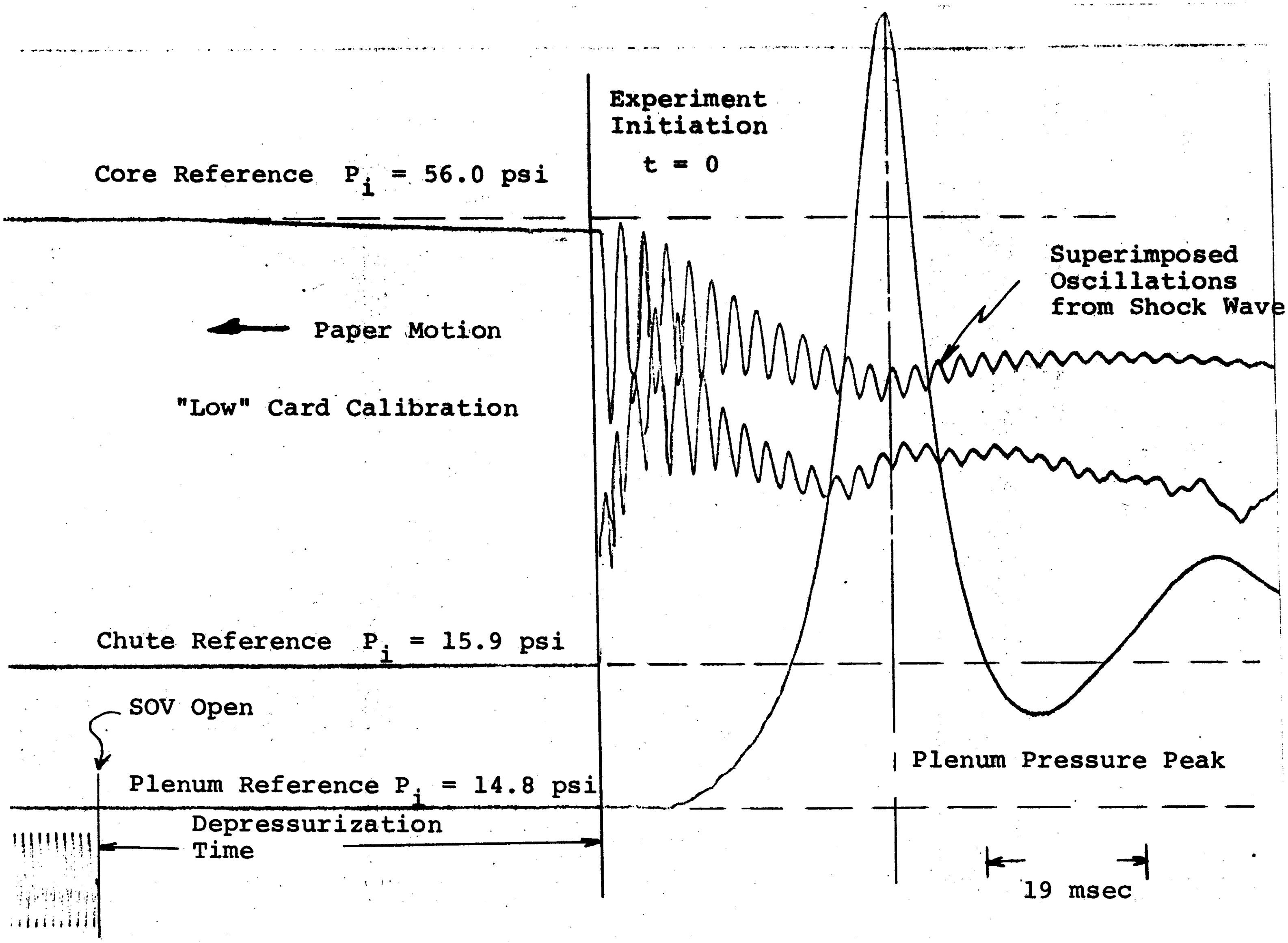

E.1: Pressure history of run TH2

APPENDIX F

CORRADINI'S MODEL FOR LIQUID ENTRAINMENT BY A GAS JET

The jet transient is modeled by an isentropic expansion, with the expanding gas volume lumped as one common uniform pressure and temperature system. The gas is treated as a perfect gas with constant properties. The expansion is assumed to be one-dimensional and to occur in two stages. When the gas is expanding through the blowdown chute, the liquid slug is treated as the liquid mass of the blowdown chute. When the gas enters the viewing region, the liquid slug becomes that of the liquid in the viewing region and the blowdown chute. The gas is assumed to act across the whole cross section of the upper pool. The cover gas is also lumped into one system and isentropically modeled. The governing momentum equation is given by

$$a = \frac{d^2x}{dt^2} = \frac{P_g - P_{p\ell}}{M_{slug}} \tag{F.1}$$

where

$$P_g = \frac{M_g R_g T_g}{V_g} \tag{F.2}$$

$$R_g = R_o/MW_{gas} \tag{F.3}$$

$$V_g = A_p X \tag{F.4}$$

$$P_{p\ell} = P_{p\ell,i}\left(\frac{V_{p\ell,i}}{V_{p\ell}}\right)^{\gamma} \tag{F.5}$$

$$V_{p\ell} = V_{total} - V_g \tag{F.6}$$

$$V_{total} = \text{constant} = V_{g,i} + V_{p\ell,i} \tag{F.7}$$

The initial conditions then are the initial core volume ($V_{g,i}$), the gas plenum volume ($V_{p\ell,i}$), the mass of gas (M_g), and the temperature of the gas (T_g). The energy equation for an adiabatic expansion is

$$\frac{dU}{dt} = \frac{-dW}{dt} \tag{F.8}$$

$$\frac{d}{dt}\left(\frac{M_g R_g T_g}{\gamma-1}\right) = -P_g \frac{dV_g}{dt} \tag{F.9}$$

$$\frac{dT_g}{dt} = \left(\frac{\gamma - 1}{M_g R}\right) P_g A_p \frac{dx}{dt} \tag{F.10}$$

$$\dot{V}_\rho = 0.32 \frac{X_o}{D_{ch}}\left(\frac{\rho_g}{\rho_\ell}\right)^{1/2} \frac{dV_g}{dt} \tag{F.11.a}$$

for a turbulent jet and

$$\dot{V}_\rho = A_p\sqrt{a\lambda c} \tag{F.11.b}$$

for the Taylor instability entrainment. The characteristic length (X_o) for the turbulent length is assumed to be the height of the blowdown chute. The hydraulic diameter (D_{ch}) is that of the blowdown chute. These non-linear differential equation and the entrainment equations are solved by a numerical integration technique.

The coupling of the model between the blowdown chute and viewing region expansions need two boundary conditions. The velocity at the exit of the blowdown chute was considered as the initial velocity of viewing region expansion with the correction

$$v\Big|_{\substack{\text{viewing}\\\text{region}}} = \frac{dx}{dt} = v\Big|_{\substack{\text{blowdown}\\\text{chute}}} \left(\frac{A_{\text{chute}}}{A_{\text{viewing region}}}\right) \tag{F.12}$$

Likewise, the accelerations were matched at this point by

$$a\Big|_{\text{viewing region}} = \frac{d^2x}{dt^2} = (P_g - P_{p\ell}) \left(\frac{A_p}{M_{\text{slug}}}\right)\Bigg|_{\substack{\text{viewing}\\\text{region}}} \tag{F.13}$$

Since the actual initial pressure at the beginning of the expansion is less than the initial core pressure, an isentropic correction was made for the model input.

$$P_{gi} = 0.74 \; P_i$$

A more detailed explanation of this model is described by Corradini [13].

APPENDIX G

BASIC EXPANSION MODEL

Inertial constraints of the pool geometry are best illustrated by considering two models for the expansion of the pool. One is a simple one-dimensional slug expansion. The other is a radially symmetric growth pushing the pool surface upward by displacement.

First consider the one-dimensional slug expansion. From Newton's equation of motion, the slug growth when the pressure is uniform across the base of the slug, is given by

$$\ddot{s}_2 = \frac{P - P_\infty}{\rho H} \tag{G.1}$$

for an open top condition. This equation is easily integrated to yield $\dot{s}_2$. From the boundary conditions $\dot{s} = 0$ at $t = 0$,

$$\dot{s}_2 = \frac{P - P_\infty}{\rho H} t \tag{G.2}$$

The radial growth is that of a half cylindrical section from the blowdown chute of dimension R_o (half the width). The momentum equation neglecting surface tension, viscous forces, and body forces for steady state growth is

$$\rho v_r \frac{\partial v_r}{\partial r} = - \frac{\partial P}{\partial r} \tag{G.3}$$

From continuity of volume as the cylinder expands,

$$v_r = \frac{RV_R}{r} \tag{G.4}$$

Also, from this relationship,

$$r \frac{\partial v_r}{\partial r} + v_r = 0 \tag{G.5}$$

From equations (G.4) and G.5), substitution into (G.3) yields

$$\rho \, R^2 V_R^2 \, \frac{\partial r}{r^3} = \partial P \tag{G.6}$$

Integrating (G.6) for an infinite bubble growth from a differential pressure $P - P_\infty$, then with proper substitution

$$\dot{r} = \left[\frac{2(P - P_\infty)}{\rho} \right]^{1/2} \tag{G.7}$$

Assuming no entrainment in the bubble, the surface displacement can be related to the bubble volume by

$$V_{total} = V_{slug} + V_{bubble} \tag{G.8}$$

To get the surface velocity with this model $\dot{s}_1$,

$$\dot{s}_1 = \frac{\pi}{L} r \frac{dr}{dt} = \frac{\pi}{L} r \, \dot{r} \tag{G.9}$$

By integrating (G.7) with $r = R_o$ at $t = 0$ and substitution into G.9)

$$\dot{s}_1 = \frac{\pi}{L}\left[\left(\frac{2(P - P_\infty)}{\rho}\right)^{1/2} t + R_o\right]\left[\frac{2(P - P_\infty)}{\rho}\right]^{1/2} \tag{G.10}$$

To observe the effect of these models, consider the ratio $\dot{s}_1/\dot{s}_2$. The following equation results

$$\frac{\dot{s}_1}{\dot{s}_2} = \frac{2\pi H}{L} + \frac{2\pi R_o H}{Lt}\left(\frac{2(P - P_\infty)}{\rho}\right)^{-1/2} \tag{G.11}$$

which is of the form

$$\frac{\dot{s}_1}{\dot{s}_2} = K_1 + K_2/t \tag{G.12}$$

Thus, a simple result is observed. The velocity ratio will start at infinity and decrease to a value of $2\pi H/L$ as time goes to infinity. When applying the previous analysis to the present experiments, the above slug area is closed. Thus, P_∞ must be varied with time. Assuming an isentropic compression,

$$P_\infty(t) = \frac{P_o V_o{}^{\gamma}}{[LW(Z - H - \dot{s}t)]^{\gamma}} \tag{G.13}$$

With this modification to equation (G.11), and using $\dot{s}$ as that of $\dot{s}_1$, Figure G.1 results. Figure G.1 is a graph of $\dot{s}_1/\dot{s}_2$ versus time for a variety of pressures based on the present experimental apparatus. Also, on Figure G.1, is a graph for a constant P_∞ of 1 bar. A pressure, P, of 6 bars is illustrated in this figure. This figure illustrates that the radial expansion can be modeled as a one-dimensional slug expansion in a relatively short length of time. As seen, the ratio of velocities whether P_∞ is kept constant or not, is close for the entire duration of the expansion. However, the actual values of $\dot{s}_1$ and $\dot{s}_2$ vary significantly.

Figure G.2 shows pool surface velocity varying with time for a 6 bar pressure hydrodynamic run and the two models. As seen here, the pool clearly behaves as a slug for this case as the radial expansion model yields large velocities. This was typical of all the calculations made using equation (G.9) and (G.10). It should be noted that these assume no effects from the chute and the pool is at zero velocity when the bubble emerges into the viewing region.

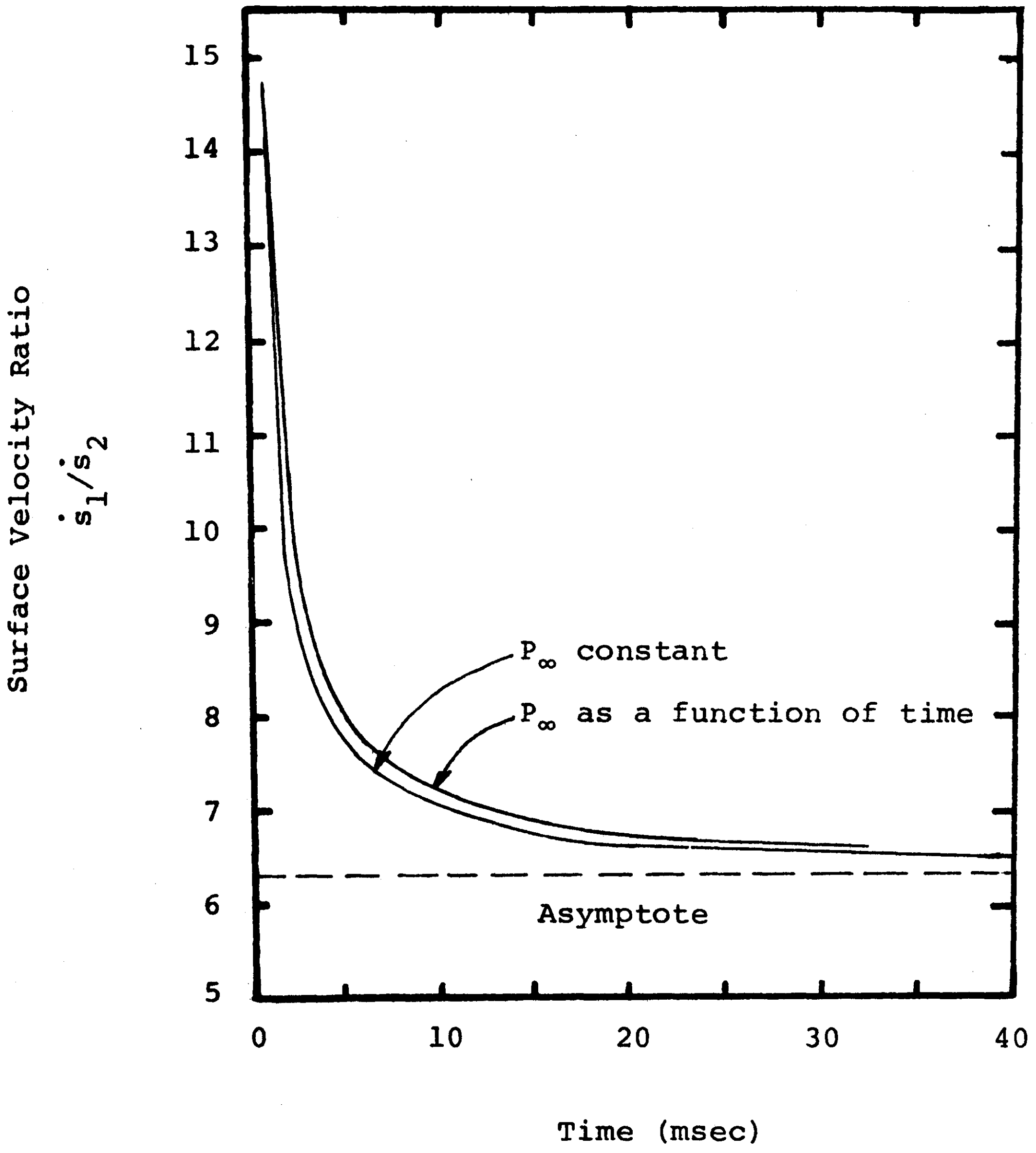

Figure G.1: Ratio of surface velocities for slug and radial bubble expansion models versus time

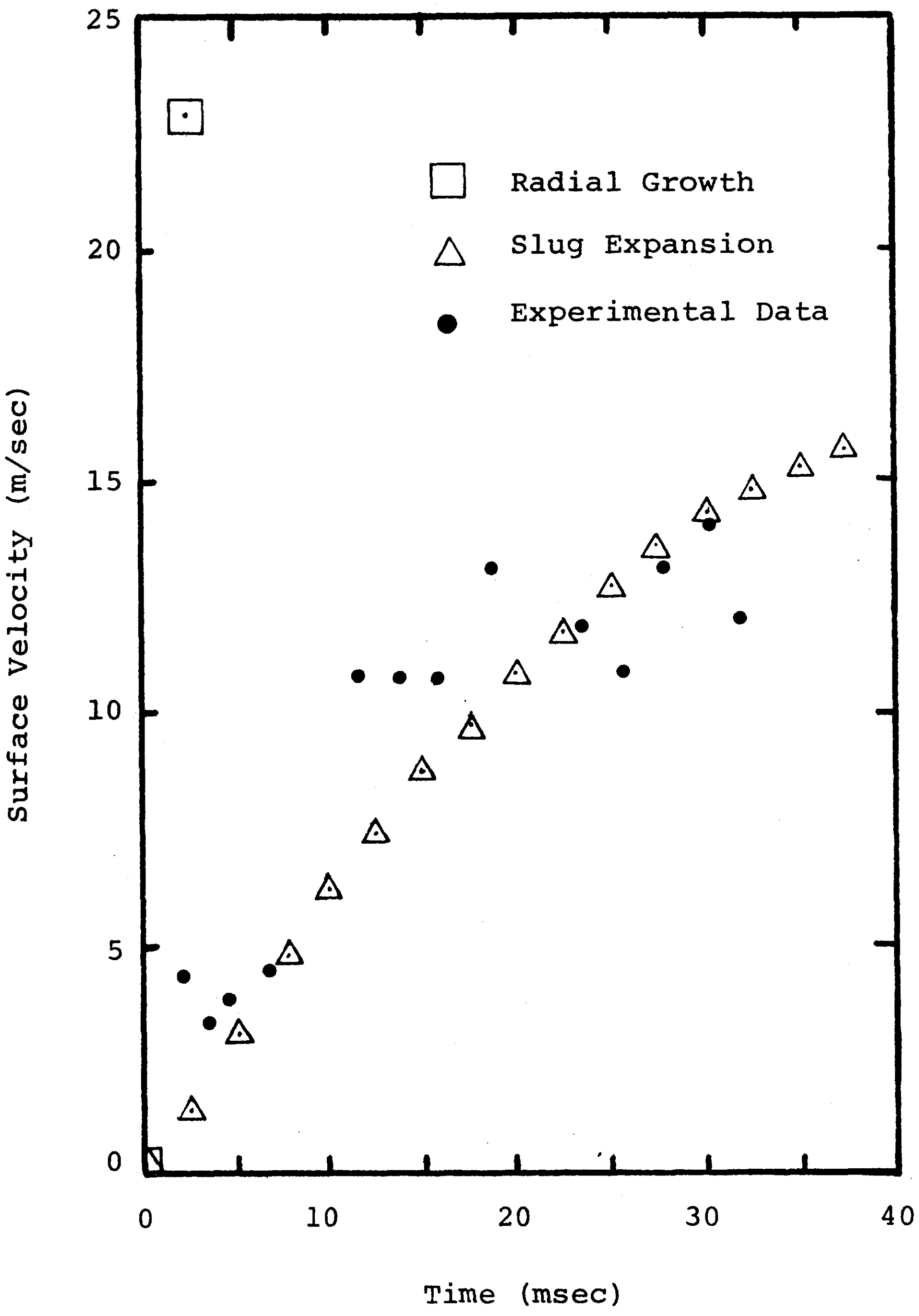

Figure G.2: Radial expansion model, one-dimensional slug model, and experimental data for pool velocity versus time

APPENDIX H

NOMENCLATURE

a	acceleration
A_p	cross sectional area of gas expansion
D_{ch}	hydraulic diameter
H	height of slug
K_1	constant
K_2	constant
L	width of slug
M_g	mass of the gas
M_{slug}	mass of the slug
MW_{gas}	molecular weight of gas
P	pressure
P_g	core gas pressure
P_i	initial core pressure
P_o	initial plenum gas pressure
$P_{p\ell}$	plenum gas pressure
P_∞	plenum pressure
r	bubble radius
$\dot{r}$	bubble radius velocity (v_r)
R	radius
R_g	gas constant of core gas
R_o	universal gas constant
$\dot{s}$	surface velocity
$\dot{s}_1$	surface velocity for radial expansion model
$\dot{s}_2$	surface velocity for slug one-dimensional model
$\ddot{s}_2$	acceleration of surface for slug one-dimensional model
t	time
T_g	temperature of core gas
U	internal energy
v_r	bubble radius velocity
V_r	velocity of radius

Nomenclature (continued)

V_R	velocity of radius
V_o	initial plenum volume
$V_{p\ell}$	volume of plenum gas
V_g	volume of gas
$\dot{V}_\rho$	mass flow rate across interface
V_{total}	total gas volume
w	work
W	thickness of slug
x	displacement
x_o	characteristic length
z	viewing region height

Greek Symbols

γ	ratio of specific heat
λ_c	characteristic wavelength for Taylor instabilities
ρ	density
ρ_1	density of fluid one
ρ_2	density of fluid two
ρ_g	density of gas
ρ_ℓ	density of liquid